Transport in Superconducting/Ferromagnetic Heterostructures

A DISSERTATION
SUBMITTED TO THE FACULTY OF THE GRADUATE SCHOOL
OF THE UNIVERSITY OF MINNESOTA
BY

Evan Marcus Moen

IN PARTIAL FULFILLMENT OF THE REQUIREMENTS
FOR THE DEGREE OF
DOCTOR OF PHILOSOPHY

Oriol T. Valls

July, 2019

Acknowledgements

I would like to thank my adviser, Oriol Valls, for all his help and guidance. His advice was invaluable and he was always there to guide me through all aspects of my PhD as well as planning for my future career. He was persistent and kept me on task, all the while being patient and understanding. I could not thank Oriol enough. I would like to thank my experimental collaborators Ilya Krivorotov and Alejandro Jara. I would also like to thank my committee members, Professors Natalia Perkins, Vlad Pribiag, and Robert Gehrz for their time and input towards my thesis. I would like to like to thank Natalia in particular for providing her advice and guidance in my career search. I would also like to thank Professors Jorge Vinals, Alex Kamenev, Benjamin Baymen, Rafael Fernandes, and J. Woods Halley for their help and support during my tenure here. I would like to thank Chien-Te Wu for all his help with my research. He was always kind and patient with me through all my questions. I would also like to thank Abdul Naseer for his help when I was first getting started, and Chris Conklin for his career advice and help. I would like to thank my friends: Michael Sammon, Michael Mullen, Nicholas Lewellyn, Xuzhe Ying, Zachary Robinson, Nicholas Mast, Daniel Shaffer, Harison Weisman, Santosh Adhikari, Michael Crumrine, Gino Graziano, and Brenda Knauber, and everyone I have had the pleasure to TA with. I would like to thank Scott Dossa for all his help, advice, and interesting conversations. I will not forget our fish bowl at Outpost McNamara. I would like to thank my office mates and friends, Ezra Day-Roberts, Fei Chen, Yang Yang, Tianbai Cui, and Virginia Gali for all their help and support through my last year here. Finally, I would like to thank my family for all their love and support, and for always believing in me. This is for you.

This work was supported in part by DOE grant No. DE-SC0014467. I would like to thank the Minnesota Supercomputing Institute (MSI) for their help and service.

Dedication

I would like to dedicate this thesis to my loving parents, who supported me every step of the way. I wouldn't have done it without you.

Abstract

In this thesis I present my research on spin and charge transport in ferromagnet, superconductor (F/S) heterostructures using a self-consistent, clean limit theory. The goal is to characterize realistic samples. The primary focus is on the $F_1/N/F_2/S$ superconducting spin valve. I also consider the $S_1/F_1/N/F_2/S_2$ ferromagnetic Josephson structures. We solve the Bogoliubov deGennes equations (BdG) using a self-consistent, numerical approach and determine the thermodynamic quantities such as the pair potential. For the charge transport, we use the Blonder-Tinhkam-Kapwijk (BTK) method to determine the conductance G. We study the conductance features and their dependence on the physical parameters such as the layer thicknesses and interfacial quality of the sample. The main results are the dependence of G on the misalignment angle ϕ of the magnetizations in F_2 relative to F_1, which constitutes a 'valve effect'. The valve effect in F/S structures is due to the proximity effect, which is angularly dependent. The critical bias (CB), equal to the gap energy, is non-monotonic with ϕ due to this proximity effect. The conductance features are split for incoming spin-up and spin-down electrons, which leads to a subgap (below CB) peak in the total conductance. This subgap peak is dependent on the intermediate F_2 layer thickness and ferromagnetic exchange field h in which the peak position oscillates between zero bias and the CB with a periodicity of π/h. These subgap peaks are resistant to high interfacial barriers and lead to a monotonic angular dependence on ϕ in the peak maxima. In the $S_1/F_1/N/F_2/S_2$ quasiparticle conductance, there are multiple subgap peaks with similar oscillations in the peak positions. In addition, the conductance peak position oscillates with ϕ by a quarter phase between the parallel and antiparallel configuration. We also study the spin transport in the $F_1/N/F_2/S$ system for realistic parameters. The spin transport quantities are not conserved due to the spin transfer torque (STT) within the ferromagnetic layers, and are spatially dependent. There exists a critical bias feature in which no spin current penetrates the S layer for biases below the CB, and the STT becomes quasilinear for biases above the critical bias.

Contents

List of Figures

Chapter 1

Introduction

In this thesis I present my study on transport in ferromagnetic/superconducting heterostructures. Much of the work presented here is on the $F/N/F/S$ "superconducting spin valve" structure, where F represents a ferromagnetic layer, N a normal metal, and S a superconductor. These devices introduce a superconducting layer to the spin valve structure, which is a device in which two ferromagnetic layers are separated by another material, typically an insulator [1]. Spin valves are based on the Giant Magnetoresistance effect (GMR) [2, 3], where the resistance of the multilayer is significantly increased when the relative orientation of the magnetizations go from a parallel to anti-parallel configuration.

Recently, the development of layered F and S heterostructures with clean interfaces have been made possible, and with it, many spintronic devices featuring superconductors have been proposed [4, 5, 6]. As we will see in the chapters to follow, these devices can have unique properties in both the charge and spin transport. We also study the charge transport in the $S/F/N/F/S$ heterostructure, which is a modification of the Josephson junction [7] with potential use in speicalized electronic devices [8]. Our work is part of a joint theoretical/experimental collaboration with the University of California, Irvine, with the expressed purpose of fabricating and then characterizing these superconductor spintronic devices. Using our clean limit theory, we wish to determine the transport properties and their dependencies on the physical parameters of the system, chiefly the thickness dependence of the layers and the angular dependence of the magnetization orientation within the ferromagnets. We also consider the interfacial scattering quality,

which is essential to describe realistic experimental samples. We hope that the presented work will serve useful in the future development of superconductor spintronic devices. Previous work [9] had successfully characterized the equilibrium properties, such as the critical temperature, in $F/N/F/S$ devices using cobalt, copper, and niobium, with appropriately fitted parameters. For this reason, we will assume the same physical parameters for the same materials in our model.

The organization of this introduction is as follows: In Sec. 1.1 we introduce the basic theory on superconductivity which is fundamental to our theory. In Sec. 1.2 we discuss the proximity effects of N/S and F/S heterostructures. In Sec. 1.3 we do a brief overview of the Josephson junction and theory. In Sec. 1.4 we present our numerical, self-consistent methods in determining the equilibrium properties of the $F/N/F/S$ structure which are necessary in the study of both spin and charge transport. Finally, in Sec. 1.5, we give a brief summary of the chapters that follow.

1.1 Background on BCS superconductivity

Superconductivity was first discovered in 1911 by Heike Kamerlingh Onnes in Hg [10]. When trying to determine the resistivity of various materials at low temperatures, he noticed something very odd was happening in Hg. When he cooled the sample below 4.2 K the resistivity would abruptly drop to zero. This resistance-less current is called a supercurrent and the 4.2 K temperature is known as the critical temperature of Hg. This superconductivity was later found in other materials such as lead and niobium.

Another fundamental aspect of superconductivity is the Meissner effect [11] in which the magnetic flux from an applied field is completely expelled from a superconductor ($M = -\frac{1}{\mu_0}B$) for fields below a critical field value B_c. This critical field also decreases with increasing temperature and goes to zero at $T = T_c$. The difference in free energy between the normal state (N) and the superconducting state (S) is the work done by the field $F_N(B_c) - F_S(0) = B_c^2/2\mu_0$. Since its discovery, there have been many attempts to describe these two aspects of superconductivity, with two prominent examples being the London equations [12] and the Ginzburg-Landau theory of superconductivity [13, 14, 15]. However, it wasn't until much later that the phenomenon was understood in a completely microscopic theory.

The first truly successful microscopic theory came in 1957 by Bardeen, Cooper, and Schrieffer (BCS) [16]. In this theory, pairs of opposite spin and momentum electrons known as Cooper pairs form bound states near the Fermi surface due to a weak, phonon-mediated attraction [17]. The formation of these pairs leads to an energy gap near the Fermi surface. The Cooper pairs have a long range coherence (ξ_0 at $T = 0$), on the order of nanometers, and the thermal fluctuations can not break them apart for temperatures below T_c. This coherent state then condenses to an energy below the Fermi surface, which opens an energy gap in the allowed states of excitations, leading to resistanceless flow. The BCS ground state can be described by the wavefunction $|\psi_G\rangle = \prod_k u_k + v_k c^\dagger_{k\uparrow} c^\dagger_{-k\downarrow}|\psi_0\rangle$ where $|\psi_0\rangle$ is the vacuum state and $|v_k|^2(|u_k|^2)$ is the probability that the $(\mathbf{k}\uparrow, -\mathbf{k}\downarrow)$ state is occupied(unoccupied). In the original BCS paper, a variational method was used to determine the ground state energy and critical temperature relationship with the gap energy. However, we will use the Bogoliubov approach [18] to determine these quantities [14, 15] as it is better suited to deal with excitations and spatially non-uniform Hamiltonians, which are essential in the study of transport in heterostructures. Here and throughout, we assume a typical, BCS s-wave superconductor such as niobium.

We start with the Hartree-Fock Hamiltonian with a singlet-pair interaction V_{kl}:

$$\mathcal{H} = \sum_{k,\sigma} \epsilon_k c^\dagger_{k\sigma} c_{k\sigma} + \sum_{k,l} V_{kl} c^\dagger_{k\uparrow} c^\dagger_{-k\downarrow} c_{-l\downarrow} c_{l\uparrow} \tag{1.1}$$

where ϵ_k is the single particle energy. If we assume $\langle c_{-k\downarrow} c_{k\uparrow}\rangle \neq 0$ and that the fluctuations about this expectation value are small, we can express the BCS Hamiltonian as:

$$\mathcal{H}_{BCS} = \sum_{k,\sigma} \epsilon_k c^\dagger_{k\sigma} c_{k\sigma} + \sum_k \left(\Delta_k c^\dagger_{k\uparrow} c^\dagger_{-k\downarrow} + \Delta^*_k c_{-k\downarrow} c_{k\uparrow}\right) \tag{1.2}$$

where we define the self-consistent pair potential as

$$\Delta_k = -\sum_l V_{kl} \langle c_{-k\downarrow} c_{k\uparrow}\rangle \tag{1.3}$$

and $\langle c_{-k\downarrow} c_{k\uparrow}\rangle$ is the pair amplitude. In addition, we have dropped a constant from the BCS Hamiltonian. We then diagonalize the Hamiltonian to the form $\mathcal{H}_{BCS} =$

$\sum_{k,\sigma} E_k \gamma^\dagger_{k\sigma}\gamma_{k\sigma}$ using the Bogoliubov transformation:

$$\gamma_{k\uparrow} = u_k c_{k\uparrow} - v_k c^\dagger_{k\downarrow} \tag{1.4a}$$

$$\gamma_{k\downarrow} = u_k c_{k\downarrow} + v_k c^\dagger_{k\uparrow} \tag{1.4b}$$

where by the anti-commutation relation of the fermion operators we see that $|u_k|^2 + |v_k|^2 = 1$. Furthermore, the choice of u_k and v_k which diagonalizes the Hamiltonian must follow the relation $2\epsilon_k u_k v_k + \Delta^*_k {v_k}^2 - \Delta_k {u_k}^2 = 0$. Solving this we get the relation that

$$|u_k/v_k| = (E_k - \epsilon_k)/|\Delta_k| \tag{1.5}$$

where $E_k = \sqrt{({\epsilon_k}^2 + |\Delta_k|^2)}$ is the excitation energy of the Bogoliubov quasiparticles and $|\Delta_k|$ is the energy gap. The probability that the Bloch state $(\mathbf{k}\uparrow, \mathbf{k}\downarrow)$ is occupied is given by

$$|v_k|^2 = 1 - |u_k|^2 = \frac{1}{2}\left(1 - \frac{\epsilon_k}{E_k}\right) \tag{1.6}$$

In the BCS approximation, it is assumed that the potential is attractive and independent on the wavevectors ($V_{kl} = -V$). For phonon-mediated attractions, this potential is nonzero only for energies below the Debye frequency $\hbar\omega_D$. We can then use the Bogoliubov transformation to self-consistently solve for the pair potential [18, 19] by substituting the transformation into Eq. 1.3,

$$\Delta_k = -\sum_l V_{kl}\langle c_{-k\downarrow} c_{k\uparrow}\rangle = V u^*_k v_k \left(1 - 2f(E_k)\right) = V u^*_k v_k \tanh\frac{\beta E_k}{2} \tag{1.7}$$

where $f(E_k)$ is the Fermi function. Substituting $2u^*_k v_k = \frac{\Delta_k}{E_k}$ we can solve for Δ and we get the condition:

$$\frac{1}{V} = \frac{1}{2}\sum_k \frac{\tanh(\beta E_k/2)}{E_k} \tag{1.8}$$

where $\beta = (k_B T)^{-1}$. We sum (or integrate) for all energies below the Debye cutoff frequency $\hbar\omega_D$. We can independently solve for $\Delta(T = 0)$ or T_c in terms of V by substituting $T = 0$ or $E_k = \epsilon_k$ into Eq. (1.8) respectively. By eliminating V, we can relate the pair potential at zero temperature to the critical temperature as $\Delta(0) \approx 1.763\ k_B T_c$. The predictions of the BCS theory has since been confirmed for many conventional

superconductors and still stands as the pillar of the theory of superconductivity.

1.2 Proximity Effects and Andreev Reflection

When a superconductor is in contact with a normal metal (N), and if the contact is good, the Cooper pairs may leak into the normal metal near the N/S interface [20]. The Cooper pairs remain coherent for long distances in the normal metal. For temperatures well above the transition temperature of the normal metal, these coherent Cooper pairs do not lead to the formation of an energy gap Δ within N. The Cooper pair amplitude is given by

$$F(\mathbf{r}) = \langle \psi_\uparrow(\mathbf{r})\, \psi_\downarrow(\mathbf{r}) \rangle \tag{1.9}$$

For an N/S interface normal to the x axis, the pair potential can then be described by $\Delta(x) = g(x)F(x)$ where $g(x)$ is only nonzero in the superconductor. Near the N/S interface, the pair amplitude is a slowly varying function with an asymptotic decay into the N layer:

$$F = f(x)e^{-|x|/\xi_N} \tag{1.10}$$

where ξ_N is the proximity length of the pair amplitude in the normal metal and $f(x)$ is some slowly varying function of position. If the normal metal is "clean", i.e. the electron mean free path ℓ is much greater than the proximity length ξ_N, then we can determine the proximity length to be $\xi_N = \frac{\hbar v_F}{2\pi k_B T}$. This proximity length is quite long, and in the $T = 0$ limit the pair amplitude goes as $1/x$. For example, the proximity length in N is on the order of 1000 Å for superconducting Sn at $T = 1.5$ K with gold contacts [21]. In the opposite "dirty" limit ($\ell \ll \xi_N$) the proximity length is dependent on the mean free path such that $\xi_N = \sqrt{\frac{\hbar v_F \ell}{6\pi k_B T}}$ [20].

The proximity effect in F/S heterostructures is of particular physical interest due to the antagonistic nature of the two materials [22]. As described above, an s-wave superconductor forms opposite spin Cooper pairs. Ferromagnets, on the other hand, prefer same-spin electron states. In the effective field approximation, the internal exchange interaction of the ferromagnet is represented by an effective magnetic field field H_{eff}. We then define the exchange field $h = \mu_B H_{eff}$, also known as the Stoner field, which is along the direction of the internal magnetization [22, 23]. If we consider the

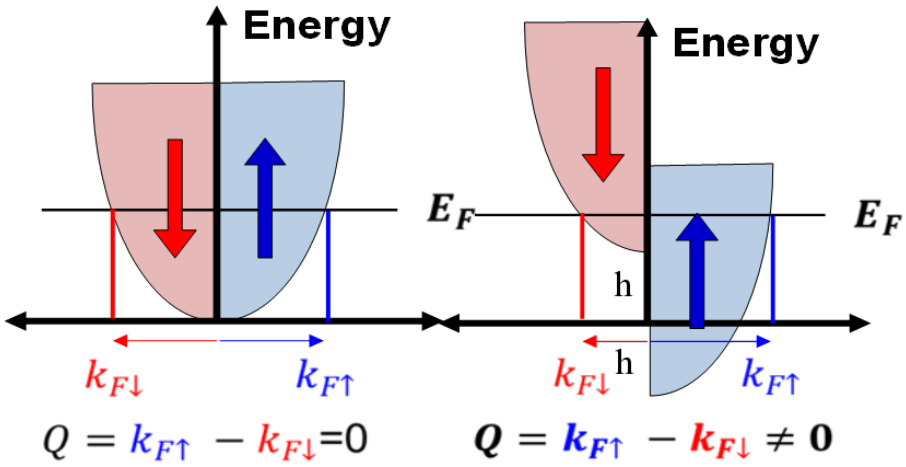

Figure 1.1: Sketch of the band-splitting due to the Stoner exchange field h [24]. Left is a representation of a normal metal with symmetric spin bands, and the right a ferromagnet characterized by an exchange field h. The center of mass momentum Q is nonzero within the ferromagnetic due to this splitting.

exchange field to be in the z direction, then the spin-up band decreases in energy by h relative to the Fermi energy and the spin-down band increases in energy by h (see Fig. 1.1 above and Eq. 1.11 below). The exchange field creates an imbalance in the number of states between spin-up and spin-down, and thus same-spin pair correlations (such as the $S = 1$, $m_z = \pm 1$ triplet correlations) are favored within a ferromagnet.

In addition, the singlet pair correlation amplitudes pick up a center of mass momentum $Q = 2h/v_F$ within the ferromagnet [25], as the momentum of the spin up ($\hbar k_{F\uparrow}$) and spin down ($\hbar k_{F\downarrow}$) band is shifted in opposite directions with respect to the Fermi energy (see Eq. 1.11 below). In all, this leads to a damped, oscillatory pair amplitude in the F/S proximity effect [26, 27]. The proximity length of the singlet pair amplitude can be expressed as [28] $\xi_F \approx (k_{F\uparrow} - k_{F\downarrow})^{-1}$ where $k_{F\sigma}$ is the Fermi wavevector of the spin σ band. We may express the F layer energy spectrum as:

$$\frac{\hbar^2 k_{F\uparrow}^2}{2m} = E_F\,(1+h)\,, \tag{1.11a}$$

$$\frac{\hbar^2 k_{F\downarrow}^2}{2m} = E_F\,(1-h)\,, \tag{1.11b}$$

where we have now normalized the effective exchange field energy h to the Fermi energy E_F. Thus the proximity length in the F layer is [25]

$$\xi_F \approx (k_{F\uparrow} - k_{F\downarrow})^{-1} = k_F^{-1}\left(\sqrt{1+h} - \sqrt{1-h}\right)^{-1} \approx \frac{1}{h}k_F^{-1} \tag{1.12}$$

A similar analysis of Eq. (1.11) shows that the change in momentum $\hbar(k_{F\uparrow} - k_{F\downarrow}) = 2h/v_F$

For a typical ferromagnet, in which the normalized exchange field is on the order of 0.1, this leads to a proximity length on the order of 10 Å. This is much smaller than in the normal metal proximity effect. This has the effect that a significantly reduced portion of the singlet pair amplitude leaks into the ferromagnet as it does the normal metal. The leakage of the pair amplitude $F(x)$ has the effect of reducing the pair potential $\Delta(x)$ near the interface. If the superconducting layer is not too thick (but still larger than the coherence length), the Cooper pair amplitude (and thus the pair potential) is depleted throughout the superconducting layer by the proximity of the normal metal. This effect is minimal for the short ranged F/S proximity effect. In addition, the oscillatory nature of the pair amplitude in the ferromagnet may affect the spatial dependence of F/S heterostructures.

One key aspect of the F/S proximity effect is that long ranged triplet correlations may be induced [29, 30, 31, 32] even for an s-wave superconductor. In the N/S heterostructure, the Hamiltonian commutes with both the $\mathbf{S}$ and S_z operators, and thus no triplet correlations can be induced ($S = 0$ singlet states only). In the case of a single, homogeneous ferromagnet, the rotational symmetry of the spin states is broken, and the $\mathbf{S}$ operator no longer commutes (but S_z does), thus the $S = 1$, $m_z = 0$ triplet state can be induced. The $m_z = \pm 1$ triplet states may be induced through a non-uniform ferromagnet or a second ferromagnet with a non-collinear magnetization, for which the S_z operator no longer commutes with the Hamiltonian (see Eq. 1.19 as an example). This symmetry may also be broken for materials with significant spin-orbit coupling. Due to the Pauli Principle, these triplet correlations must be odd in frequency [33] or in time [31] if the superconductor is s-wave symmetric. The proximity effect for the $m_z = 0$ triplet is short-ranged for the same reason that the singlet state is: the ferromagnet favors same-spin pair correlations. On the other hand, the $m_z = \pm 1$ triplet

correlations are long-ranged in the F layer [23, 34, 35, 36, 37, 38, 39]. For an $F/F/S$ heterostructure, the second ferromagnet effectively "rotates" the $m_z = 0$ short-ranged triplet states partially into the long-ranged $m_z = \pm 1$ states for non-collinear F layer magnetizations. For collinear orientations, only short ranged proximity effects occur.

It was suggested by Žutić et. al. (Ref. [5]) that superconductor heterostructures could be applied to spintronic devices, which are electronic devices that utilize the electron's spin as opposed to its charge. Since then, many ferromagnetic and superconducting heterostructures have been proposed [4, 40, 41, 42, 43, 44] which utilize multiple ferromagnets with non-uniform magnetization, typically in an $F/S/F$ or $F/F/S$ structure, or a single ferromagnetic with non-uniform magnetiziation such as holmium [45, 46, 47]. In these devices, the induced triplet correlations play an important role in the spintronic state of the system. The long-range correlations of the non-collinear magnetization allows for more leakage of the singlet pair amplitude into the ferromagnetic layers, which reduces the pair potential within the superconductor. The reduction of the pair potential, and the consequences of it (such as a drop in T_c), constitutes a "valve-effect" in the transport properties due to the angular dependence of the triplet correlations. Unlike the GMR valve effect in a typical spin valve, the valve effect on the triplet correlations is non-monotonic since the long range ($m_z = \pm 1$) correlations are induced for only non-collinear orientations.

The oscillatory nature of the F/S proximity effects gives rise to many unique thermal equilibrium properties [48]. It has been experimentally verified that the critical temperature T_c is oscillatory with thickness [9] and with the angular mismatch of the magnetizations [32, 9]. These proximity effects give rise to unique transport properties too [41]. The thermal equilibrium properties may themselves have an impact on the transport by reducing the pair potential energy gap or by decreasing the critical temperature, via the induced triplet correlations.

So far we have discussed the proximity effect in terms of the equilibrium properties, but the proximity effect is directly related to transport as well. Consider an electron with bias eV in a normal metal N that is impinging on the N/S interface. Normally, for biases less than the gap energy, one would expect that the superconductor perfectly reflects the electron as there are no states available to accept a single, unpaired electron within the gap. This is indeed the case for a tunnel junction, where there is no current for

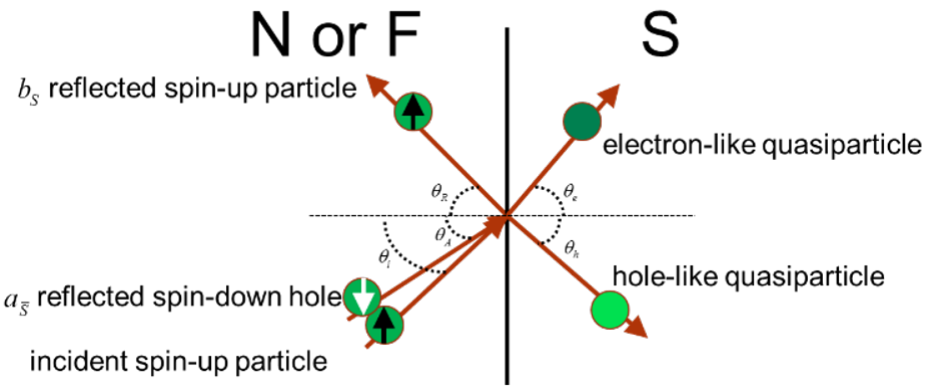

Figure 1.2: Sketch of the Andreev reflections [24]. A spin-up electron may reflect at the interface as a spin-up electron with probability b (normal reflection) or a spin-down hole with probability a (Andreev reflection). The transmission amplitudes within the superconductor are electron-like and hole-like excitations above the energy gap.

biases below the gap potential. However, for a clean interface, an electron of momentum $\mathbf{k}$ and spin σ may pair with another electron to form a Cooper pair near the Fermi energy within the superconducting gap. This process is known as Andreev reflection [49] (see Fig. 1.2 above). By conservation of charge and momentum, the transmitted electron must reflect as a hole with opposite momentum $-\mathbf{k}$. In addition, since the singlet Cooper pairs have net zero spin, the hole must also have opposite spin $-\sigma$. Since this process takes a right-moving electron and reflects a left-moving hole of opposite charge, the net current is doubled. This means that the conductance for biases below the gap energy (i.e. the subgap conductance) is twice the conductance that is above the gap energy (i.e. the normal conductance) [50, 51].

If we now consider triplet correlations, which are prevalent in the inhomogeneous F/S proximity effect, an electron may form a triplet same-spin Cooper pair through the reflection of a same-spin hole [41, 52, 53, 54, 55]. This is known as anomalous Andreev reflection. Andreev reflections and the resulting transport properties are dependent on the exchange field within the F layer(s) [56, 57]. For example, if there is a single homogeneous F layer that is a half-metal ($h = 1$) then there is only one spin band available within the ferromagnet and there can be no opposite spin pair correlations, and thus there is no Andreev reflection and no proximity effect. If triplet states are induced by a second ferromagnet, then the proximity effect can occur through the

anomalous Andreev reflections. The inclusion of the full spectrum of these reflections is imperative in our study on transport in $F/N/F/S$ heterostructures.

1.3 Josephson Junctions

It was once thought unlikely for a supercurrent to travel between two superconductors that are separated by an insulating layer. After all, the probability of a single electron to tunnel through the barrier is quite low, so it would stand to reason that the tunneling probability of a Cooper pair would be neigh impossible since it involves the tunneling of two electrons at the same time. It turns out, this assumption was quite wrong. Brian Josephson described the tunneling of superconducting electrons between two separate superconducting layers in 1962 [7]. He found that a supercurrent may persist with zero voltage induced across the gap. He described the effect through the use of the Bogoliubov theory [15] which included pair creation operators and a tunneling Hamiltonian. For our purposes we will use a simpler argument, as many other works have [10, 14, 58], in order to better understand the basics of the Josephson phenomenon. If we take $\psi = |\psi|e^{i\theta}$, where $|\psi|^2$ is proportional to the number density of the Cooper pairs and θ is the phase of the superconducting order parameter, we can express the current density as:

$$\mathbf{J} = \frac{2e\hbar}{m}|\psi|^2\left(\nabla\theta - \frac{2\pi}{\Phi_0}\mathbf{A}\right) \tag{1.13}$$

$$\theta = \theta_2 - \theta_1 - \frac{2\pi}{\Phi_0}\int \mathbf{A}\cdot d\mathbf{l} \tag{1.14}$$

where $\Phi_0 = \frac{h}{2e}$ is the magnetic flux quantum. For any closed loop, θ must be a multiple of 2π. By integrating Eq. 1.14 we see that the magnetic flux must be an integer multiple of the magnetic flux quantum $\Phi = n\Phi_0$. If we consider tunneling between two superconductors, the tunneling Hamiltonian with an applied bias V in the absence of an external field can be expressed simply as [10]:

$$\begin{pmatrix} -eV & T \\ T & eV \end{pmatrix}\begin{pmatrix}\psi_1 \\ \psi_2\end{pmatrix} = \hbar\frac{\partial}{\partial t}\begin{pmatrix}\psi_1 \\ \psi_2\end{pmatrix}, \tag{1.15}$$

For two identical superconductors ($|\psi_1| = |\psi_2|$) we have the relation that $\frac{\partial|\psi|^2}{\partial t} = \frac{2}{\hbar}T|\psi|^2\sin(\theta)$ where $\theta = \theta_2 - \theta_1$ and $\partial\theta/\partial t = 2eV/\hbar$. Since the charge density is $2e|\psi|^2$, by charge conservation we can determine the current phase relationship [58]:

$$I = I_c \sin(\theta) \tag{1.16a}$$

$$\frac{\partial\theta}{\partial t} = \frac{2\pi}{\Phi_0}V \tag{1.16b}$$

where I_c is the critical Josephson current. This critical current is the maximum DC current that can pass through the Josephson junction at zero bias voltage. For an applied DC current above the critical value, the induced voltage will no longer be zero and will jump to a higher value. This is known as the DC Josephson effect. For a finite applied voltage, the second equation gives the phase relationship of the junction where $\theta(t) = \theta(0) - \frac{2\pi}{\Phi_0}Vt$. In conjunction with Eq. (1.16a), this leads to an AC current for an applied DC bias. This is known as the AC Josephson effect.

In the presence of an external magnetic field, the critical current is modulated by the magnetic flux quantum. By integrated the current Eq. 1.13 over the junction, we may write the maximum DC current as:

$$I_{max} = I_c\frac{\sin(\pi\Phi/\Phi_0)}{\pi\Phi/\Phi_0} \tag{1.17}$$

This current is extremely sensitive to changes in magnetic field. Because of this, devices containing multiple Josephson junctions have proved useful. For example, precise magnetometers can be made using SQUIDs (superconducting quantum interferometer devices) which have set the voltage standard. Another example of a Josephson junction device are the Rapid Single Flux Quantum (RSFQ) devices used in digital signal processing applications for their high clock rate [8].

The Josephson current is not the only current that runs through a Josephson junction, as there is also the contribution of normal electron transport. In the two-fluid model, where the Cooper pair electrons are considered to have completely separate transport from the normal electron transport, we can express the net current in a Josephson structure using the Resistively and Capacitively Shunted Josephson (RCSJ)

model [59].

$$I = I_c \sin(\theta) + GV + C\frac{dV}{dt} \tag{1.18}$$

This equation describes a resistive and capacitive circuit element running in parallel with a pure Josephson junction of tunneling Cooper pairs. This is a non-linear equation and will result in a hysteresis [58] in the current vs voltage (I-V) curves if the time scale of the RC element $\tau_{RC} = RC$ is greater than that of the Josephson junction $\tau_J = \frac{\Phi_o}{2\pi}\frac{1}{I_c R}$ where $R = G^{-1}$. This hysteresis results in a finite current at zero bias when increasing the applied current and (nearly) zero finite current at zero bias for decreasing applied current. In this case, the current characteristic for decreasing current is effectively $I = GV$. This is typically the case for Josephson junctions separated by an insulator (tunnel junction) where the subgap resistance is extremely high and and the capacitance is high as well.

In our study, we will focus on the GV term in Eq. (1.18), known as the quasiparticle current, for clean $S/F/N/F/S$ ferromagnetic Josephson structures. For metallic junctions, or even junctions with a metallic weak-link such as a point contact or microbridge, the normal electrons move more freely through the metal and the capacitance goes to zero, removing the hysteresis in the DC I-V curves. Because of this, there is a finite voltage at which the I-V curve for decreasing currents jumps to zero voltage and to a "capture" current I_{min} which is the minimum DC current that can be attained at a non-zero bias [58]. This capture current is less than or equal to the critical current I_c of the DC Josephson effect. This can make it difficult to measure the quasiparticle current (GV) for low biases as the system will tend to jump to zero bias as the current is decreased. This can be avoided in two ways: one is to modulate the current loop with a magnetic field such that critical current I_c is at a minimum [60] (see Eq. 1.17). Another approach is to simply shunt the Josephson junction with a capacitor and resistor in parallel to the junction [61]. This will restore the hysteresis which then minimizes I_{min} and thus drives the minimum voltage close to zero. Therefore it is possible to probe the quasiparticle bias dependence into the subgap regime, where $eV < \Delta$.

In this body of work, we intend to study the subgap conductance for metallic, ferromagnetic/superconducting heterostructures, including Josephson structures. In Chapter 5 we review the theory on the quasiparticle, subgap bias dependence on the conductance in metallic weak-link Josephson structures. We then perform an analytic and numerical study on $S/F_1/N/F_2/S$ ferromagnetic Josephson structures using a suitable ballistic theory.

1.4 Bogoliubov deGennes equations

In this section we discuss the methods we use to determine the equilibrium (thermodynamic) quantities of the ferromagnetic/superconducting heterostructure that accounts for the proximity effects discussed in Sec. 1.2. In all our calculations, both equilibrium and transport, it is imperative to determine the BCS energy gap, i.e. the pair potential, in a self-consistent manner. The self-consitent condition is neccessary to the determination of the equilibrium quantities such as the critical temperature [48]. In addition, it has been shown [41, 62, 63, 64] that it is imperative in transport calculations as a non-self-consistent solution violates charge conservation. We will review charge conservation in greater detail in Sec. 2.2.3. Here, we summarize our methods to determine the thermodynamic properties of the heterostructures and leave discussing the calculation of the transport quantities, such as the conductance and spin current, to later chapters.

In Sec. 1.1 we determined the self-consistent condition for a bulk, s-wave superconductor described by the BCS Hamiltonian Eq. (1.2). Bogoliubov deGennes generalized Eq. (1.2) to allow for the inclusion of a non-uniform, external potential [15, 18]. This was later modified by Buzdin [22] to include magnetism through the use of an effective field $\mathbf{h}$. With the effective field approximation, each spin band within the ferromagnet has its Fermi energy shifted by the exchange field: $E_{F,\sigma} = E_F + \eta_\sigma h$ where $\eta_\sigma \equiv 1(-1)$ for the spin up(down) band.

For most of this thesis (Chapters 2, 3, and 4), we will be discussing both spin and charge transport in $F_1/N/F_2/S$ superconducting spin valve heterostructures. A sketch of the geometry is given by Fig. 1.3. In Chapter 5 we will also analyze a similar $S_1/F_1/N/F_2/S_2$ Josephson structure (see Fig. 5.1). The F layers represent ferromagnets of the same material and the S layer is a superconducting material, whose parameters

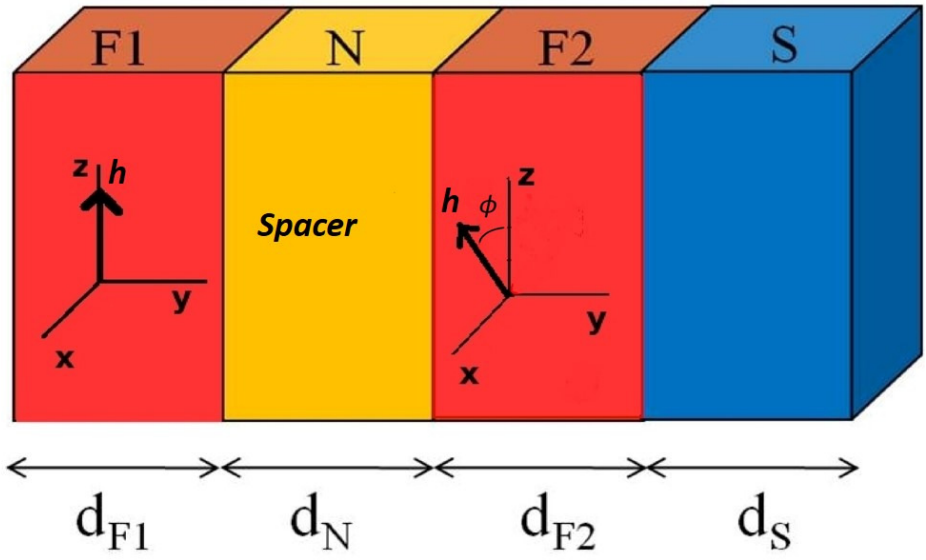

Figure 1.3: Sketch of the $F_1/N/F_2/S$ heterostructure with the notation for thicknesses of the different layers indicated. The magnetizations of the outer magnetic layer F_1 is along the z axis while that in F_2 it is in the x-z plane, forming an angle ϕ with the z axis, as indicated. The y axis is normal to the layers. This sketch is not to scale.

will be set to the values found in Ref. [9], appropriate for cobalt and niobium. The layer thicknesses are chosen in close consultation with our experimental collaborators. In each case there are two ferromagnets separated by a normal metal spacer. This spacer is typical in experimental samples as a means to control the magnetization orientation of one layer without affecting the other. With this, we can define the magnetization misalignment angle ϕ. In the F_1 layer the magnetization is set at the z-axis and in the F_2 layer it is rotated by ϕ in the x-z plane.

To generalize the BCS Hamiltonian (Eq. 1.2), we define the operators $\psi_\sigma(\mathbf{r}) = \sum_k e^{i\mathbf{k}\cdot\mathbf{r}} c_{k\sigma}$ and so on for $\psi^\dagger_\sigma(\mathbf{r})$. We can then express the Hamiltonian, which includes the exchange interaction of the ferromagnet layers, by:

$$\begin{aligned}\mathcal{H}_{eff} &= \int d^3r \left\{ \sum_\alpha \psi^\dagger_\alpha(\mathbf{r})\, \mathcal{H}_0 \psi_\alpha(\mathbf{r}) + \frac{1}{2}\left[\sum_{\alpha,\,\beta} (i\hat{\sigma}_y)_{\alpha\beta}\, \Delta(\mathbf{r})\, \psi^\dagger_\alpha(\mathbf{r})\, \psi^\dagger_\beta(\mathbf{r}) + H.c. \right] \right. \\ &- \left. \sum_{\alpha,\,\beta} \psi^\dagger_\alpha(\mathbf{r})\, (\mathbf{h}\cdot\hat{\boldsymbol{\sigma}})_{\alpha\beta}\, \psi_\beta(\mathbf{r}) \right\}, \end{aligned} \tag{1.19}$$

where $\mathcal{H}_0 = -\nabla^2/2m - E_F + U(\mathbf{r})$ is the single particle Hamiltonian, $\mathbf{h}$ is the Stoner exchange field, and $\Delta(\mathbf{r})$ is the pair potential. In the single particle Hamiltonian, E_F is the Fermi energy and $U(\mathbf{r})$ is the scattering potential. The $\hat{\sigma}$ vector components correspond to the σ_x, σ_y, and σ_z Pauli matrices respectively. We then do a Bogoliubov transformation (a direct analog of Eq. 1.4):

$$\psi_\uparrow(\mathbf{r}) = \sum_n \left(\gamma_{n\uparrow} u_n(\mathbf{r}) - \gamma^\dagger_{n\downarrow} v^*_n(\mathbf{r})\right) \tag{1.20a}$$

$$\psi_\downarrow(\mathbf{r}) = \sum_n \left(\gamma_{n\downarrow} u_n(\mathbf{r}) + \gamma^\dagger_{n\uparrow} v^*_n(\mathbf{r})\right) \tag{1.20b}$$

the result of which are a series of coupled equations known as the Bogoliubov equations (see Ref. [15]). These equations can be solved numerically for the self-consistent condition. Below, we express the Bogoliubov equations and the self consistency equation in the quasi-one dimensional case in Eqs. 1.22 and 1.23 respectively.

The layers are assumed to be infinite in the transverse x-z plane and finite in the longitudinal y direction, making our theoretical description quasi-one dimensional. Since the Stoner field is perpendicular to the direction of the spatial dependence, it is convenient to choose the y-axis as the longitudinal direction to eliminate the complex σ_y Pauli matrices in our numerical calculations. The three-dimensional problem can be made one-dimensional by $\psi_\sigma(\mathbf{r}) = \sum_k e^{i\mathbf{k}_\perp\cdot\mathbf{r}} e^{ik_y y} c_{k\sigma}$, and the the Bogoliubov wavefunction becomes $u_n(\mathbf{r}) = e^{i\mathbf{k}_\perp\cdot\mathbf{r}} u_n(y)$ and so on for v_n.

The Bogoliubov transformation is now

$$\psi_\sigma(y) = \sum_n \left(u_{n\sigma}(y)\gamma_n - \eta_\sigma v^*_{n\sigma}(y)\gamma^\dagger_n\right), \tag{1.21}$$

where $\eta_\sigma \equiv 1(-1)$ for spin-up (down). We then express the eigenvalue equations as:

$$\begin{pmatrix} H_0 - h_z & -h_x & 0 & \Delta \\ -h_x & H_0 + h_z & \Delta & 0 \\ 0 & \Delta & -(H_0 - h_z) & -h_x \\ \Delta & 0 & -h_x & -(H_0 + h_z) \end{pmatrix} \begin{pmatrix} u_{n\uparrow} \\ u_{n\downarrow} \\ v_{n\uparrow} \\ v_{n\downarrow} \end{pmatrix} = \epsilon_n \begin{pmatrix} u_{n\uparrow} \\ u_{n\downarrow} \\ v_{n\uparrow} \\ v_{n\downarrow} \end{pmatrix}, \tag{1.22}$$

where each term is implicitly a function of y and we have dropped it from our notation

in Eq. (1.22) for readability. $u_{n\sigma}(y)$ and $v_{n\sigma}(y)$ are the quasiparticle and quasihole amplitudes in the Bogoliubov transformation. These amplitudes are spatially dependent on y and the spin dependence is due to the inclusion of the exchange field. We express this Hamiltonian in the natural units $\hbar = k_B = 1$. The single particle Hamiltonian is $H_0 = -(1/2m)(d^2/dy^2) + \epsilon_\perp - E_F(y) + U(y)$ where $E_F(y)$ is the layer dependent width of the band: $E_F(y) = E_{FS} \equiv k_{FS}^2/2m$ in the S layer and $E_F(y) = E_{FM}$ in the F layers. We may define a mismatch parameter [65] Λ as $E_{FM} \equiv \Lambda E_{FS}$ although we typically set $\Lambda = 1$ for reasons we explain later on. $U(y)$ is the scattering potential due to imperfect interfaces. For the $F/N/F/S$ system, this potential can be expressed as a series of delta function potentials at the interfaces: $U(y) = H_1\delta(y - d_{F1}) + H_2\delta(y - d_{F1} - d_N) + H_3\delta(y - d_{F1} - d_N - d_{F2})$ where d_i is the thickness of the ith layer and $y = 0$ is at the leftmost end of the heterostructure. In general, this can be extended to any heterostructure with interfacial barriers H_i. The term $\epsilon_\perp$ is the transverse kinetic energy which makes Eq. 1.22 a set of decoupled equations, one for each $\epsilon_\perp = k_\perp^2/2m$. The Stoner exchange field $\mathbf{h}(y)$ is a nonzero constant within each F layer. For two identical ferromagnets, we define the magnitude of the exchange field to be $h = h_1 = h_2$. In the F_1 layer, we set our z-axis to be along the direction of the exchange field such that $\mathbf{h}_1 = h\hat{\mathbf{z}}$ while in the F_2 layer, $\mathbf{h}_2$ is rotated by a misalignment angle ϕ in the x-z plane.

The pair potential term $\Delta(y)$ is nonzero only within the superconducting layer (as opposed to the pair amplitude, see Eq. 1.9). This spatial dependence is due to the proximity effect discussed in Sec. 1.2. Therefore, all calculations which prominently involve proximity effects must be solved self-consistently. The self-consistency condition is:

$$\Delta(y) = \frac{g(y)}{2}{\sum_n}' \left[u_{n\uparrow}(y)v_{n\downarrow}^*(y) + u_{n\downarrow}(y)v_{n\uparrow}^*(y)\right] \tanh\left(\frac{\epsilon_n}{2T}\right), \tag{1.23}$$

with the summation being over all eigenstates (and all $\epsilon_\perp$) and the prime indicates that it is limited to states with eigenenergies within a cutoff ω_D from the Fermi level. The quantity g is the superconducting coupling constant for the singlet pair correlation and is nonvanishing in S only. The self-consistent solution requires a numerical approach. The details of such a calculation can be found in Ref. [66].

To get a self-consistent result, we use an iterative method: we start with a suitable initial choice of $\Delta(y)$ and solve for the quasiparticle amplitudes $u_n(y)$ and $v_n(y)$ via

Eq. 1.22. Using these amplitudes we calculate the pair potential with Eq. 1.23. We then iterate Eqs. 1.22 and 1.23 until the input and output values of $\Delta(y)$ coincide. One can then derive the thermodynamic quantities from the self-consistent wavefunctions[40, 31], the results of which have been found to be in agreement with experimental work [9].

1.5 Summary

In Chapter 2, the BdG equations from section 1.4 are applied to the $F_1/N/F_2/S$ superconducting spin valve. The BTK method is used to calculate the conductance as explained therein. We study the dependence of the conductance on the physical parameters such as layer thicknesses, interfacial scattering, and temperature. We find a non-monotonic dependence on the magnetic misalignment angle ϕ. We also find resonance effects with a dependence on the interlayer thicknesses. We briefly discuss the calculation of the spin current for an idealized system. The work presented in this chapter is based on a previous publication Ref. [67] which has been edited for use in this thesis.

In Chapter 3, we extend the analysis done in Chapter 2 and study the intermediate layer thickness dependence in greater detail. We find that in the $N/F/S$ heterostructure, which necessarily includes scattering at the N/F interface, there is a subgap peak in conductance. This peak is due to the large difference in the conductance contributions from spin-up and spin-down electrons which we call collectively the spin-split conductance, as we explain therein. We then study the angular dependence in this paradigm for a superconducting spin valve $F_1/N/F_2/S$ configuration. The work presented in this chapter is based on a previous publication Ref. [68] which has been edited for use in this thesis.

In Chapter 4 the spin current, spin transfer torque, and spin accumulation is studied for the superconducting spin valve. In this chapter, we review our methods and extend them to include the calculation of spin current quantities, which are spatially dependent within the multilayer. We analyze the spatial dependence of the spin transport quantities with respect to the applied bias as well as the physical parameters such as the interfacial scattering and layer thicknesses. We also analyze the spatially averaged spin torque and spin accumulation within each layer to generalize the bias dependence on the

spin transport. The work presented in this chapter is based on a previous publication Ref. [69] which has been edited for use in this thesis.

In Chapter 5 we study the $S/F/N/F/S$ Josephson structure. We present our numerical calculations and analysis on the quasiparticle current through the heterostructure to determine the conductance-bias relationship. We use an analytic approximation to study the simpler $N/F/S$ heterostructure in the context of multiple Andreev reflections to determine the thickness dependence of the conductance peaks. We then repeat this for the $S_1/F/S_2$ Josephson structure. We find that for the Josephson structures, there exists two sub-gap peaks which are a result of two different resonance effects. The conductance of the ferromagnetic Josephson structure $S_1/F_1/N/F_2/S_2$ is then calculated numerically and we determine the thickness dependence on F_2. We then find the angular dependence on the conductance to determine a possible valve effect in these structures.

In Chapter 6 we summarize and conclude the findings of the thesis chapters above.

Chapter 2

Conductance in Superconducting Spin Valves

2.1 Introduction

The work presented in this chapter is based on a previous publication Ref. [67] which has been edited for use in this thesis.

In this chapter we present our study on transport in ferromagnetic/superconducting heterostructures, namely the $F/N/F/S$ superconducting spin valve. Our primary goal is to describe the charge and spin transport properties within these heterostructures for realistic, fabricable devices. Recently, it has become possible to fabricate specialized spin valves by layering ferromagnetic (F) and superconducting (S) materials that can be modeled using a ballistic, clean limit theory. Much of the interest in these heterostructures comes from the antagonistic proximity effects, which we have discussed in Sec. 1.2. Spintronic devices of various kinds [4, 5, 6] have been proposed since. In this thesis, our focus is on the superconducting spin valve device. A traditional spin valve ($F_1/N/F_2$) is a spintronic, non-volatile magnetic memory device in which the memory state is determined by the relative orientation of the magnetization within the ferromagnets (F), also known as the misalignment angle [2]. The ferromagnets are separated by a normal metal spacer (N) such that the relative orientation of the ferromagnets can be altered. These spin valves are based on the Giant Magnetoresistive (GMR) effect [2, 3] and can switch memory states with an applied current via the spin

transfer torque (STT) [1]. The superconducting spin valve devices have been studied extensively [40, 41, 42] both theoretically and experimentally for their unique properties stemming from the F/S proximity effect [22]. The addition of a superconductor into the heterostructure also has the additional advantage of lowering the power consumption in applicable devices [70]. Here, we present our study of the transport properties and their dependencies on the physical parameters that govern real nanoscale devices and experimental samples.

Ferromagnetism and s-wave superconductivity would appear to be incompatible due to the opposite spin structure of their order parameters: the internal fields in the ferromagnets tend to break the singlet Cooper pairs. Indeed, although proximity effects do exist in F/S heterostructures, they are very different from those at N/S interfaces. The exchange field leads to the Cooper pairs acquiring a center of mass momentum [25] which results in damped oscillatory behavior of the singlet pair amplitudes in the F layer regions [26, 27]. This behavior is fundamentally important: it induces oscillations in most of the physical properties of these structures, including the dependence of the transition temperature [22] on the thickness of the various layers. It also drastically changes the behavior of transport quantities such as the the bias dependent conductance, discussed below.

An even more noteworthy phenomenon arising from the F/S proximity effects is that in certain F/S heterostructures triplet correlations may be induced, even though the S material is an s-wave superconductor [29, 30, 31, 32]. These triplet correlations are necessarily odd in frequency [33] or, equivalently, odd in time [31] as required by the Pauli principle. When the ferromagnetic exchange fields are all aligned only the $m_z = 0$ triplet component can be induced since S_z, the z component of the Cooper pair spin, commutes with the Hamiltonian. However, when there are two or more F layers with non-collinear exchange fields, as can happen for example in $F_1/F_2/S$ structures, S_z cannot commute with the Hamiltonian and the $m_z = \pm 1$ triplet states can also be induced. This is also the case with a single F layer having a non-uniform magnetization texture [45, 46, 71]. In contrast to the short-range proximity-induced singlet pair amplitudes, these odd $m_z = \pm 1$ triplet states are usually long ranged [23, 34, 35, 36, 37, 38, 39] in the F layers. Since they are induced by oscillatory singlet pairs, the triplet behavior is also oscillatory in nature. Because of this, the details of

the geometry of the F/S multilayers are crucial to determining their equilibrium [48] properties, including the oscillatory behavior of the transition temperature with layer thicknesses [9] and with the misalignment angle ϕ between the two F layers [9, 32] in a spin valve. As in a conventional spin valve, the relative exchange field orientation of the F layers can have a large effect on the conductance of the system [41]. The introduction of triplet correlations can lead to a nonmonotonic dependence of the conductance on ϕ, just as for equilibrium quantities.

Ultimately, all superconducting proximity effects are governed by Andreev reflection at the interfaces. Andreev reflection [49] is the process of electron-to-hole conversion by the creation or annihilation of a Cooper pair in the superconducting layer. In conventional Andreev reflection, the reflected electron/hole has opposite spin to the incident particle. However, it has been shown [41, 52, 53, 54, 55] that for F/S interfaces the triplet proximity effects are correlated with anomalous Andreev reflection, in which the reflected quasiparticle has the same spin as the incident one. From this, it follows that the proper consideration of Andreev reflection is essential in the description of the transport properties, as has long been recognized in both N/S [50, 51] and F/S [56, 57] systems. These effects are particularly important when examining the conductance in the subgap bias regime, where $eV < \Delta$.

In this chapter, we are motivated by the increasing interest in building actual, practical spin valve structures with potential use as part of magnetic memory elements. We therefore investigate the charge transport properties of a superconducting spin valve, an $F_1/N/F_2/S$ structure which includes the normal metal layer spacer This normal metal spacer is necessary in experiments in order to control the relative exchange field of the F layers through the use, for example, of a pinned and a soft ferromagnetic layer, in which the spacer decouples the ferromagnetic layers layers (see e.g. Ref. [9]). We will use typical values of the different thicknesses, as in existing and planned devices from our experimental collaborators, and we include realistic interfacial scattering between the different layers. Parameters such as the exchange field and coherence length will be taken to be in the range relevant to the materials actually used. These $F/N/F$ layers are grown on top of a superconducting substrate. This substrate must be thick enough to allow for the sample to be superconducting: its thickness must exceed the superconducting correlation length. Too thick, and the pair amplitude remains saturated to

near the bulk value and the proximity effect can not be seen as clearly. Therefore, we take the superconducting layer to be about one and a half times the coherence length of the superconductor. Furthermore, experimental constraints do not allow for perfect interfaces. Although recent developments in fabrication techniques [5] have allowed for very clean interfaces with ballistic transport properties, surface imperfections are unavoidable and even small interfacial scattering can have a large effect on the transport properties, as we shall see, since they affect both ordinary and Andreev scattering.

We will use a self consistent solution of the Bogoliubov deGennes (BdG) equations, discussed in Sec. 1.4, to calculate the conductance G as a function of bias voltage for realistic ranges of geometrical and material parameters, and as a function of the angle ϕ. Temperature corrections, which we will show to be non negligible, will also be studied. The conductance will be obtained from the self consistent solutions of the Hamiltonian, via a transfer matrix procedure which makes use of the Blonder-Tinkham-Klapwijk (BTK) method [50]. In some previous calculations [55, 72] of the conductance, a non self-consistent, step-function pair potential has been assumed. This neglects the very proximity effects which act on the singlet and triplet pair amplitudes, and thus the pair potential. In order to properly take these effects into account, one must use a self-consistent calculation of the pair potential. Even more important, only a self-consistent solution can guarantee that the conservation laws are satisfied [41], as we review in Sec. 2.2.3 below. The feasibility of the methods we use here was demonstrated in previous work [41] on simple $F/F/S$ heterostructures without N spacers or interfacial scattering, at $T = 0$. That work proved that the self-consistent BTK method embedded into a transfer matrix procedure can be used to calculate the conductance as well as the spin transport quantities. Our work presented here exploits these methods with a broader focus on realistic experimental parameters and sample compositions.

Because of the oscillatory nature of the superconducting singlet (and triplet) amplitudes in the F layers, we will see that the transport results are highly dependent on the layer thicknesses, as they are on the exchange field. We report on the ϕ dependence of the conductance as the angular spin valve effect of the system. We do so for a variety of thicknesses for the ferromagnetic and normal layers. Furthermore, we investigate the dependence of G on the interfacial scattering strengths at all the interfaces. The dependencies that we find are, as a rule, nonmonotonic, and therefore straightforward

extrapolations are not possible. Our goal is to provide a better understanding on the full range of experimentally relevant results where the interfacial quality cannot be perfectly controlled. From this, not only can one determine how these parameters affect the spin valve effect, but one can also provide the approximate set of parameters that can then maximize this effect: this has both experimental and technological importance. We investigate also, in a more restricted set of cases, the spin current and spin-transfer torque (STT). The results presented in this chapter will lay the groundwork for the experimentally parameterized spin transport calculations done in Chapter 4.

After this introduction, we review our methods for the transport calculations in Sec. 2.2, as well as give a brief summary of the equilibrium calculations presented in Sec. 1.4. The results are presented, chiefly in graphical form, in Sec. 2.3, and discussed in the proper context. A summary Sec. 2.4 closes the chapter.

2.2 Methods

2.2.1 The basic equations

The basic methods and procedures used are straightforward extensions of those discussed in Refs. [41] and [66]. We have also presented our methods for calculating the thermodynamic quantities in Sec. 1.4 using the Bogoliubov deGennes transformation and eigenvalue equations [15, 18]. We present only a summary of these methods as a way to establish notation and to drive the main points from which our calculations follow. The geometry of the system under consideration is represented qualitatively in Fig. 1.3. The layers are assumed to be infinite in the transverse direction. The y-axis is normal to the layers: this somewhat unconventional choice turns out to be computationally convenient because only the σ_y Pauli matrix is complex. The magnetizations of the outer and inner layers form an angle ϕ with each other.

The Hamiltonian appropriate to our system is given by Eq. 1.19 and is described in detail in Sec. 1.4. The Hamiltonian for the multilayer system includes the Stoner exchange field $\mathbf{h}$ which is vanishing in the N and S layers, as well as the pair potential Δ which is nonvanishing in S only. It also includes the single particle Hamiltonian which includes interfacial scattering in the form of delta function potentials with barrier H_i for each interface. We assume $h_1 = h_2 \equiv h$ since in most experiments

the same material is employed. Performing a generalized Bogoliubov transformation $\psi_\sigma = \sum_n \left(u_{n\sigma}\gamma_n - \eta_\sigma v^*_{n\sigma}\gamma^\dagger_n \right)$, where $\eta_\sigma \equiv 1(-1)$ for spin-up (down), and taking advantage of the quasi one dimensional geometry one can recast the eigenvalue equation corresponding to the Hamiltonian given by Eq. 1.19, as done in Sec. 1.4.

$$\begin{pmatrix} H_0 - h_z & -h_x & 0 & \Delta \\ -h_x & H_0 + h_z & \Delta & 0 \\ 0 & \Delta & -(H_0 - h_z) & -h_x \\ \Delta & 0 & -h_x & -(H_0 + h_z) \end{pmatrix} \begin{pmatrix} u_{n\uparrow} \\ u_{n\downarrow} \\ v_{n\uparrow} \\ v_{n\downarrow} \end{pmatrix} = \epsilon_n \begin{pmatrix} u_{n\uparrow} \\ u_{n\downarrow} \\ v_{n\uparrow} \\ v_{n\downarrow} \end{pmatrix}, \qquad (2.1)$$

with the $u_{n\sigma}(y)$ and $v_{n\sigma}(y)$ being the usual position and spin dependent quasiparticle and quasihole amplitudes as described in Sec. 1.4. Each term represented above is implicitly a function of y which we had dropped from our notation for readability. We use units such that $\hbar = k_B = 1$. The quasi one dimensional Hamiltonian is $H_0 = -(1/2m)(d^2/dy^2) + \epsilon_\perp - E_F(y) + U(y)$ where $\epsilon_\perp$ is the transverse energy, (so that Eq. 2.1 is a set of decoupled equations, one for each $\epsilon_\perp$). $U(y)$ is the interfacial scattering. We take this scattering, due to unavoidable surface roughness at the interfaces, to be spin-independent and of the form $U(y) = H_1\delta(y - d_{f1}) + H_2\delta(y - d_{f1} - d_N) + H_3\delta(y - d_{f1} - d_N - d_{f2})$. The dimensionless parameters $H_{Bi} \equiv H_i/v_F$, where v_F is the Fermi speed in S, conveniently characterize the strength of the delta functions. $E_F(y)$ is the layer dependent width of the band as discussed in Sec. 1.4. We assume the mismatch parameter [65] to be $\Lambda = 1$ and we subsume its effects into the interfacial scattering strengths.

All calculations must be performed self-consistently, otherwise a large part of the proximity effect is eliminated from the problem. As previously shown [41, 62, 63, 64], and as reiterated in Section 2.2.3, it is paramount to perform the transport calculations self-consistently: not doing so jeopardizes the law of conservation of charge [73]. The self consistency condition is:

$$\Delta(y) = \frac{g(y)}{2} {\sum_n}' \left[u_{n\uparrow}(y) v^*_{n\downarrow}(y) + u_{n\downarrow}(y) v^*_{n\uparrow}(y) \right] \tanh\left(\frac{\epsilon_n}{2T} \right), \qquad (2.2)$$

where the sum is over all the eigenvalues and the prime in the sum denotes, as usual, that the sum is limited to states with eigenenergies within a cutoff ω_D from the Fermi level.

The superconducting coupling constant $g(y)$, in the singlet channel, is nonvanishing in S only. Self consistency is achieved by starting with a suitable choice of $\Delta(y)$ and iterating Eqs. (2.1) and (2.2) until the input and output values of $\Delta(y)$ coincide. The thermodynamic quantities can then be derived from the wave functions. The transition temperature itself can be most conveniently obtained by linearization of Eq. (2.2) and an efficient eigenvalue technique [31, 40] as in previous [9] work.

2.2.2 Transport: the BTK method and self-consistency

After the self consistent $\Delta(y)$ function has been obtained as reviewed in Sec. 1.4 and above, one can proceed with the calculation of the transport properties. We use the BTK formalism [50] to evaluate the conductance. We first calculate the reflection and transmission amplitudes for incoming electrons traveling perpendicular to the plane of our heterostructure and then use the BTK method to extract the conductance, in Sec. 2.2.4, which is given in terms of the spin dependent Andreev and ordinary reflection amplitudes $a_{\sigma,\sigma'}$ and $b_{\sigma,\sigma'}$ respectively. The methods used are the same as those used in previous work [41] and are extended here to include interfacial scattering and a normal metal layer N.

We start by describing the wavefunctions within each layer. For an incident particle with spin up the wavefunction in F_1 is:

$$\Psi_{F1,\uparrow} \equiv \begin{pmatrix} e^{ik^{+}_{\uparrow 1}y} + b_{\uparrow,\uparrow}e^{-ik^{+}_{\uparrow 1}y} \\ b_{\downarrow,\uparrow}e^{-ik^{+}_{\downarrow 1}y} \\ a_{\uparrow,\uparrow}e^{ik^{-}_{\uparrow 1}y} \\ a_{\downarrow,\uparrow}e^{ik^{-}_{\downarrow 1}y} \end{pmatrix} \tag{2.3}$$

where we have included the appropriate amplitudes for the ordinary and Andreev reflection processes $b_{\sigma,\uparrow}$ and $a_{\sigma,\uparrow}$, which we must calculate. The first spin index of the reflection amplitudes denotes the spin of the reflected particle, while the second spin index denotes the spin of the incoming particle. If the incident particle has spin down,

the corresponding wavefunction in F_1 is

$$\Psi_{F1,\downarrow} \equiv \begin{pmatrix} b_{\uparrow,\downarrow} e^{-ik^+_{\uparrow 1} y} \\ e^{ik^+_{\downarrow 1} y} + b_{\downarrow,\downarrow} e^{-ik^+_{\downarrow 1} y} \\ a_{\uparrow,\downarrow} e^{ik^-_{\uparrow 1} y} \\ a_{\downarrow,\downarrow} e^{ik^-_{\downarrow 1} y} \end{pmatrix} \tag{2.4}$$

with appropriate amplitude coefficients, numerically different from those for the spin up incident particle. Each set of coefficients is calculated separately for incident spin-up and spin-down electrons. One has, in the above equations:

$$k^{\pm}_{\sigma 1} = \left[\Lambda(1 - \eta_\sigma h_1) \pm \epsilon - k^2_\perp\right]^{1/2}, \tag{2.5}$$

where $\eta_\sigma \equiv 1(-1)$ for up (down) spins, and $k_\perp$ is the wavevector corresponding to energy $\epsilon_\perp$. All wavevectors are understood to be in units of k_{FS} and all energies in terms of E_{FS}.

All of the amplitudes are then determined from the transfer matrix procedure discussed in Ref. [41], where the self-consistent pair potential determines the wavevectors in the S layer. The transfer matrix matches the continuity conditions for each layer. In the F_1 layer there are only four coefficients for left moving plane wave particle reflections (and right moving holes). For the intermediate layers, the eigenfunctions contain both left- and right-moving plane waves. Thus the wavefunction for intermediate F_2 layer has eight unknown coefficients c_n [41],

$$\Psi_{F2} \equiv \begin{pmatrix} c_1 f^+_\uparrow e^{ik^+_{\uparrow 2} y} + c_2 f^+_\uparrow e^{-ik^+_{\uparrow 2} y} + c_3 g^+_\uparrow e^{ik^+_{\downarrow 2} y} + c_4 g^+_\uparrow e^{-ik^+_{\downarrow 2} y} \\ c_1 f^+_\downarrow e^{ik^+_{\uparrow 2} y} + c_2 f^+_\downarrow e^{-ik^+_{\uparrow 2} y} + c_3 g^+_\downarrow e^{ik^+_{\downarrow 2} y} + c_4 g^+_\downarrow e^{-ik^+_{\downarrow 2} y} \\ c_5 f^-_\uparrow e^{ik^-_{\uparrow 2} y} + c_6 f^-_\uparrow e^{-ik^-_{\uparrow 2} y} + c_7 g^-_\uparrow e^{ik^-_{\downarrow 2} y} + c_8 g^-_\uparrow e^{-ik^-_{\downarrow 2} y} \\ c_5 f^-_\downarrow e^{ik^-_{\uparrow 2} y} + c_6 f^-_\downarrow e^{-ik^-_{\uparrow 2} y} + c_7 g^-_\downarrow e^{ik^-_{\downarrow 2} y} + c_8 g^-_\downarrow e^{-ik^-_{\downarrow 2} y} \end{pmatrix}, \tag{2.6}$$

where $k^{\pm}_{\uparrow 2}$ and $k^{\pm}_{\downarrow 2}$ are defined in Eq. (2.5) replacing h_1 with h_2. The eigenspinors f and g, for $0 \le \phi \le \pi/2$ are given by

$$\begin{pmatrix} f^+_\uparrow \\ f^+_\downarrow \end{pmatrix} = \frac{1}{\mathcal{N}} \begin{pmatrix} 1 \\ \frac{1-\cos\phi}{\sin\phi} \end{pmatrix} = \begin{pmatrix} f^-_\uparrow \\ -f^-_\downarrow \end{pmatrix}; \quad \begin{pmatrix} g^+_\uparrow \\ g^+_\downarrow \end{pmatrix} = \frac{1}{\mathcal{N}} \begin{pmatrix} -\frac{\sin\phi}{1+\cos\phi} \\ 1 \end{pmatrix} = \begin{pmatrix} -g^-_\uparrow \\ g^-_\downarrow \end{pmatrix} \tag{2.7}$$

with the normalization constant $\mathcal{N} = \sqrt{2/1+\cos\phi}$. For $\pi/2 \leq \phi \leq \pi$ they are given by

$$\begin{pmatrix} f_\uparrow^+ \\ f_\downarrow^+ \end{pmatrix} = \frac{1}{\mathcal{N}} \begin{pmatrix} \frac{\sin\phi}{1-\cos\phi} \\ 1 \end{pmatrix} = \begin{pmatrix} -f_\uparrow^- \\ f_\downarrow^- \end{pmatrix}; \quad \begin{pmatrix} g_\uparrow^+ \\ g_\downarrow^+ \end{pmatrix} = \frac{1}{\mathcal{N}} \begin{pmatrix} 1 \\ -\frac{1+\cos\phi}{\sin\phi} \end{pmatrix} = \begin{pmatrix} g_\uparrow^- \\ -g_\downarrow^- \end{pmatrix} \tag{2.8}$$

with $\mathcal{N} = \sqrt{2/1-\cos\phi}$.

The S layer is split into multiple sublayers S_i. Each sublayer has eight coefficients, $t_{n,i}$ and $\bar{t}_{n,i}$ [41],

$$\Psi_{Si} \equiv \begin{pmatrix} t_{1i}u_i e^{ik_i^+ y} + \bar{t}_{1i}u_i e^{-ik_i^+ y} + t_{4i}v_i e^{-ik_i^- y} + \bar{t}_{4i}v_i e^{ik_i^- y} \\ t_{2i}u_i e^{ik_i^+ y} + \bar{t}_{2i}u_i e^{-ik_i^+ y} + t_{3i}v_i e^{-ik_i^- y} + \bar{t}_{3i}v_i e^{ik_i^- y} \\ t_{2i}v_i e^{ik_i^+ y} + \bar{t}_{2i}v_i e^{-ik_i^+ y} + t_{3i}u_i e^{-ik_i^- y} + \bar{t}_{3i}u_i e^{ik_i^- y} \\ t_{1i}v_i e^{ik_i^+ y} + \bar{t}_{1i}v_i e^{-ik_i^+ y} + t_{4i}u_i e^{-ik_i^- y} + \bar{t}_{4i}v_i e^{ik_i^- y} \end{pmatrix}, \tag{2.9}$$

where $k_i^\pm = \left[1 \pm \sqrt{\epsilon^2 - \Delta_i^2} - k_\perp^2\right]^{1/2}$, and Δ_i represents the strength of the self consistent pair potential in the ith superconducting layer. The superconducting coherence factors u_i and v_i are given by

$$\sqrt{2}u_i = \left[\left(\epsilon + \sqrt{\epsilon^2 - \Delta_i^2}\right)/\epsilon\right]^{1/2} \sqrt{2}v_i = \left[\left(\epsilon - \sqrt{\epsilon^2 - \Delta_i^2}\right)/\epsilon\right]^{1/2} \tag{2.10}$$

The final, right-most sublayer of the superconductor has the additional boundary condition which allows for only right-moving quasiparticles and left-moving quasiholes, with four unknown coefficients which are the same as those in Eq. (2.9) taking the $\bar{t}_n$ amplitudes to be zero.

We apply the continuity condition at each interface $\Psi_{F1}(d_{F1}) = \Psi_N(d_{F1})$, $\Psi_N(d_F + d_N) = \Psi_{F_2}(d_F + d_N)$, etc. The conditions on their derivatives are $\partial\Psi_{F1}(d_{F1})/\partial y = \partial\Psi_N(d_{F1})/\partial y + 2H_B\Psi_N(d_{F1})$ and similarly for each interface. We can use a transfer matrix method to write these as 8×8 matrices $\mathcal{M}_i$ multiplied by their respective vector of unknown coefficients x_i for each layer i, as was explained in Ref. [41]. Then, $\mathcal{M}_{F1}x_{F1,\sigma} + c_{F1} = \mathcal{M}_{N,l}x_N$ and $\mathcal{M}_{N,r}x_N = \mathcal{M}_{F2,l}x_{F2}$ etc, where (l,r) denote that the wavefunctions are evaluated on the left or right side of the layer respectively and σ

denotes the spin of the incoming electron in the F_1 layer. $c_{F1,\sigma}$ represents the incoming spin σ electron term in Ψ_{F1}. We can incorporate a self-consistent pair potential by splitting the S layer into infinitesimal sublayers S_i such that the continuity equations become $\mathcal{M}_{F2,r}x_{F2} = \mathcal{M}_{S_0,l}x_{S_0}$, $\mathcal{M}_{S_0,r}x_{S_0} = \mathcal{M}_{S_1,l}x_{S_1}$ etc until we reach the last sublayer. By solving and eliminating the intermediate layer coefficients, we find the reflection amplitudes $b_{\sigma,\sigma'}$ and $a_{\sigma,\sigma'}$ which we use to extract the conductance in Sec. 2.2.4. We can also use the coefficients of each layer to determine the wavefunction $\Psi_n(y) = (u_{n\uparrow}(y), u_{n\downarrow}(y), v_{n\uparrow}(y), u_{n\uparrow}(y))^\intercal$, which can be used to calculate the spin transport quantities. Since these quantities are spatially dependent, it is convenient to solve for all unknown coefficients simultaneously, which improves upon numerical precision. This can be done by recasting the transfer matrices to the form $Ax + c_\sigma = 0$ where A is an $8(N-1) \times 8(N-1)$ matrix for N layers, x is the $8(N-1) \times 1$ vector of the unknown coefficients, and c_σ represents the incoming particle of spin σ. Eq. (29) of Ref. [74] relates the $\mathcal{M}$ transfer matrices of each sublayer to the matrix A and we refer the reader there for more details.

2.2.3 Conservation laws and conductance

In transport calculations great care has to be taken not to violate [73] the conservation laws. Consider the equation for charge density $\rho(\mathbf{r}, t)$ which arises from the Heisenberg equation:

$$\frac{\partial}{\partial t} \langle \rho(\mathbf{r}) \rangle = i \langle [\mathcal{H}_{eff}, \rho(\mathbf{r})] \rangle . \tag{2.11}$$

We are considering here steady state situations, so the time derivative vanishes and we simply should have a zero divergence condition for the current. In our quasi one dimensional geometry, the only non-vanishing component of the current is j_y, and it depends only on y. Hence we need to ensure that $\partial j_y/\partial y = 0$. Upon computing the commutator in the right side of Eq. (2.11) under these conditions we find, however:

$$\frac{\partial j_y(y)}{\partial y} = 2e\mathrm{Im}\left\{ \Delta(y) \sum_n \left[u^*_{n\uparrow} v_{n\downarrow} + u^*_{n\downarrow} v_{n\uparrow} \right] \tanh\left(\frac{\epsilon_n}{2T} \right) \right\} \tag{2.12}$$

In transport calculations the wavefunctions cannot be taken to be real, as is possible

for the evaluation of static quantities in a current-free situation. Hence it is not necessarily true that the right side of Eq. (2.12) will vanish. However, it is easy to see [41, 63] that it will be identically zero when the self consistency condition Eq. (2.2) is satisfied. In the non-equilibrium case, the continuity condition is more complicated and involves the interchange between quasi-particle current density and the supercurrent density [41, 50] which is only accounted for in the self consistent theory. Therefore, the importance of performing the calculations self consistently, despite the computational simplifications inherent to non-self-consistent methods, cannot be overemphasized.

2.2.4 Extraction of the conductance

From the results of the previous subsection, one can extract the conductance. The current is related to the applied bias [50] V via the expression:

$$I(V) = \int G_0(\epsilon) \left[f\left(\epsilon - eV\right) - f\left(\epsilon\right) \right] d\epsilon, \tag{2.13}$$

where f is the Fermi function. The bias dependent conductance is $G(V) = \partial I / \partial V$. The function G_0 in Eq. (2.13) is the conductance in the low-T limit or, more generally, the conductance obtained by replacing the derivative of the Fermi function by a δ function. It is related to the scattering amplitudes by:

$$\begin{aligned} G_0(\epsilon, \theta_i) &= \sum_\sigma P_\sigma G_\sigma(\epsilon, \theta_i) \\ &= \sum_\sigma P_\sigma \left(1 + \frac{k^-_{\uparrow 1}}{k^+_{\sigma 1}} |a_{\uparrow,\sigma}|^2 + \frac{k^-_{\downarrow 1}}{k^+_{\sigma 1}} |a_{\downarrow,\sigma}|^2 - \frac{k^+_{\uparrow 1}}{k^+_{\sigma 1}} |b_{\uparrow,\sigma}|^2 - \frac{k^+_{\downarrow 1}}{k^+_{\sigma 1}} |b_{\downarrow,\sigma}|^2 \right), \end{aligned} \tag{2.14}$$

in the customary natural units of conductance (e^2/h). In Eq. (2.14) the different k symbols are as defined in Eq. (2.5). The angle θ_i is the angle of incidence: for spin up it is given by $\tan\theta_i = (k_\perp / k^+_{\uparrow 1})$, and similarly for spin down. Thus one has $\theta_i = 0$ for the forward conductance. The factors $P_\sigma \equiv (1 - h_1 \eta_\sigma)/2$ are included to take into account the different density of incoming spin up and spin down states. The energy dependence of $G(\epsilon)$ arises from the applied bias voltage V. It is customary and convenient to measure this bias in terms of the dimensionless quantity $E \equiv eV/\Delta_0$ where Δ_0 is the

value of the order parameter in bulk S material. We will refer to the dimensionless bias dependent conductance simply as $G(V)$ or $G(E)$ usually omitting the angular argument for the forward conductance.

One can not always assume that the experiments are performed in the low T limit. At finite temperature there are two sources of T corrections. The first and more obvious is that arising from the T dependence of $\Delta(y)$, that is, the T dependence of the effective BCS Hamiltonian. This is of course straightforward to include: one just calculates the self consistent Δ at finite T (see Eq. (2.2) and uses it as input in the transfer matrix calculations. But there is also a temperature dependence arising from the Fermi function in Eq. (2.13). If the temperature is not too close to T_{c0}, the transition temperature of the bare S material which sets the overall scale, one can use a Sommerfeld type expansion. Because the energy scale over which $G(V)$ varies is of order Δ_0, the relevant expansion parameter is T/T_{c0}, not T/T_F, and hence not necessarily negligibly small in all experimental situations. One finds using elementary [75] methods:

$$G(V,T) = G_0(V) + a_1 \left(\frac{T}{\Delta_0}\right)^2 \left(\frac{\partial^2 G(V)}{\partial \epsilon^2}\right)\Big|_{\epsilon=V} + \mathcal{O}\left(\frac{T}{\Delta_0}\right)^4 \tag{2.15}$$

where a_1 can be expressed [75] in terms of a Bernoulli number. Alternatively, one can use the general form:

$$G(V,T) = \frac{1}{4T}\int dV' \frac{1}{\cosh^2[(1/2T)(V-V')]} G_0(V'). \tag{2.16}$$

In Eqs. (2.15) and (2.16) $G_0(V)$ means the result of Eq. (2.14) evaluated with the self consistent pair potential at temperature T. The second form turns out to be more useful as most relevant temperatures turn out to be too high for the Sommerfeld expansion.

2.2.5 Spin transport

We will also consider spin transport here in order to lay the groundwork for a more detailed discussion in Chapter 4. In our quasi one-dimensional geometry the tensorial spin current becomes a vector in spin space, while spatially it depends only on y. Denoting

this vector as $\vec{S}(y)$ it can be written [41] in terms of the wavefunctions, as:

$$S_i \equiv \frac{i\mu_B}{2m}\sum_\sigma \left\langle \psi^\dagger_\sigma \sigma_i \frac{\partial \psi_\sigma}{\partial y} - \frac{\partial \psi^\dagger_\sigma}{\partial y}\sigma_i \psi_\sigma \right\rangle . \tag{2.17}$$

It is not difficult to write the components S_i in terms of the u_n and v_n wavefunctions. In the $T = 0$ limit, the result is [41]:

$$\begin{aligned}
S_x =& \frac{-\mu_B}{m}\mathrm{Im}\left[\sum_n \left(-v_{n\uparrow}\frac{\partial v^*_{n\downarrow}}{\partial y} - v_{n\downarrow}\frac{\partial v^*_{n\uparrow}}{\partial y}\right)\right. && (2.18a)\\
&\left. + \sum_{\epsilon_{\mathbf{k}}<eV}\left(u^*_{\mathbf{k}\uparrow}\frac{\partial u_{\mathbf{k}\downarrow}}{\partial y} + v_{\mathbf{k}\uparrow}\frac{\partial v^*_{\mathbf{k}\downarrow}}{\partial y} + u^*_{\mathbf{k}\downarrow}\frac{\partial u_{\mathbf{k}\uparrow}}{\partial y} + v_{\mathbf{k}\downarrow}\frac{\partial v^*_{\mathbf{k}\uparrow}}{\partial y}\right)\right] \\
S_y =& \frac{\mu_B}{m}\mathrm{Re}\left[\sum_n \left(-v_{n\uparrow}\frac{\partial v^*_{n\downarrow}}{\partial y} + v_{n\downarrow}\frac{\partial v^*_{n\uparrow}}{\partial y}\right)\right. && (2.18b)\\
&\left. + \sum_{\epsilon_{\mathbf{k}}<eV}\left(u^*_{\mathbf{k}\uparrow}\frac{\partial u_{\mathbf{k}\downarrow}}{\partial y} + v_{\mathbf{k}\uparrow}\frac{\partial v^*_{\mathbf{k}\downarrow}}{\partial y} - u^*_{\mathbf{k}\downarrow}\frac{\partial u_{\mathbf{k}\uparrow}}{\partial y} - v_{\mathbf{k}\downarrow}\frac{\partial v^*_{\mathbf{k}\uparrow}}{\partial y}\right)\right] \\
S_z =& \frac{-\mu_B}{m}\mathrm{Im}\left[\sum_n \left(v_{n\uparrow}\frac{\partial v^*_{n\uparrow}}{\partial y} - v_{n\downarrow}\frac{\partial v^*_{n\downarrow}}{\partial y}\right)\right. && (2.18c)\\
&\left. + \sum_{\epsilon_{\mathbf{k}}<eV}\left(u^*_{\mathbf{k}\uparrow}\frac{\partial u_{\mathbf{k}\uparrow}}{\partial y} - v_{\mathbf{k}\uparrow}\frac{\partial v^*_{\mathbf{k}\uparrow}}{\partial y} - u^*_{\mathbf{k}\downarrow}\frac{\partial u_{\mathbf{k}\downarrow}}{\partial y} + v_{\mathbf{k}\downarrow}\frac{\partial v^*_{\mathbf{k}\downarrow}}{\partial y}\right)\right],
\end{aligned}$$

where the first terms in the right side are the spin current components in the absence of bias. A static spin transfer current may exist near the boundary of two magnets with misaligned fields. The above results are valid at low T, and we will not consider temperature corrections for this quantity. In the steady state the conservation laws require:

$$\frac{\partial}{\partial y}S_i = \tau_i, \quad i = x, y, z \tag{2.19}$$

where $\boldsymbol{\tau}$ is the torque $\boldsymbol{\tau} \equiv 2\mathbf{m} \times \mathbf{h}$ with $\mathbf{m}$ being the local magnetization $\mathbf{m} = -\mu_B \sum_\sigma \langle \psi^\dagger_\sigma \boldsymbol{\sigma} \psi_\sigma \rangle$. The expression for $\mathbf{m}$ in terms of the wavefunctions is given in Ref. [41].

2.3 Results

In this section we present our results. As discussed in the Introduction, our emphasis is in exploring a range of values of experimental interest for the relevant parameters. This, in addition to helping us meet our goal of helping experimentalists understand their data, will keep the discussion within reasonable bounds: otherwise, with a more than ten-dimensional parameter space to be investigated, this work would completely lose its focus. We do have an extensive and growing database of results for many other cases. In Chapter 3 we will go into more detail on the conductance dependence on select parameters. As mentioned above, we use dimensionless parameters in our plots: all lengths are given in units of k_{FS} and all energies in units of E_{FS} except, as already stated, for the bias. Dimensionless lengths will be denoted by capital letters with the appropriate subscript. The units for the dimensionless barrier height parameters H_{Bi} have been explained before. Values close to unity or higher would represent a strong tunneling limit: these would be experimentally very undesirable as the proximity effects would be very small. Zero values represent an ideal interface, which is unlikely to be attainable experimentally. Since the first and second interfaces are both between F and N materials, one can fairly safely assume that these two barrier strengths are similar, and we will usually take them to be identical, $H_{B1} = H_{B2} \equiv H_B$. In our dimensionless units a field parameter value of $h = 1$ would correspond to a half metal. The results for G presented are for $h = 0.145$ a value previously found adequate [9] in fitting Co static properties in similar devices. As in Ref. [9], we subsume some of the wavevector mismatch effects with the phenomenological H_{Bi} parameters. We will also assume a value of $\Xi_0 = 115$ for the dimensionless correlation length in S, a value used in the same context [9] for Nb. We will vary the thicknesses of all layers, keeping D_{F2} relatively small, which is necessary to obtain good proximity effect, and allowing D_N and D_{F1} to be somewhat larger. As to D_S, the thickness of the superconducting layer, it must of course be kept above Ξ_0: otherwise the sample tends to become non-superconducting, for rather obvious reasons. We will focus here on forward conductance results ($\theta = 0$), which can be obtained from point probes and involve trends much easier to understand.

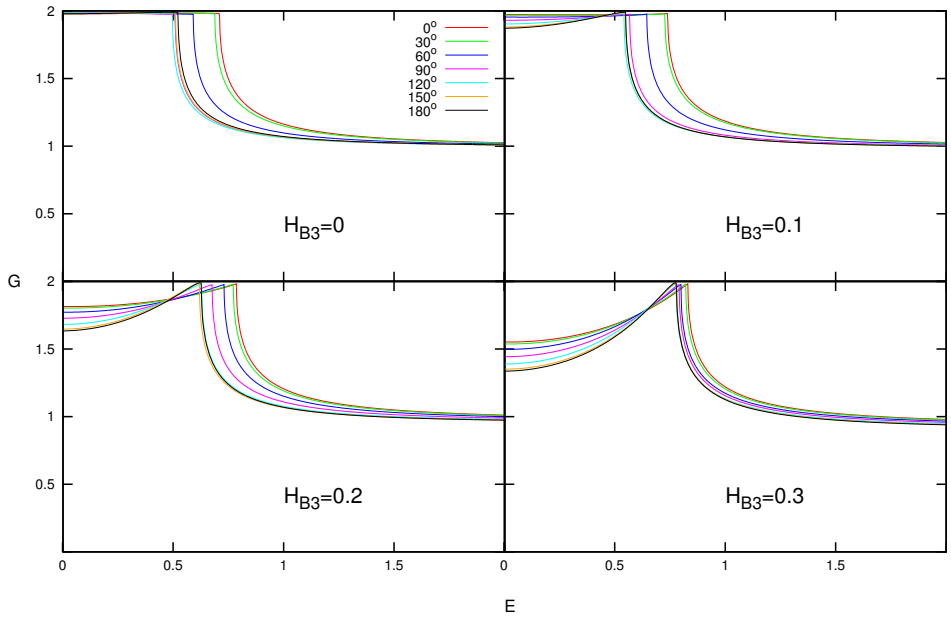

Figure 2.1: Effect on the conductance of the barrier between the superconductor and the inner ferromagnet H_{B3}. The four panels show results for G in natural units, as a function of bias voltage $E \equiv eV/\Delta_0$ at seven values of the misalignment angle ϕ as indicated in the legend. The panels correspond to different values of H_{B3} ranging from 0.0 to 0.3 with $H_{B1} = H_{B2} \equiv H_B = 0$. The thicknesses are $D_{F1} = 20$, $D_N = 40$, $D_{F2} = 12$ and $D_S = 180$. The internal field parameter is $h = 0.145$

2.3.1 Barrier effects

The effects of interfacial scattering are very strong and important. Recall that even in standard normal-superconductor interfaces the zero bias conductance (ZBC) can vary between a value of two for a perfect interface, and an exponentially small value for the tunneling limit. One should recall here that even in the case where the barrier parameter is zero there is still scattering at the N/F and F/S interfaces: this is because it is impossible for the two Fermi wavevectors in the ferromagnets to match the Fermi wavevector of either the N or the S materials. This has to be kept in mind in the discussion below.

In Fig. 2.1 we show the effect of increasing H_{B3} assuming that the other interfaces

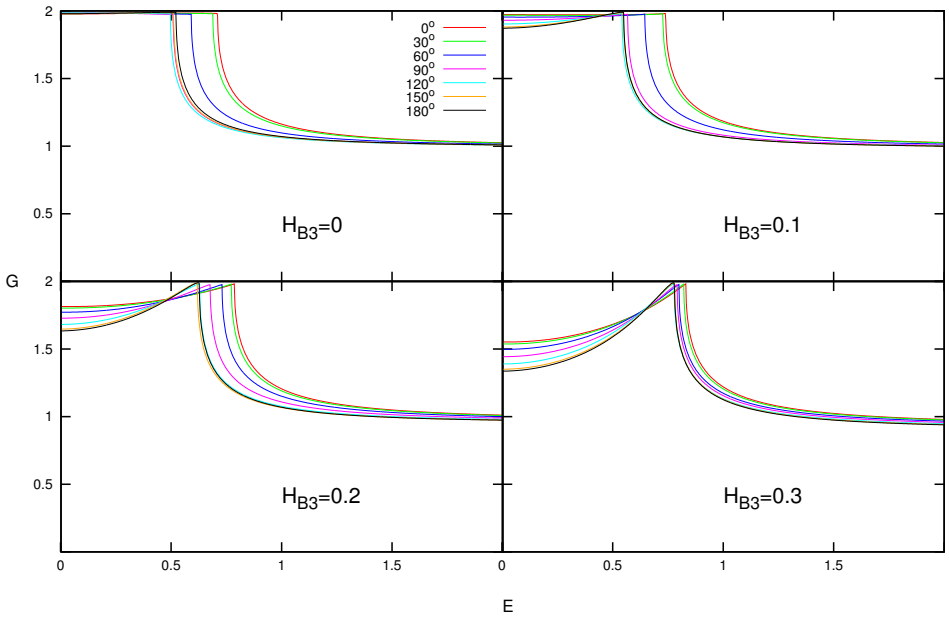

Figure 2.2: Effect on the conductance of the barriers between the normal spacer and the ferromagnets $H_{B1} = H_{B2} = H_B$. The four panels show results for the same arrangement as in Fig. 2.1 and the same geometrical and field parameters except in this case H_{B3} is held constant and the value of the barrier parameter at the other two interfaces is varied between 0.1 and 0.4.

have zero interfacial scattering potential, although scattering due to wavevector mismatches is present. Four values of H_{B3} are studied, one in each panel, and curves for seven values of the misalignment angle ϕ are plotted. The geometrical parameters are $D_{F1} = 20$, $D_N = 40$, $D_{F2} = 12$ and $D_S = 180$. The overall trend on increasing H_{B3} is a marked decrease of the low bias conductance and a much smaller decrease of the high bias limiting value. The critical bias (CB) is the value of the bias at which G sharply changes behavior and begins trending towards its normal state limit. In general, the critical bias is smaller than unity, and smaller values are associated with stronger proximity effects since the CB is associated with the saturated value of $\Delta(Y)$ well inside S. We see that the CB tends to increase with H_{B3}, while the value of G at critical bias (the critical bias conductance, CBC) remains nearly the same. On the other hand, the CB is

in all cases a strong function of ϕ, decreasing as ϕ increases, up to just above $\phi = 100°$ and then flattening, for this geometry. The dependence is less marked at higher barrier values. The ZBC however, is monotonically decreasing in ϕ. This dependence on ϕ is different from that of the CB or CBC, and it leads to a crossover in the conductance values. Remarkably, this crossover tends to occur with a "nodal" behavior at a single bias value in the subgap region: this can best be seen in the third and fourth panels. Monotonic behavior in the ZBC also occurs for other values of D_{F2} that we have studied, but the direction (increasing or decreasing in ϕ) is reversed in an oscillatory way: for example the ZBC increases with ϕ at values of D_{F2} of 7 and 10 and again at 16, 17. This is one more example of the multiple oscillatory behavior found in this problem and an illustration of how much care one has to take before extrapolating results.

Next we consider, in Fig. 2.2, the effect of increasing $H_{B1} = H_{B2} \equiv H_B$ while keeping $H_{B3} = 0$ at the F_2/S interface. Again, four barrier values are considered, in an arrangement very similar to that in the previous figure. The effects of interfacial scattering are now more pronounced. This is not necessarily due to the presence of two barriers: as in well known situations in elementary one-dimensional quantum mechanics, we find that having more barriers does not necessarily lead to less transparency. This analogy is imperfect: our system is not one-dimensional, there are multiple scattering mechanisms (interfacial imperfections, wavevector mismatch, Andreev reflection, etc). Still, we find that having two barriers does not always reduce transmission. A clear example of this can be seen in the ZBC value which, for the chosen values of $D_{F2} = 12$ and D_N, is nearly independent of H_B. This means there is a resonance-like behavior in this geometry. Furthermore, changing the values of $D_{F2} = 12$ and D_N leads to ZBC behavior more similar to that in Fig. 2.1, which we discuss in the next subsection in connection with Fig. 2.5. The behavior of the CB with angle is nonmonotonic, in a way similar to that found in Fig. 2.1. The minimum is now somewhat less shallow, particularly at higher H_B. At low bias, G decreases as the bias is increased, although an upturn does occur as the CB is approached albeit at a lower value of the CBC for increasing H_B. This is in contrast to Fig. 2.1 where the CBC was unaffected by H_{B3}.

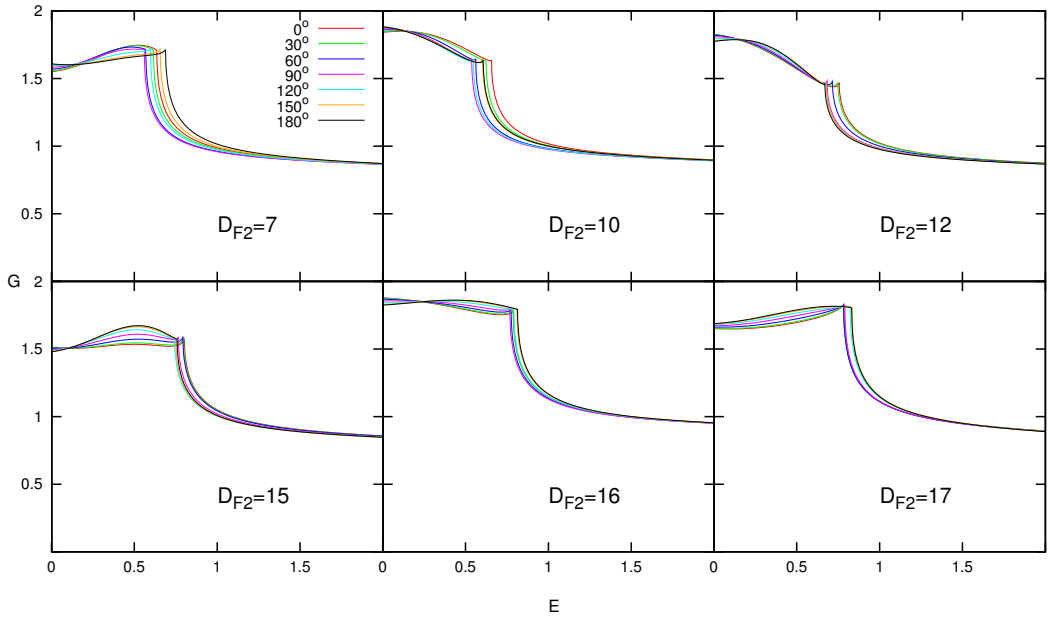

Figure 2.3: Effect on the conductance by varying the thickness D_{F2} of the inner ferromagnetic layer. The values of the other thicknesses, field, and correlation length are as in the previous two figures, and the barrier values are set to 0.3, 0.3, and 0.1 respectively, which are representative of possible experimental values. The six panels show G vs bias voltage for several angles, at six values of $D_{F2} = 7, 10, 12, 15, 16,$ and 17. The spin valve effect varies significantly in both the CB and the ZBC.

2.3.2 Geometrical Effects

We have mentioned in the previous discussion that the thickness of the different layers may have a strong and often nonmonotonic effect on G. The thickness of the inner magnetic layer, D_{F2} turns out to be the more important of these geometrical variables. In the six panels in Fig. 2.3 we consider increasing values of D_{F2} while keeping the other geometrical and material parameters fixed to their values in the previous figures. The three interfacial barrier parameters are set to intermediate values (see the caption).

Consider in detail the first panel, where $D_{F2} = 7$. One notices immediately the reduction in ZBC, as opposed to the results for $D_{F2} = 12$ in the third panel or to those in the previous figures. The behavior of this reduction occurs, as has been mentioned

above, in an oscillatory manner with D_{F2}: it can be seen again at $D_{F2} = 15$ (fourth panel). In this panel, as in the second and the fifth, the minimum value of the CB with angle is at $\phi = 90°$, and this minimum is very well marked – this is an optimum situation for valve effects. The ZBC value depends somewhat on ϕ but not in the same way as the CB: hence, the crossing conductance curves near a bias of 0.2. The second panel exhibits similar behavior, but the ZBC is markedly higher. On further increasing D_{F2} to 12 (third panel) the CB becomes monotonic in ϕ while the low bias conductance does not change: indeed the node where the lines cross barely moves. The case $D_{F2} = 15$ (fourth panel) is yet different: the CB is larger and there is a marked "bump" in the low bias conductance, the height of which increases with ϕ. Resonance in the ZBC is observed again in the fifth panel, and the angular dependence of the CB returns to having a marked minimum at $\phi = 90°$ although with a weaker dependence. Furthermore, the node noticeably moves to a higher bias value. Finally, at $D_{F2} = 17$ (last panel) the ZBC drops again, the angular dependence of the CB is reversed, and the node disappears. Thus we see that the thickness of the inner magnetic layer is a very important variable in determining the conductance properties.

On the other hand, the effect of varying D_{F1}, the thickness of the outer ferromagnetic layer, is much weaker than that of varying D_{F2}. This is illustrated in the first two panels of Fig. 2.4. There we display, in each panel, results for G at fixed $\phi = 0$. In the first panel we do this for several values of D_{F1} ranging from 12 to 30 and, in the second panel, for D_{F2} values from 7 to 17 at fixed D_{F1}. In both panels $D_N = 40$. Barrier heights and other parameters are as in Fig. 2.3. The difference is obvious: while in the first panel the results barely change (although the change is nonmonotonic), in the second one every relevant quantity (CB, ZBC, high bias and low bias behaviors etc) changes, in obvious and very strongly nonmonotonic ways. Thus, in the fabrication process, the precise thickness of D_{F1} is less critical than that of D_{F2}. As to the normal spacer thickness, in the last two panels of Fig. 2.4 we consider the dependence of G on D_N. We again plot G at fixed $\phi = 0$ for several values of D_N at two values of D_{F2} (see caption). One can see that while quantities such as the CB do not depend very much on D_N, the low and high bias behaviors vary quite appreciably overall, the former rather dramatically. Hence we conclude that D_{F2} is the crucial geometrical parameter in the problem, followed in importance by D_N and with D_{F1} being much less relevant.

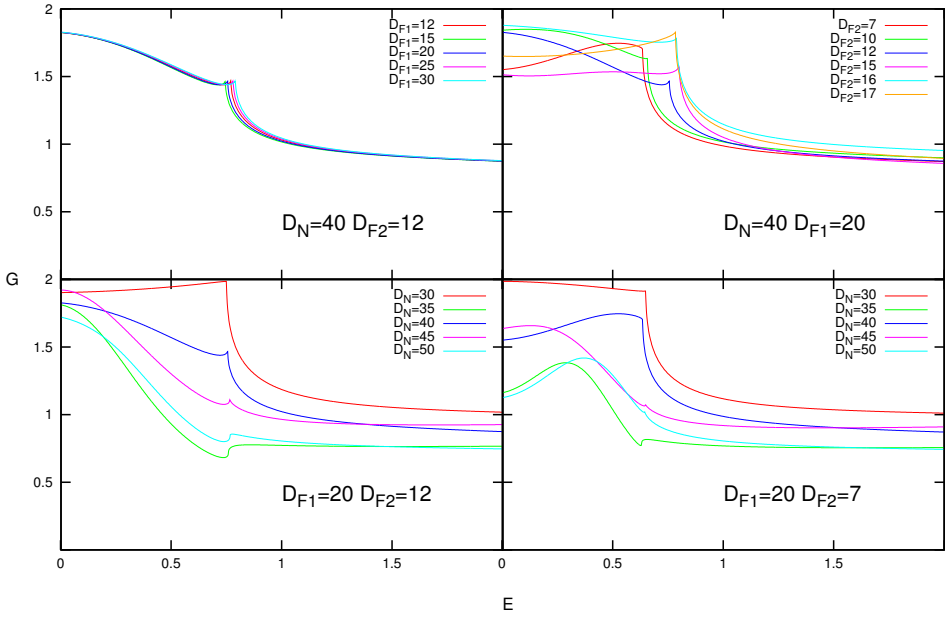

Figure 2.4: Effects of varying D_{F1} or D_N, compared with dependence on D_{F2}. All panels are for $\phi = 0$, barrier values of 0.3, 0.3, and 0.1 and the field parameter, correlation length, and D_S are as in Figure 2.1. The first two panels contrast the effect on the conductance of varying the thickness D_{F1} of the outer ferromagnetic layer with D_{F2} of the inner ferromagnetic layer. In the first panel, D_{F1} is varied, as indicated in the legend, at $D_{F2} = 12$, while in the second one D_{F2} is varied at $D_{F1} = 20$. The last two panels show the effect of varying D_N at $D_{F1} = 12$ and $D_{F2} = 7$ respectively. The dependence of the results on D_{F1} is much weaker than that on D_{F2} or D_N. Both D_{F2} and D_N have a large impact on the ZBC, meanwhile D_{F2} has a much larger effect on the CB.

Careful examination of the above results yields insights on the combined effects of interfacial scattering and on geometry, particularly on D_{F2}: how geometry and interfacial strength are related follows ultimately from the oscillatory nature of the Cooper pairs and from quantum mechanical interference. We now display, in Fig. 2.5, these combined effects in a more direct way. As in Fig. 2.4 we study results for fixed $\phi = 0$. We consider four values of D_{F2}, one in each panel, ranging from 7 to 17, and plot results for several values of H_B at $H_{B3} = 0$. In the first panel we see a large and monotonic dependence on H_B of the entire conductance dependence. In the next case shown,

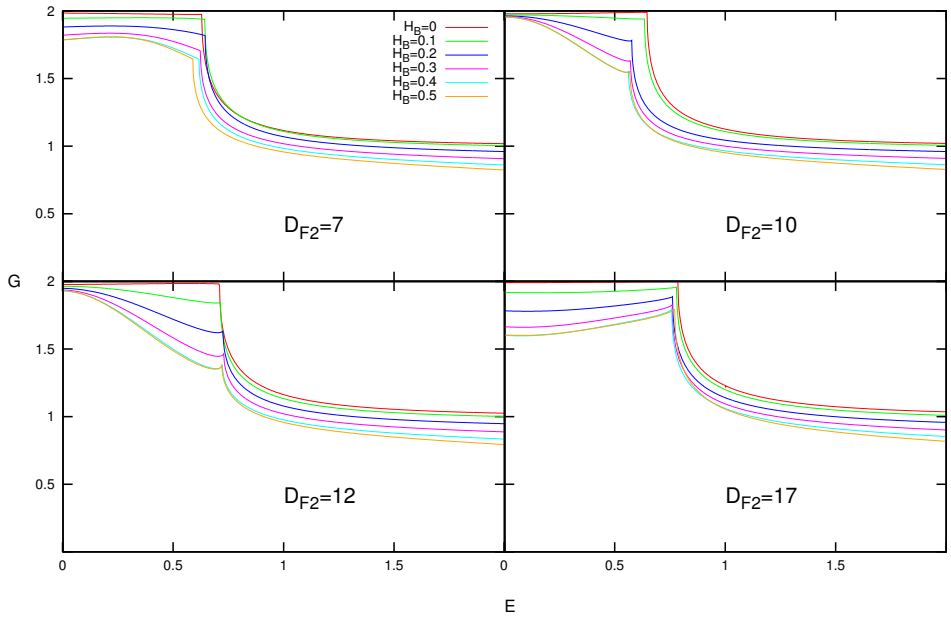

Figure 2.5: Combined effect of D_{F2} and barriers. The behavior at fixed $\phi = 0$ and $H_{B3} = 0$ is studied. Each of the four panels corresponds to a fixed value of D_{F2}: 7, 10, 12, and 17 and the curves correspond to values of $H_{B1} = H_{B2} \equiv H_B$ as indicated in the legend. A nonmonotonic feature in the ZBC is observed as a function of D_{F2}, owing to the oscillatory behavior of the Cooper pairs.

$D_{F2} = 12$, the ZBC depends only very weakly on H_B. In the next panel, the spread in the ZBC with H_B increases somewhat, as compared to the previous panel, and it does so even more in the last panel. This resonance-like behavior is not the same as in the one-dimensional two barrier problems in basic quantum mechanics, where a resonance feature is observed in the transmission coefficients as a function of the distance between the barriers. This analogy might apply better to D_N, but not to the inner ferromagnetic thickness D_{F2}. Instead, this resonance is due to the oscillatory behavior of the Cooper pairs. We see then that certain values of D_{F2} make the system, or at least its ZBC, partly "immune" to the effects of fairly high surface barriers. Although this holds only to a limited extent, it may be worthwhile to attempt to exploit this effect to palliate the existence of unfavorable interfaces with unavoidably large scattering. In Chapter 3 we

further examine this resonance effect and how it relates to the oscillatory Cooper pairs and the spin-dependent conductance.

2.3.3 Temperature dependence

Experiments in these systems are not performed at zero temperature, nor, in practice, at ultralow T. Therefore the influence of T must be examined. There are two transition temperatures to consider: the transition temperature T_{c0} of pure bulk S material, and the transition temperature T_c of the device, which is typically considerably lower. In our discussion we will use a dimensionless temperature T in units of T_{c0} since T_c varies as the geometry is changed.

As explained in Sec. 3.2.3 one has to consider two sources of T dependence. The first is that arising from the self-consistent pair potential, $\Delta(y)$, that is, the T dependence in the effective Hamiltonian. This leads to the function G_0 defined below Eq. (2.13) and in Eq. (2.14) being T dependent. The second is that originating in the Fermi functions in Eq. (2.13). As discussed in connection with Eq. (2.15) the latter is not negligible since the scale of the variation of G with bias is Δ_0, not the Fermi energy. We have found that, in practice, Eq. (2.16), which is not dependent on any expansion, is much more useful than the Sommerfeld method in the relevant temperature range. This is because the conductance has large, and even discontinuous derivatives, which the Sommerfeld expansion does not handle well.

Representative results are shown in Fig. 2.6. In the first two panels we consider a fixed $\phi = 0$ and we show results for G both at $T = 0$ and at a temperature $T = 0.1$. For the size ranges considered in this section we have found that T_c/T_{c0} values are in the 0.5 to 0.6 region, which corresponds to a T/T_c of about 0.2. The first panel shows results in a strong tunneling limit regime with high barriers, and the second for zero barrier heights. Plots of G_0 , i.e. the results obtained by using the $\Delta(y)$ correction only are also included: these are obviously inadequate in both cases, and the full result is needed. We have found this to be invariably the case except at unrealistically low T. The overall effect of the temperature is, otherwise, that of rounding up and softening the sharp features of the low T results. A consequence of this is that at finite T one has to redefine more carefully the CB as the bias value at which G has a peak or a high derivative. The proper redefinition is the bias value at which G varies fastest.

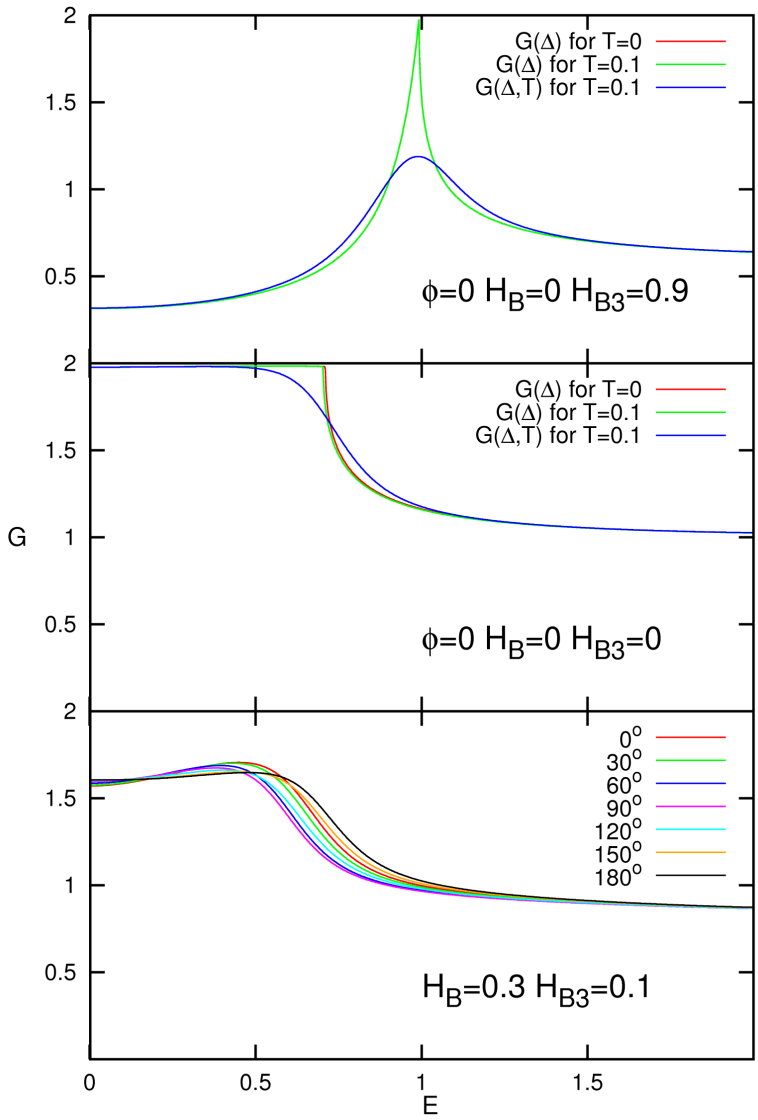

Figure 2.6: Temperature dependence of the conductance. In the first two panels we consider G at fixed ϕ. The thicknesses and fields are as in Fig. 2.1. Temperatures $T = 0.1$, in units of T_{c0}, are compared to $T = 0$ results. The result of including only G_0, the correction to G arising from the T dependence of $\Delta(y)$ is also shown, but is nearly identical to that of G at $T = 0$ particularly in the top panel. The first panel is for a very high barrier ($H_{B3} = 0.9$) between S and F_2 and $H_{B1} = H_{B2} = 0$, while in the second all $H_{Bi} = 0$. The last panel illustrates (for the same values as the first panel in Fig. 2.3), a case where the CB varies very nonmonotonically with angle, and shows how little this behavior is affected by T.

In the third panel of Fig. 2.6, we replot G for the same case considered in the first panel of Fig. 2.3, which, as we have remarked before, shows good spin valve effects in its CB properties, but now at $T = 0.1$ instead of at zero temperature. The two results should be carefully compared. We see that while the curves are now much smoother the behavior of the different features with angle are robust. In particular the sharp minimum of the critical bias at $\phi = 90^\circ$ remains unchanged. We have found this to be the the situation in all the cases we have checked. Hence, spin valve properties on the CB are only weakly dependent on T.

2.3.4 Spin Currents

We present here some results for the spin current and the spin transfer torque. We restrict ourselves in this chapter to the case where there is no spacer, and the barrier parameters are zero, where we include these items in Chapter 4. We consider in this chapter a range of bias voltages and all values of the angle ϕ. Very limited results for only $\phi = 90^\circ$ value were given in Ref. [41]. We use units such that $\mu_B = 1$ and take $h = 0.1$. We consider a superconductor thickness of five times the coherence length ($D_S = 250 = 5\Xi_0$) so that the saturated value of $\Delta(y)$ is essentially the same as the bulk S value Δ_0. We assume a rather thick F_1 layer ($D_{F1} = 250$) while $D_{F_2} = 30$.

The main quantities we will focus on are the three components of the spin currents and of the spin transfer torques (STT) as a function of position. For the charge current, the conservation law entails that the current is independent of position. But for spin, the derivative of the current is the STT (see Eq. 2.19) and the latter quantity is of great physical interest. As usual [31, 41] we normalize $\mathbf{m}$ to $-\mu_B(N_\uparrow + N_\downarrow)$. The normalization for the spin current follows from these conventions. There are two alternative methods to calculate the spin currents: one is directly from the expressions in Eqs. (2.18). The other method is to calculate the torque first, from the expression below Eq. (2.19) and then integrate over the y variable. The two methods agree when the calculations are done self consistently, as was conclusivelly shown in Ref. [41]. The second method is computationally much easier, but it yields results only up to a constant of integration. We have therefore used the direct method: it requires obtaining wavefunction results over a very fine mesh, so that the derivatives in Eq. (2.18) can be calculated to sufficient accuracy.

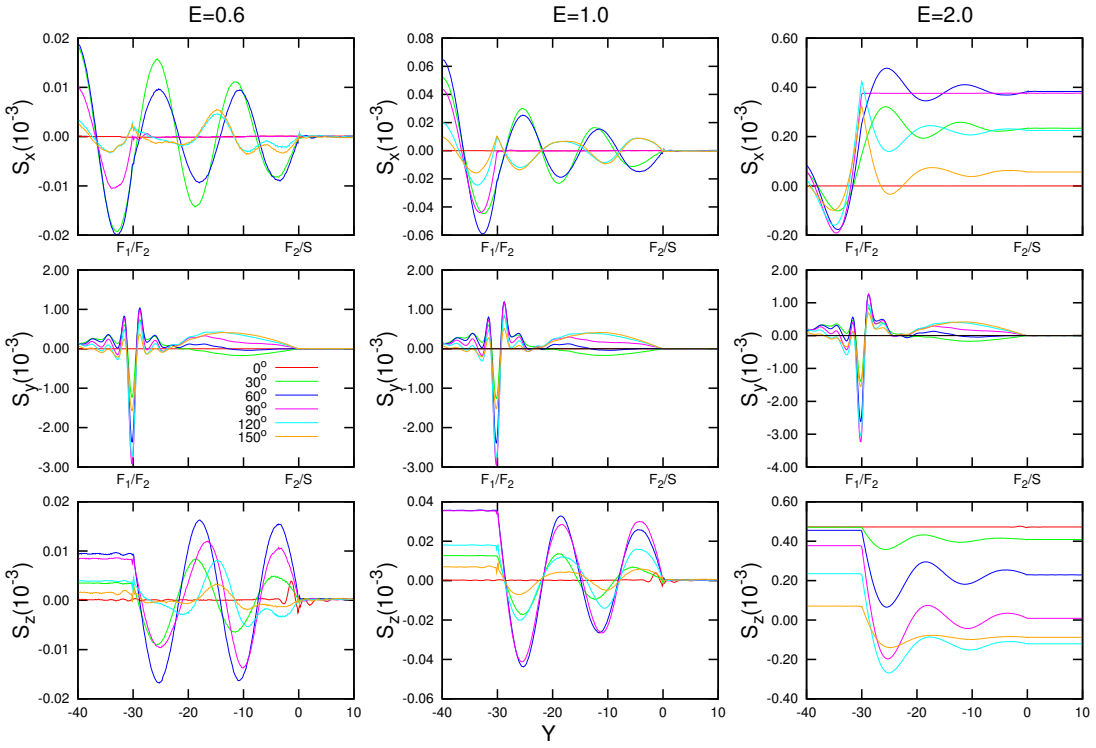

Figure 2.7: The three components of the spin current are shown as a function of Y for several values of ϕ, as indicated, and three values of the bias voltage. We have $h = 0.1$, $D_{F1} = D_S = 250 = 5\Xi_0$, $D_{F2} = 30$, $D_N = 0$. Only the central region of Y is plotted: $Y = 0$ is at the F_2/S interface. All components of the spin current are zero for $\phi = 180°$.

In the following discussion it is important to recall the meaning of the indices and coordinates. The spin current is in general a tensor, each element having two indices, one corresponding to the spatial components and the other to spin. In a quasi-one dimensional geometry, the only spatial component is in the y direction, normal to the layers in our convention (see Fig. 1.3). The spin current is then simply a vector in spin space: the indices in S_i denote spin components, with all transport being in the spatial y direction. Recalling Eq. (2.19) and the definition of the torque $\tau = \mathbf{2m}\times\mathbf{h}$ we see that τ_y tends to twist the magnetization in the plane of the layers, but of course it can only do so in regions near the interfaces, where $\mathbf{m}$ and $\mathbf{h}$ are not parallel due to magnetic proximity effects. We also see that each component of the torque vanishes in the S layer where the internal field parameter h is zero.

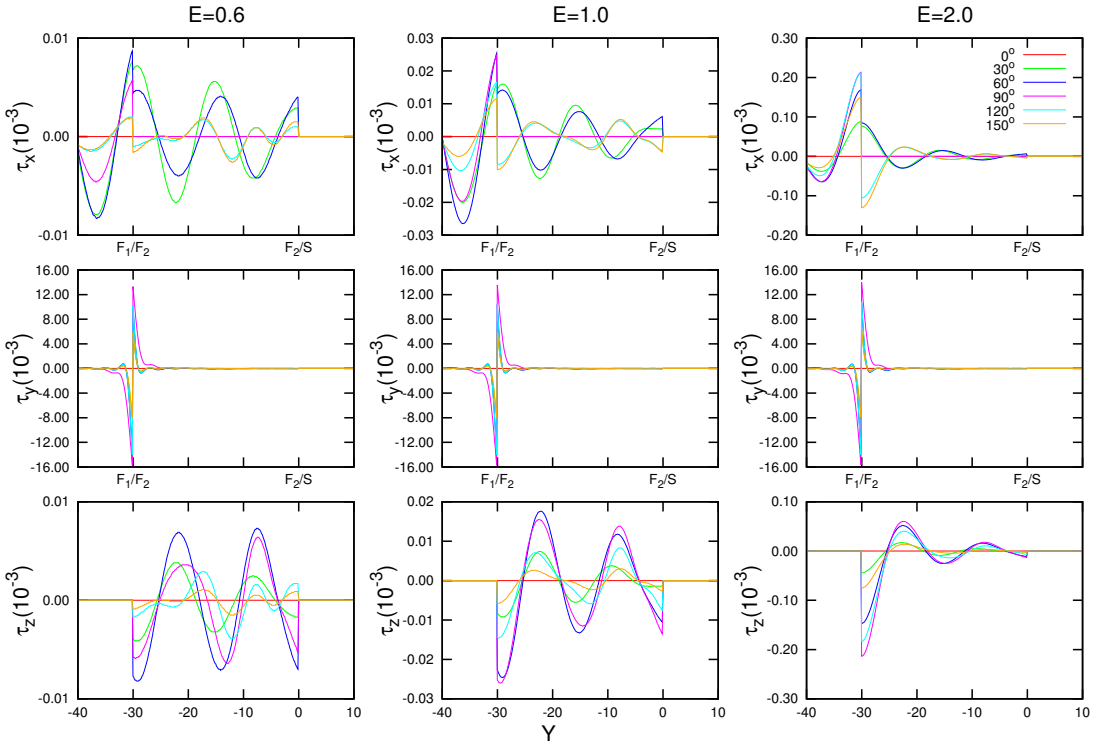

Figure 2.8: The three components of the spin transfer torque plotted for the same situation as in the previous figure. The torque is identically zero for $\phi = 0$ and $\phi = 180°$. The discontinuities at the interface reflect those of the internal fields.

We can now discuss the plots in Figs. 2.7 and 2.8. These two figures show results for the three components of the spin current and of the STT respectively, each under the same conditions (see captions). These quantities are shown for three values of the bias, E, ranging from below to well above Δ_0: for each component, there is a panel corresponding to each value of E. The curves correspond to different values of ϕ as indicated in the legend. At $\phi = 0$ and $\phi = 180°$ the same conservation laws that preclude singlet to triplet pair conversion imply that the torques vanish. It is evident that there is no point in including the regions of the sample deep inside S or even well inside F_1, so the region plotted is that which includes both interfaces: the S/F_2 interface at the origin and that between ferromagnets at $Y = -30$, where Y is the dimensionless position.

The y-components results are easiest to understand: the component of the torque

has very sharp peaks, with opposite signs, near the F_1/F_2 boundary where it vanishes. These peaks reflect the existence of a strong but short-ranged magnetic proximity effect. In F_2 and in F_1, τ_y is small and oscillatory. It reaches its maximum value at $\phi = 90°$. It depends only weakly on the bias, since it basically reflects a static effect: the two magnets interacting with each other. This behavior is of course reflected in S_y as both quantities are related via Eq. (2.19).

The behavior of the in-plane components, x and z, is similar to each other (they are related by spin rotations) and quite different from that of y. Now currents and torques are transport-induced and one sees immediately that they markedly depend on bias. Since in F_1 the internal field always points along z, we find that S_z is a constant in F_1, its value increasing with bias. As a function of ϕ its behavior is complicated, the maximum value is not precisely at $\phi = 90°$ and it is dependent on bias. For this value of ϕ the field points along the x direction in F_2 (it is always along z in F_1). Therefore S_z is always spatially constant in F_1 and this applies also to S_x in F_2 at $\phi = 90°$. For other values of the mismatch angle S_x oscillates in both magnetic layers, and so does S_z in F_2. The amplitude of the oscillations of S_x decays slowly deep into the F_1 layer. In all cases the period of the spatial oscillations is approximately $1/h$ indicating that the oscillations are due to the behavior of the Cooper pairs. As to the corresponding components of the torque, one notes at once that their maximum value is much smaller than that of the τ_y peak but, away from the F_1/F_2 interface, the values are not all that different. This reflects the geometry, as explained above. We see that the x and z components of the torque are also nonmonotonic with ϕ, with peaks that are not necessarily at $\phi = 90°$, depending on the bias. For lower biases, the peak values appear to shift away to smaller values, more closely aligned with the z direction, due to the increasing static effect from the F_1 layer. In our coordinate system, τ_z vanishes in F_1 for all ϕ and oscillates in F_2. Correspondingly, τ_x is oscillatory in both F_1 and F_2 except at $\phi = 90°$ where it is zero in F_2. We have not plotted the magnetization itself, but its components exhibit damped oscillations which reflect the well known [76] precessional behavior of the magnetization around the internal fields. Such precessional behavior is then reflected in the spin current oscillations discussed above.

In our coordinate system, S_z is a constant in the outer layer, F_1. Also, all the components of the spin current are trivially constant in the S layer, since there are

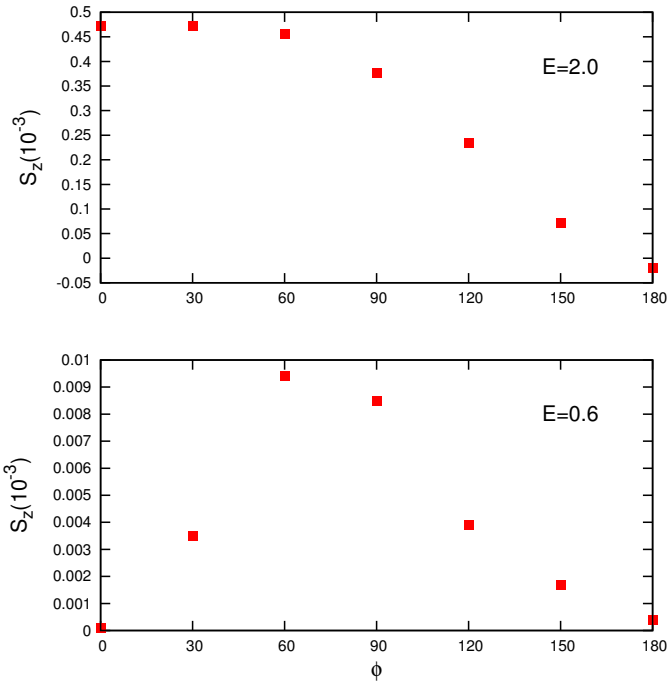

Figure 2.9: The z component of the spin current in the outer F region as a function of ϕ, at two different bias values.

no torques there. As can be seen in Fig. 2.7, all spin current components vanish in S unless the bias exceeds the bulk S gap, Δ_0. This confirms the remarkable fact [41] that, in this respect, spin currents behave like charge currents in an N/S tunnel junction. It can rather easily be shown via standard spin rotation matrix arguments that the constant values of S_z and S_x deep in the S material, in the limit of large bias, should be approximately related to the value of S_z in the F_1 layer by factors of $\cos\phi$ and $\sin\phi$ respectively, and this can be seen in the last column of Fig. 2.7 to hold rather accurately at $E = 2$. On the other hand, the dependence of the constant value of S_z in the outer layer on ϕ is nontrivial as one can see in Fig. 2.7. We display this more clearly in Fig. 2.9, where we plot the value of S_z in F_1 at two different bias values. We see that for values below the CB the behavior is nonmonotonic: it cannot be monotonic, since S_z vanishes at both $\phi = 0$ and $\phi = 180°$. The maximum value is near $\phi = 90°$. On the

other hand, when the bias is well above the CB, S_z, which in this case is non-vanishing at zero angular mismatch, decreases monotonically with ϕ. It becomes slightly negative when the two magnets are aligned in opposite direction. The behavior is not described by a simple trigonometric function and a simple argument leading to the behavior found seems elusive.

2.4 Conclusions

The focus of this chapter is on the prediction of the charge transport properties of superconducting spin valves with a $F_1/N/F_2/S$ layered structure. The emphasis is on studying systems having material and geometrical characteristics corresponding to samples that can be experimentally fabricated. Our main results pertain to the conductance G as a function of bias, particularly with respect to the misalignment magnetization angle ϕ between the F layers: variation of this angle produces the desired spin valve effects. The conductance is the basic information which is experimentally obtained from charge transport measurements: it is the derivative of the current-voltage relation. To further our objective we have used values of the material parameters (such as the internal magnetic field and the superconducting coherence length) which have been previously shown [9] to fit with great accuracy the transition temperatures of such valve structures when the actual materials are Co, Cu and Nb. We have also used thickness values which encompass the available and desirable experimental ranges and have stayed away from idealistic assumptions, such as ideal interfaces, which are essentially irrelevant to actual experimental conditions. We have also studied the often neglected temperature dependence of the results. We have used a fully self consistent approach, which is absolutely necessary to ensure that charge conservation is satisfied.

Our results are summarized in Sect. 2.3. The most important conclusion to be learned from the figures presented is that simple extrapolations are inadequate. There are several interfering oscillatory phenomena involved – the center of mass oscillation of the Cooper pairs in ferromagnets, the transmissions and reflections (ordinary, Andreev, and anomalous Andreev) at the three interfaces, and the usual quantum mechanical effects. As a result, the dependence of the relevant quantities that characterize the conductance (examples are the critical bias, the zero bias conductance, and the low and

high bias features) have nonmonotonic behavior when just about any parameter in the problem varies. From this it follows that the valve effects, that is, the variation of G with ϕ, vary quantitatively and qualitatively depending on parameter values. The lack of monotonicity makes it extremely difficult to predict by extrapolation the measurable features expected for any given set of conditions. The only thing that makes sense is to build a database of conductance plots for different sets of parameter values, and compare the plots in the database with experimental results as they become available. We have built such a database– the results included here are a representative subset.

As far as the geometry dependence we have found that results depend most strongly on the thickness of the inner ferromagnetic layer, with a large dependence on the normal spacer thickness as well and a relatively weaker one on that of the outer F electrode. This is however an overall, general statement: specific details may be different. We study the spatial dependence of the F_2 layer and the resonance phenomenology in greater detail in the Chapter 3. We have also found that the interfacial scattering specifically due to surface imperfections (the barriers) does not severely affect the valve effects for typical experimentally accessible values. Of course, scattering strong enough to destroy the proximity effect would be another matter. Another important conclusion we have reached is that temperature effects are not negligible in typical experimental situations. Furthermore, because of high derivative regions in the G vs. bias curves, a Sommerfeld expansion does not work well. However, an exact calculation can be performed numerically and it reveals that the shape of the conductance curve changes, becoming much smoother as bias varies, where as the valve effects as a function of ϕ remain unaffected.

We have also studied, in a much more limited way, the spin transfer torque and the spin currents in structures lacking the N layer. The results are analyzed in Sec. 2.3.4. We have found, in our geometry, that the y-component of the spin torques have sharp peaks at the F_1/F_2 interface, nearly independent of applied bias. These are due to the strong, static magnetic proximity effects. The greatest peak occurs for a mismatch angle ϕ of 90°. The spin torque components in the x and z direction are bias dependent and more complex, with higher peaks at angles smaller than $\phi = 90°$ for lower biases. We attribute this to static effects from the F_1 layer magnetization. We have calculated the spin currents using the direct method described in Eq. (2.18). We find a nonmonotonic

behavior in the spin current amplitudes similar to that of the spin torque. The oscillation amplitudes tend to peak for angles slightly below $\phi = 90^\circ$ for lower biases. The S_z component is constant in the F_1 layer and monotonic with angle for high bias values (above Δ_0) only. In the S layer, the spin currents are zero except for at high bias when both the S_x and S_z components attain nonzero values for most values of ϕ. The consistency between the torques and spin current gradients, imposed by the conservation laws, is ensured in our approach. In Chapter 4 we extend our study in spin transport to include the N layer and interfacial scattering.

To conclude, the measurable quantities have complex behavior, often nonmonotonic as experimental parameters and inputs vary. Our plots provide an wide spectrum of features to study, many of which are not yet fully understood. We expect that the results we have obtained will provide a very important guide to experimentalists building real world superconducting spin valves in nanoscale heterostructures.

Chapter 3

Spin-split Conductance and the Sub-gap Peak

3.1 Introduction

The work presented in this chapter is based on a previous publication Ref. [68] which has been edited for use in this thesis.

In Chapter 2 we studied the charge transport properties of the superconducting spin valve $F_1/N/F_2/S$ heterostructure with realistic geometrical thicknesses, interfacial scattering due to sample imperfections, and for realistic parameters of the materials. We studied the dependence of the conductance not only on the relative orientation of the ferromagnetic exchange fields, i.e. the valve effect, but also on the sample layer thicknesses and interfacial quality. However, we had only scratched the surface of the rich properties that can be found in these devices. In this chapter, we dive deeper into the thickness dependence of the F_2 layer in order to investigate further the resonance effects found in Chapter 2, in which the conductance at zero bias would be independent of the interfacial scattering quality for certain thicknesses of the intermediate layers. We find below that many of these properties can be described by a spin-dependent conductance which may also give rise to a subgap peak structure in the total conductance. We then investigate this subgap structure and the angular dependence of the valve effect.

The scientific interest in the unusual and useful properties of F/S structures arises from their antagonistic proximity effects. In ferromagnets, the exchange field works to

split apart singlet Cooper pairs, favoring same-spin triplet states ($m_z = \pm 1$). This leads to an F/S proximity effect that differs drastically from that at N/S interfaces. These proximity effects are very short ranged, and are oscillatory in position [26, 27] due to the Cooper pairs acquiring a center of mass momentum [25]. thickness dependence of thermodynamic properties of F/S layered structures [22], including in ferromagnetic Josephson junctions [77, 78], and transport properties in superconducting spin valve devices [67, 79, 80]. Under certain conditions, it is possible for these structures to feature long range proximity effects. For heterostructures with two or more non-collinear ferromagnetic exchange fields [29, 31, 32, 81] such as the $F_1/N/F_2/S$ case we study, triplet pair correlations with both $m_z = 0$ and $m_z = \pm 1$ can be induced by the ferromagnetic layers' exchange fields. A non-collinear exchange field is necessary to induce $m_z = \pm 1$ states, because otherwise S_z commutes with the Hamiltonian and only the $m_z = 0$ triplet state can be induced. Due to the spatial symmetry of the s-wave Cooper pairs, these triplet correlations in the ferromagnet are odd in time [31] or, equivalently, in frequency [33]. These $m_z = \pm 1$ correlations are long ranged since they are not broken apart by the exchange field [23, 37, 38, 39, 41]. This yields a unique spin-valve effect in $F_1/N/F_2/S$ structures where the triplet correlations, induced by a non-collinear magnetization angle between the ferromagnets, can lead to a non-monotonic angular dependence on the transport features as we discussed in Chapter 2, as well as on the static physical properties such as the transition temperature [9]. This angular dependence motivates much of our study into superconducting spin-valve structures. By considering the spin-dependent charge transport in F/S structures, we can gain further insight into this angular dependence of the superconducting spin valve $F_1/N/F_2/S$. We are also interested in how it compares to the angularly independent $N/F/S$ system.

A charge current carries electrons and holes in both the spin-up and spin-down states, which add up to produce the total conductance of the circuit. When a device is spin polarized, we can see unusual changes to the conductance features arising from the difference in the spin channel transport, leading to each spin band having its own associated conductance that differs from that of the opposite spin channel [82, 83]. The separate spin channel conductances can have features which diverge from those of the total conductance, which is why we collectively refer to the spin-polarized components of the conductance as the spin-split conductance. In a superconducting/ferromagnetic

heterostructure, the interplay between each spin channel in the ferromagnet with the energy gap of the superconductor can lead to dramatic effects in the overall conductance. At low bias, this interplay is mediated by Andreev reflections [49] in which an incoming electron is reflected as a hole and forms a Cooper pair in the superconductor. There are two types of Andreev reflection: ordinary Andreev reflection in which the electron/hole has opposite spin upon reflection, and anomalous Andreev reflection in which they have the same spin. It has been shown [41, 52, 53, 54, 55] that for F/S interfaces, triplet proximity effects are correlated with anomalous Andreev reflection. Therefore, it is pertinent to consider these reflections when determining the spin-split conductance for $N/F/S$ and $F_1/N/F_2/S$ systems.

In Chapter 2, we have noted that the conductance G versus bias voltage V curves in $F_1/N/F_2/S$ structures can exhibit a "subgap" peak structure below the critical bias. We explain in this chapter that in general the low bias structure of G in these devices is due to spin split conductance behavior, and we study in some detail the features involved and what parameters influence them. Specifically, we calculate the spin-split conductance of $N/F/S$ and $F_1/N/F_2/S$ heterostructures and verify that the spin dependence of the conductance can lead to exotic behavior and unusual properties, e.g. in the layer thickness dependence in such structures [67]. By studying the spin-split conductance, we can gain a deeper understanding of the full conductance features studied thus far. We begin with a simple analytic model of an $N/F/S$ structure with infinitely thick N and S layers and examine the thickness dependence of the ferromagnet for the spin-split conductance in an approximate non-self consistent approach. We then compare this model to a fully self-consistent numerical calculation for a finite nanoscale system. We then include a second ferromagnet to determine how the spin-split conductance can lead to the angular dependence in the total conductance. The numerical calculations are done by finding the self-consistent solution of the Bogoliubov de Gennes (BdG) equations [15], which determine the pair potential of the superconductor, with the proximity effects fully being taken into account. We then use a transfer matrix procedure within the Blonder-Tinkham-Klapwijk (BTK) method [50] to extract the conductance.

We use layer thickness values relevant [9] to recent experimental studies of these devices. The exchange field of the ferromagnet and the coherence length of the superconductor are taken at values that correspond to the actual materials (such as Co

and Nb) used so that our work can be more easily compared with experimental results. We perform our calculations in the low T limit in order to best identify the spin-split conductance features that can be seen. We work within the clean limit, but we assume that there is interfacial scattering that can be phenomenologically described via delta function scattering potentials, located at each interface. We use realistic [9] interfacial scattering strengths, as pertinent to good but imperfect experimental samples. We find that moderate interfacial scattering actually enhances the spin-valve effects in some cases, as we discuss in our analysis and conclusions below. The static properties of these samples [9] are accurately described by our clean limit theory when the delta function interfacial potential is included. Although, initially, fabricable multilayered nanostructures were in the dirty limit [6, 84, 85], and the proximity effects in that limit are well established for both N/S heterostructures [85] and $N/F/S$ multilayers [86], recent improvements in the fabrication of nanoscale devices have permitted experimental studies of the superconducting proximity effect on samples that are in the crossover regime [87] and later, on samples in the clean limit [9].

After having established the qualitative properties of spin-split conductance via these analytical and numerical methods, we then calculate the angular dependence of the conductance in the $F_1/N/F_2/S$ superconducting spin valve and establish how it is deeply related to the spin-split conductance. We also discuss how the interfacial scattering, which is an inevitable consequence of imperfect interfaces in fabricable devices, affect the spin-split features and the subgap peak conductance in these systems. From this study, we see a dramatic shift in the conductance for biases below the critical bias (CB) value, determined by the pair potential of the superconductor. This shift within the subgap is oscillatory with the thickness of the F_2 layer, and it results in a conductance peak that occurs between the critical bias and zero bias. We find that this subgap peak in conductance can have a large angular dependence, producing a significant valve-effect. We hope that our work will lead to a better understanding of these devices for future application and motivate additional theoretical and experimental work.

3.2 Methods

The geometry of the $F/N/F/S$ system is depicted in Fig. 1.3. The layers are assumed to be infinite in the x-z plane with finite widths in the in-plane y direction in which the current will flow. The magnetizations of the two ferromagnetic layers are misaligned by an angle ϕ in the x-z plane. Since the methods we use here are those of Chapter 2, we do not repeat them in their entirety. We instead refer the reader to Secs. 1.4 and 2.2 where we discuss our calculation of the equilibrium quantities, in particular the self-consistent pair potential. This calculation involves a Bogoliubov transformation of the full Hamiltonian Eq. (1.19) which includes the pair potential Δ and the Stoner field $\mathbf{h}$. In our quasi-one dimensional geometry, the Hamiltonian can thus be expressed by Eq. (1.22), which is described in Secs. 1.4 and 2.2. The calculation of the pair potential $\Delta(y)$ must [41, 62, 63, 64, 67] be performed self consistently, in order to ensure that charge conservation [73] is preserved, as we have shown in Sec. 2.2.3. In this chapter, we also consider a simpler, one dimensional $N/F/S$ structure which can be solved analytically if one makes the additional approximation of treating the pair potential non-self-consistently, with a constant value of $\Delta(y)$ in S. This system can be visualized by removing the left-most F_1 layer in Fig. 1.3 and letting the N and S layer be infinite in thickness. The analytic calculation is an approximation, done only as a means of comparison and of obtaining, as we shall see, some physical insights. A correct calculation requires a self-consistent approach. In Sec. 3.2.1 we review the calculation of the transport quantities (e.g. the conductance) and how the transfer matrix method applies to the analytic calculation.

3.2.1 Transport

We use the BTK formalism [50] in the same way as we did in Chapter 2. We briefly review the main equations here to re-establish our notation.

The incoming waves in terms of these amplitudes are compactly written in the form

$$\Psi_{F1,\uparrow} \equiv \begin{pmatrix} e^{ik^+_{\uparrow 1}y} + b_{\uparrow,\uparrow}e^{-ik^+_{\uparrow 1}y} \\ b_{\downarrow,\uparrow}e^{-ik^+_{\downarrow 1}y} \\ a_{\uparrow,\uparrow}e^{ik^-_{\uparrow 1}y} \\ a_{\downarrow\uparrow}e^{ik^-_{\downarrow 1}y} \end{pmatrix} \tag{3.1}$$

for an incoming up spin particle in F_1, while for the down spin case one has:

$$\Psi_{F1,\downarrow} \equiv \begin{pmatrix} b_{\uparrow,\downarrow}e^{-ik^+_{\uparrow 1}y} \\ e^{ik^+_{\downarrow 1}y} + b_{\downarrow,\downarrow}e^{-ik^+_{\downarrow 1}y} \\ a_{\uparrow,\downarrow}e^{ik^-_{\uparrow 1}y} \\ a_{\downarrow,\downarrow}e^{ik^-_{\downarrow 1}y} \end{pmatrix} \tag{3.2}$$

where $a_{\sigma,\sigma'}$ are the Andreev reflection amplitudes and $b_{\sigma,\sigma'}$ are the ordinary reflection amplitudes. The second spin index in the amplitudes denotes the spin of the incoming particle, and the first that of the reflected wave. The wavevectors are:

$$k^{\pm}_{\sigma 1} = \left[(1 - \eta_\sigma h_1) \pm \epsilon - k^2_\perp\right]^{1/2}, \tag{3.3}$$

with $\eta_\sigma \equiv 1(-1)$ for up (down) spins. $k_\perp$ is the length of the wavevector corresponding to energy $\epsilon_\perp$. Here and below all wavevectors are in units of k_{FS} and all energies in terms of E_{FS}.

The method to calculate these amplitudes has been discussed in Chapter 2 and in previous work [41] for the $F_1/N/F_2/S$ system with a self-consistent pair potential and it would be superfluous to repeat the discussion here.

3.2.2 Approximate analytic methods

If one foregoes treating the pair potential self-consistently, it is possible to derive expressions for the relevant amplitudes which are in principle analytic, although rather intricate. We do this here for an infinite $N/F/S$ heterostructure, where N and S are assumed to be of infinite thickness, but F is finite. The expressions for the incident waves, now impinging from N, are of the form given in Eqs. (3.1) and (3.2) but with a

simplified wavevector structure involving only the spin independent wavevectors

$$k_N^{\pm} = [1 \pm \epsilon]^{1/2} \tag{3.4}$$

We can apply the continuity condition to write the transfer matrix as was done in Sec. 2.2.2, except now we only need a single S layer for the constant pair potential assumption and we have eliminated the F_1 layer. Thus we may apply the continuity condition at each interface $\Psi_N(0) = \Psi_F(0)$, $\Psi_F(d_F) = \Psi_S(d_F)$, where for the infinite system, we conveniently choose the N/F interface to be at $y = 0$ and the F/S interface to be at $y = d_F$. The wavefunction Ψ_F can be given by Eq. (2.6) for $\phi = 0$ and Ψ_S by Eq. (2.9) with the $\bar{t}_n$ amplitudes set to zero. The conditions on their derivatives are $\partial\Psi_N(0)/\partial y = \partial\Psi_F(0)/\partial y + 2H_B\Psi_F(0)$ and similarly for the second interface. We can use a transfer matrix method to write these as 8×8 matrices $\mathcal{M}_i$ multiplied by their respective vector of unknown coefficients x_i for each layer i. Then, $\mathcal{M}_N x_{N,\sigma} + c_{N,\sigma} = \mathcal{M}_{F,\ell} x_F$ and $\mathcal{M}_{F,r} x_F = \mathcal{M}_S x_S$, where (ℓ, r) denote that the wavefunctions are evaluated on the left or right side of the layer respectively and σ denotes the spin of the incoming electron in the N layer. $c_{N,\sigma}$ represents the incoming spin σ particle term in Ψ_N. By solving and eliminating the intermediate layer coefficients, we find the eight total coefficients of both the N and S layer:

$$x_{N,\sigma} = \mathcal{M}_N^{-1}\mathcal{M}_{F,\ell}\mathcal{M}_{F,r}^{-1}\mathcal{M}_S x_S - \mathcal{M}_N^{-1} c_{N,\sigma}. \tag{3.5}$$

Solving these eight equations simultaneously for both spin-up and spin-down incoming electrons, we find the two sets of four reflection amplitudes $b_{\sigma,\sigma'}$ and $a_{\sigma,\sigma'}$, one set for each incoming spin state σ', which we use to calculate the conductance in Sec. 3.2.3.

Thus, the calculation is formally analytic. Although the full form solution for each reflection amplitude can not be written in a compact manner, knowing the form of the plane wave description lets us approximately determine the spatial dependence of the amplitudes. This spatial dependence comes from a combination of plane waves in F, which are of the form $e^{ik_\sigma^{\pm} d_F}$, in which the wavevectors in the F layer are defined by Eq. (3.3). In the zero bias limit, $\epsilon \to 0$, we can express the wavevector for the forward conductance ($k_\perp = 0$) as $k_\sigma = \sqrt{1 \pm h}$ in our units, where we have dropped the particle/hole notation as these quantities are the same at zero bias. Thus if we

write one such combination of plane waves, e.g. $e^{i(k_\uparrow - k_\downarrow)} \approx e^{-ihd_F}$ to lowest order in h, we expect then to see a spatial periodicity with a wavelength d such as $k_{FS}d = 2\pi E_{FS}/h$ (in dimensionless units $d = 2\pi/h$) at zero bias. These are the same as the well known oscillations of the Cooper pair amplitudes within the ferromagnet [25]. Similarly, $e^{i(k_\uparrow + k_\downarrow)} \approx e^{-ik_F d_F}$ means we can also expect oscillations of wavelength $d = 2\pi/k_{FS}$ or, in dimensionless units, simply 2π. In subsection 3.2.3, we will use the absolute value squared of these amplitudes to calculate the conductance. Therefore, we expect all real coefficients with a $2\pi/h$ or 2π periodicity in the amplitude to result in a conductance with periodicities proportional to π/h and π respectively.

3.2.3 Extraction of the spin split conductance

From the above results one can extract the conductance using the BTK method [50]. The current is related to the applied bias V via the expression:

$$I(V) = \int G(\epsilon) \left[f\left(\epsilon - eV\right) - f\left(\epsilon\right) \right] d\epsilon, \tag{3.6}$$

where f is the Fermi function. The bias dependent tunneling conductance is $G(V) = \partial I/\partial V$ which we evaluate in the low-T limit. The conductance can be calculated using the reflection amplitudes a and b described in the above subsections, for either the self-consistent or non-self-consistent results. Combining the conductance contribution from incoming spin-up and spin-down electrons one has:

$$\begin{aligned} G(\epsilon) &= \sum_\sigma P_\sigma G_\sigma(\epsilon) \\ &= \sum_\sigma P_\sigma \left(1 + \frac{k^-_{\uparrow 1}}{k^+_{\sigma 1}} |a_{\uparrow,\sigma}|^2 + \frac{k^-_{\downarrow 1}}{k^+_{\sigma 1}} |a_{\downarrow,\sigma}|^2 - \frac{k^+_{\uparrow 1}}{k^+_{\sigma 1}} |b_{\uparrow,\sigma}|^2 - \frac{k^+_{\downarrow 1}}{k^+_{\sigma 1}} |b_{\downarrow,\sigma}|^2 \right), \end{aligned} \tag{3.7}$$

where G is given in natural units of conductance ($2\pi e^2/\hbar$), and σ denotes the spin of the incoming electron. In Eq. (3.7), $k^\pm_{\sigma 1}$ denotes the wavevector of the respective particle/hole in the first layer. In the $N/F/S$ case described in Sec. 3.2.2, $k^\pm_{\sigma 1} = k^\pm_N$ for both spins, while in the $F_1/N/F_2/S$ case $k^\pm_{\sigma 1}$ is given by Eq. (3.3). The factors $P_\sigma \equiv (1 - h_1 \eta_\sigma)/2$ are included to take into account the different density of incoming

spin up and spin down states in the F_1 layer for the $F_1/N/F_2/S$ system. In the $N/F/S$ system, $P_\sigma = 1/2$ denoting equal density. The quantities G_σ are the spin-up and spin-down conductances, which we collectively refer to as the spin-split conductance, since each component may drastically differ and "split" in behavior from that of the total conductance G. The energy dependence of $G(\epsilon)$ arises from the applied bias voltage V. It is customary and convenient to measure this bias in terms of the dimensionless quantity $E \equiv eV/\Delta_0$ where Δ_0 is the value of the order parameter in bulk S material. We will refer to the dimensionless bias dependent conductance simply as $G(E)$. We will refer to the spin-split conductance G_σ in a similar fashion. In the $F_1/N/F_2/S$ spin valve structure, G and G_σ also depend on ϕ.

Generally, $G_\uparrow$ and $G_\downarrow$ will differ significantly, however they are related to each other by a rotation around the y axis in spin space. Using the unitary transformation [81] $U = e^{-\frac{i}{2}\theta\sigma_y}$ and taking the expectation value, we can define our spin-up and spin-down conductances, $G_\sigma(\theta)$, in a basis rotated from that of the z axis, $G_\sigma(0)$, as:

$$G_\uparrow(\theta) = \cos^2(\theta/2)G_\uparrow(0) + \sin^2(\theta/2)G_\downarrow(0) \tag{3.8a}$$

$$G_\downarrow(\theta) = \sin^2(\theta/2)G_\uparrow(0) + \cos^2(\theta/2)G_\downarrow(0) \tag{3.8b}$$

In the $N/F/S$ system the angle θ can be thought of as the angle ϕ between the field in F and the z axis, since this basis rotation is exactly the same as a rotation in F. However, this is not the case in the $F_1/N/F_2/S$ system when there is an actual angular mismatch and a broken symmetry. We can thus compare the change in the spin split conductance due to the angular mismatch to that arising from a pure rotation in basis.

3.3 Results

In this section we present our results for the spin-split conductance defined by Eq. (3.7) and as explained in the text below it. We focus on the forward conductance, which is suitable for samples with point contacts. We start (Sec. 3.3.1), by analyzing a simple, $N/F/S$ system, with infinitely thick S and N layers, in a non-self-consistent manner, as derived in Sec. 3.2.2. In that case the calculations can be performed analytically, and the results, although quantitatively inaccurate, illuminate a qualitative discussion that

applies to all F/S systems. We then move to the self-consistent approach (Sec. 3.3.2) first briefly for a finite size $N/F/S$ system, so that we can gauge the degree of reliability of the analytic calculations, and then, in subsection 3.3.3, we consider the realistic superconducting spin valve $F_1/N/F_2/S$ system. For reasons that will become clear below, we are particularly interested in how the conductance depends on the intermediate ferromagnetic layer thickness and on the interfacial scattering barriers, particularly that at the N/F interface.

In presenting our results we use dimensionless units: all lengths are in units of k_{FS} and are denoted by capital letters such as D_N, D_F, and D_S. The bias voltage E is in units of the bulk value of the pair potential, Δ_0. The conductance is in natural units $2\pi e/\hbar$. Values of the dimensionless barrier parameters H_B (introduced in Sec. 2.2) greater than unity would begin to approach the tunneling limit, while zero represents a perfect interface. We also set any wavevector mismatch parameters Λ to unity (such that $E_{FS} = E_{FN} = E_{FM}$, see Sec. 1.4), subsuming their effects in the phenomenological H_B values. This reduces the number of parameters governing the system. With a minor exception for illustrative purposes, we set the exchange field in all ferromagnets (which we assume to be of the same material in the valve case) to be $h = 0.145$ in our dimensionless units, where $h = 1$ is the half-metallic limit, and we set the coherence length $\Xi_0 = 115$ in our dimensionless units. The values of h and Ξ_0 chosen have been found to be suitable to the quantitative analysis of static quantities done on similar systems using cobalt and niobium [9].

We have found that the most crucial geometrical parameter for our purposes is the thickness of the intermediate F layer and consequently we examine, in each subsection, the conductance dependence on this layer thickness D_F, or D_{F2}, for the $N/F/S$ or the $F_1/N/F_2/S$ spin valve system respectively. We also examine the dependence on the barrier H_B at the N/F or N/F_2 interface, and also, in Sec. 3.3.3, on the barrier strengths at all the interfaces. In Sec. 3.3.3, we also examine the dependence of the spin-split and total conductances on the mismatch angle ϕ of the exchange fields $\mathbf{h_1}$ and $\mathbf{h_2}$.

3.3.1 N/F/S conductance: analytic results

In this subsection we discuss the results of our analytic approach described in section 3.2.2. To obtain analytic results, we have to abandon self consistency, so the results are only approximate. We consider an infinite $N/F/S$ system, with finite, varying D_F thickness but infinite D_N and D_S. This is worthwhile, however, as from analytic results one can establish context and gain a degree of physical insight that it difficult to gather from our self-consistent numerical results discussed in the subsections below. The non-self-consistent results differ, of course, from the correct self-consistent ones. One obvious difference occurs near the critical bias (CB). For our analytic results the CB is always at $E = 1$ since in the non-self-consistent case, $\Delta(Y) \equiv \Delta_0$ for all Y in S. In Figs. 3.1 and 3.2 we examine the spin-split conductance G_σ (i.e. the spin-up and spin-down components) and the total conductance, G, defined by Eq. 3.7), as functions of applied bias. In Figs. 3.3 and 3.4 we plot the zero bias conductance (ZBC) and the critical bias conductance (CBC) respectively as functions of the thickness of the ferromagnetic layer D_F.

The results plotted in Fig. 3.1 are for a moderately strong barrier, $H_B = 0.5$, which is a realistic value for a good interface, located at the N/F boundary. The reason for studying this barrier is that even a small amount of interfacial scattering allows for the formation of a prominent feature that we wish to study: the subgap conductance peak. This is a peak in the conductance occurring for specific thicknesses of F at biases between zero and the critical bias (the "subgap" bias region). As we shall see, the spin-split conductance components can vary dramatically especially near the CB. The total conductance is a combination of the components of the spin-split conductance. In this single F layer system, the total G is simply the average of the up and down spin-band contributions. When the spin-up and spin-down conductances are split from one another, we see a peak in the total conductance where the two differ the most. Examining the peak value of the conductance, we find a periodic behavior with D_F, with a periodicity of $\pi/h \approx 22$ in our dimensionless units. This can be traced, of course, to the well-known periodicity [25] of the Cooper pair amplitudes, reflected in the above given value, as has been discussed at the end of Sec. 3.2.2.

The figure includes four panels, each for a different value of D_F within one cycle of this periodic behavior. In the first and third panels, which correspond to a D_F

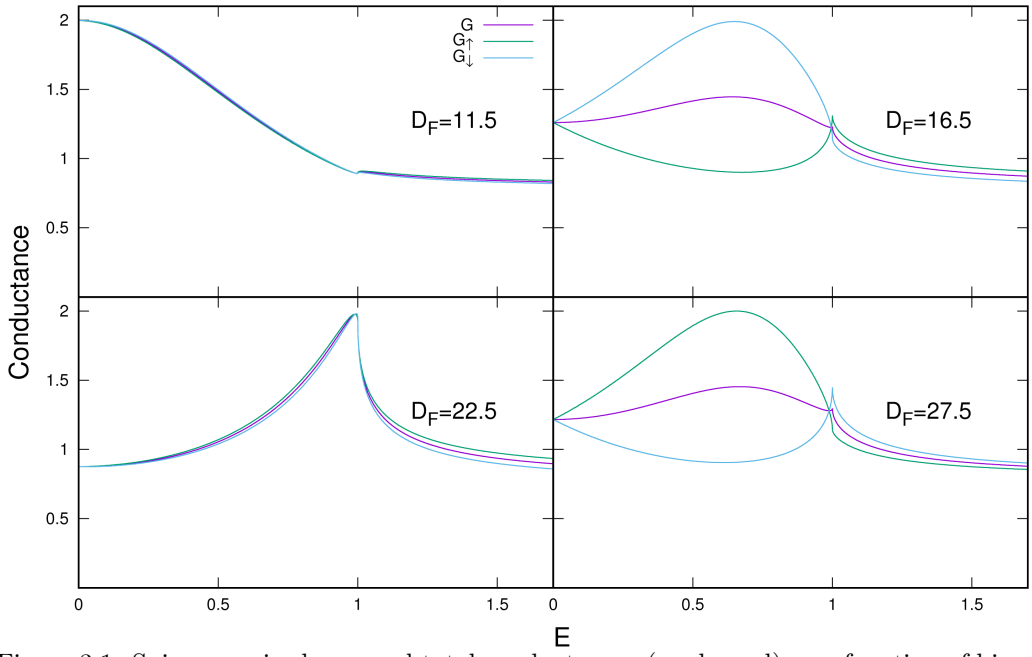

Figure 3.1: Spin-up, spin-down, and total conductances (see legend) as a function of bias (E) in the infinite $N/F/S$ system. Conductances are calculated using a non-self-consistent method. A single barrier with $H_B = 0.5$ is at the N/F interface. The four panels are for different values of the F layer thickness, labeled D_F, which are chosen at intervals of a quarter period ($\pi/2$ phase) of the spatial dependence.

difference of about half a period, we see that the peak in the total conductance occurs at zero bias and at the critical bias respectively, while in the similarly separated second and fourth panels we see a subgap bias conductance peak. This subgap peak in the conductivity is similar to those reported in Ref. [79] for inhomogeneous S/F structures, In their tunneling conductance measurements, they find symmetrical, small peaks in the subgap region of the density of states, which they call the "double-peak spectra" and, for a subset of their samples, a single peak in the zero bias conductance, which they call the "zero peak spectra". Here, we will refer to these peaks as the subgap bias and the ZBC peaks respectively. We believe these observed tunneling conductance peaks may be due to the spin-split conductance phenomenon we discuss below, with the "zero peak spectra" found for a small subset of their samples possibly being due to small fluctuations in the sample layer thicknesses, at fractions of a nanometer.

The total conductance peak moves away from zero bias in the first panel to a finite

subgap bias value in the second. Increasing D_F further, the peak moves to the critical bias in panel three, then returns in panel four to the same subgap bias value as in panel two. It goes back to zero bias, with a peak feature very similar to that in panel one for $D_F = 33$ (not shown): at that point a whole period in D_F has elapsed. In the first and third panels we see little difference between the subgap spin-up and spin-down conductances. On the other hand, we see a very large difference in the spin-split conductance for the second and fourth panels. In the second panel, the spin-down conductance has a large subgap peak, with G reaching a value of $G = 2$ before decreasing towards the CB, where there is a discontinuous change in slope (leading to what we describe as a "shoulder"). The spin-up conductance has the opposite behavior, with a dip in the subgap region that increases to a sharp cusp shaped peak at the CB. This spin-split conductance then yields a total G with a local maximum at the spin-down conductance's maximum, which is also the spin-up conductance's minimum. In panel four, we see a very similar situation. However, the respective behaviors of the spin-up and spin-down conductances have reversed, with the spin-up conductance having an intermediate maximum and a shoulder critical bias feature, and the spin-down conductance having an intermediate minimum and cusp critical bias feature. In both of these panels, the CBC is also split between spin-up and spin-down, and the total conductance has a hybrid cusp-like behavior. There is then a crossover value, where each component (and the total conductance) meet, at a bias slightly below that of the CB.

In all four panels the ZBC is the same for the spin-up and spin-down conductances, and consequentially for the total G. In ordinary Andreev reflection, a spin-up electron reflects into a spin-down hole, and vice versa. In the zero bias limit the electron and hole have equal energy. Thus, in the single F layer case, the zero bias spin-up transmission amplitudes are the same as those for spin-down transmission, due to the symmetry of the electron/hole traveling in the spin-up/spin-down bands. We will see in Sec. 3.3.3 that this is not the case when there is a second ferromagnetic layer.

In Fig. 3.2 we repeat the plots in Fig. 3.1 but for a stronger barrier, $H_B = 0.9$. In all four panels we see in general a decrease in the conductance at all biases, with the remarkable and interesting exception of the peak value of the conductance, which remains high in all cases. In panel one, for example, we see no decrease in the ZBC, and

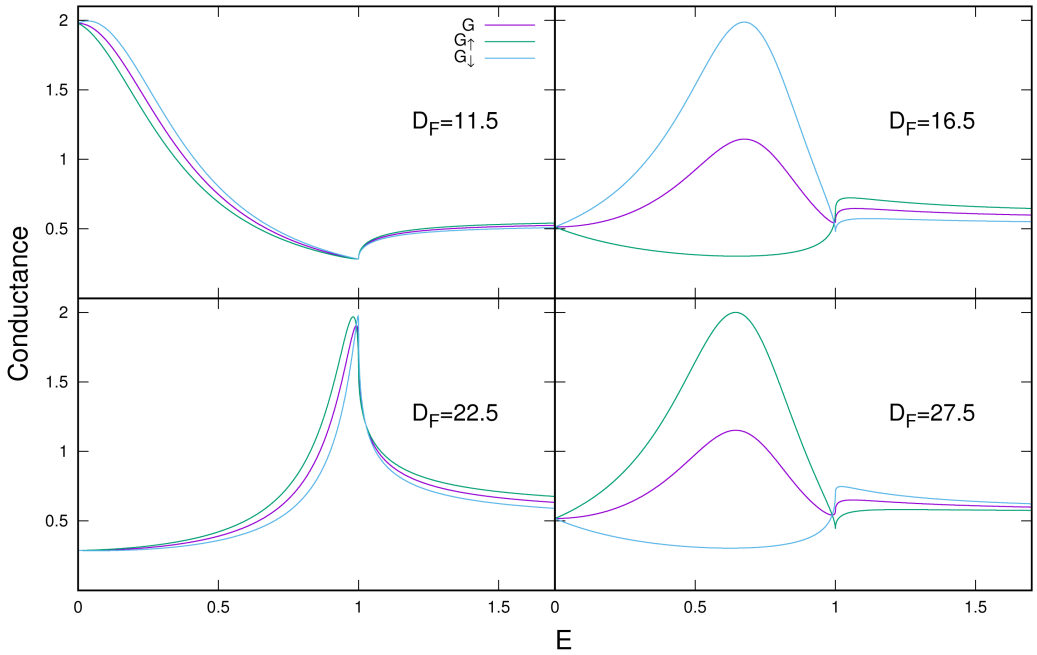

Figure 3.2: Spin-up, spin-down, and total conductance as a function of bias (E) in the infinite $N/F/S$ system. Conductance is calculated as in Fig. 3.1. A barrier with $H_B = 0.9$, significantly larger than that in Fig. 3.1 is at the N/F interface. The four panels are arranged as in the previous figure.

similarly in panel three for the CBC. This leads to a "resonance" feature similar to that discussed in Fig. 2.5 of Chapter 2, where the ZBC is independent on the barrier strength. In panels two and four, we do see a moderate decrease in the average value of the total subgap conductance, but not in the maximum values of the spin-split conductance. Instead, there is a decrease in the minimum of the opposite spin component, as well as a general decrease in the ZBC and CBC. This leads to a much more pronounced subgap peak conductance than in the $H_B = 0.5$ case. This feature is very resilient to high values of H_B, it begins to deteriorate only well into the tunneling limit. A low value for H_B makes the peak less obvious as the subgap conductance increases towards its maximum possible value of $G = 2$ and the difference between the spin-up and spin-down conductances decreases. We have restricted our analysis of this simplified model to the case of only one barrier at the F/N interface. Below, in Sec. 3.3.3, we examine an $F/N/F/S$ system with barriers at each interface including F/S.

We now show specific details of the D_F periodicity. In Fig. 3.3 we plot the zero

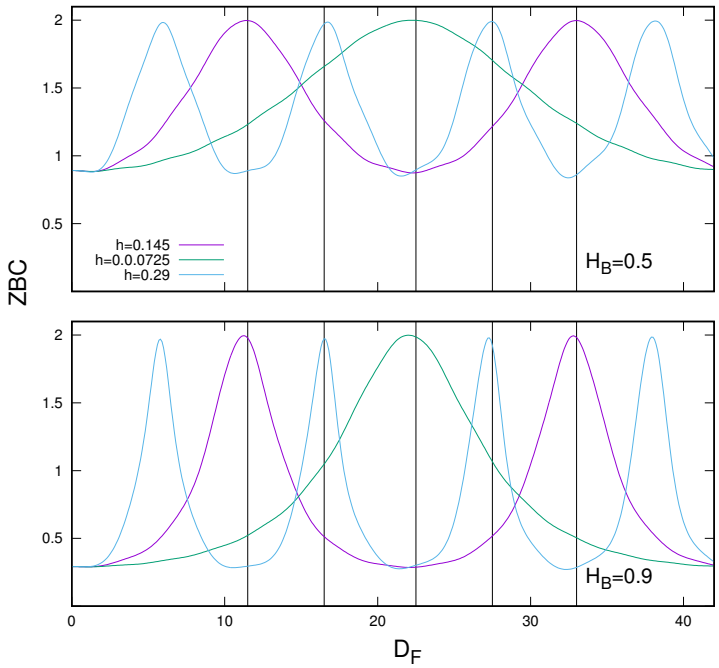

Figure 3.3: The zero bias conductance (ZBC) for an infinite $N/F/S$ system, as a function of D_F, for values of the exchange field half of, equal to, and double $h = 0.145$. The top and bottom panels have barrier strengths of $H_B = 0.5$ and $H_B = 0.9$ respectively, at the N/F interface. We plot the D_F dependence for approximately two oscillation periods at $h = 0.145$. We see a wavelength of π/h for all values of h.

bias conductance as a function of D_F for $H_B = 0.5$ (top panel) and $H_B = 0.9$ (bottom panel), for $h = 0.145$ (the only value we use in all of our figures except this one) and for $h = 0.0725$ and $h = 0.29$, half and double the original value. We do so to best demonstrate the dependence of the periodicity on h. As mentioned above, the ZBC is equal for the spin-up, spin-down, and total conductances and therefore we only plot the total G. The four leftmost vertical lines in each plot are the values of D_F used in Figs. 3.1 and 3.2, and the fifth is for $D_F = 33$ at which value one full cycle is complete for $h = 0.145$. We can clearly see here the π/h dependence of the wavelength of the oscillation. For a value double the original, the wavelength is halved, and vice versa. The oscillatory behavior looks very regular and fairly sinusoidal at $H_B = 0.5$, except for some minor irregular variations which are more prominent for $h = 0.29$. However, for the larger barrier value of the bottom panel, the oscillatory pattern is less sinusoidal,

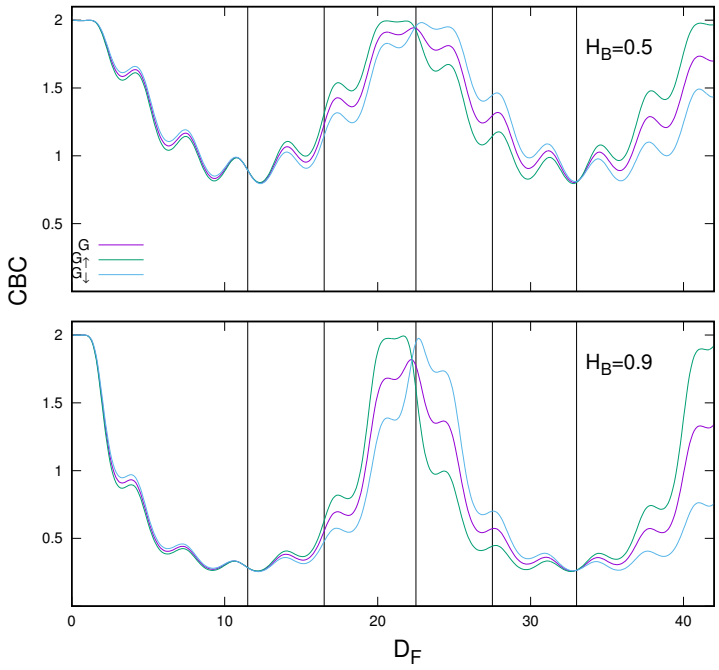

Figure 3.4: The critical bias conductance (CBC) (total, sin-up and spin-down) for an infinite $N/F/S$ system as a function of D_F. The top panel and bottom panels have a barrier $H_B = 0.5$ and $H_B = 0.9$ respectively, both at the N/F interface. We plot the thickness dependence for approximately two periods of the π/h oscillation. We also see smaller, superimposed oscillations with periodicity of π.

with a sharper dependence of the ZBC on D_F at the ZBC maxima and a broadening of the ZBC minima. For the stronger barrier only a reduced range of thicknesses have a ZBC peak conductance feature, which qualitatively agrees with what was found [79] in non-homogeneous S/F structures. Near the vertical lines, we also see a slight change in the phase of the oscillation for the stronger barrier. The periodic behavior breaks down for very small values of D_F where the ZBC becomes constant and independent on h.

Following up on this we plot, in Fig. 3.4, the critical bias conductance as a function of D_F, for both $H_B = 0.5$ and $H_B = 0.9$ (top and bottom panels respectively) at $h = 0.145$. We do so for the spin-split conductance components, which do not have the same CBC value, as well as for the total conductance. We see the same overall periodic structure as in the ZBC, with a π phase difference, since the CBC maxima occurs at the ZBC minima. There is also a minor oscillatory behavior with wavelength π superimposed on

the broader π/h oscillations: this is unobservable in the ZBC. The π oscillations are explained in Sec. 3.2.2. The spin-up and spin-down conductances cross over at the CBC maxima and they also converge at the CBC minima (where there are ZBC maxima). Between nodal points there is a difference in the spin-split conductance components that reverses between a dominant spin-up or dominant spin-down conductance. The separation becomes greater as D_F increases, or as the barrier strength increases.

We have found, using approximate analytic results, a regular, periodic behavior in the conductance features as a function of the ferromagnetic layer thickness. We have also found a subgap bias conductance peak, the prominence of which increases with the strength of the scattering barrier at the N/F interface. This peak is due to the splitting of the spin-up and spin-down conductances. This analysis will be helpful in interpreting the numerical results below.

3.3.2 N/F/S spin-split conductance

To make the discussion of our numerical spin valve results more understandable, we start with a brief discussion of a simpler finite size, $N/F/S$ structure, with a single barrier at the N/F interface: this is similar to the case studied in our analytic results. The calculation is now numerical and fully self consistent.

In Fig. 3.5 we plot the total conductance G as a function of the rescaled bias voltage E, together with the spin-up and spin-down conductance contributions. We do so in four panels corresponding to varying intermediate F layer thickness D_F, with fixed $D_N = 90$ and $D_S = 180$ in our dimensionless units. We take the scattering strength at the N/F interface of $H_B = 0.5$. The variation in D_F is chosen, as in our non-self-consistent results, to include a thickness variation that encompasses a full period of the conductance's subgap peak behavior, in a range compatible with our clean limit assumptions. The most obvious difference between the results of the non-self-consistent analytic calculation and those obtained via the numerical self-consistent procedure is that the latter case leads to a varying critical bias. This has been found and discussed previously in Chapter 2 and is directly related to the drop in the pair potential due to the proximity effect of the pair amplitude.

The first (upper left) panel of Fig. 3.5, corresponds to the situation where the ZBC is large and the CBC is low. The critical bias itself is significantly smaller in the

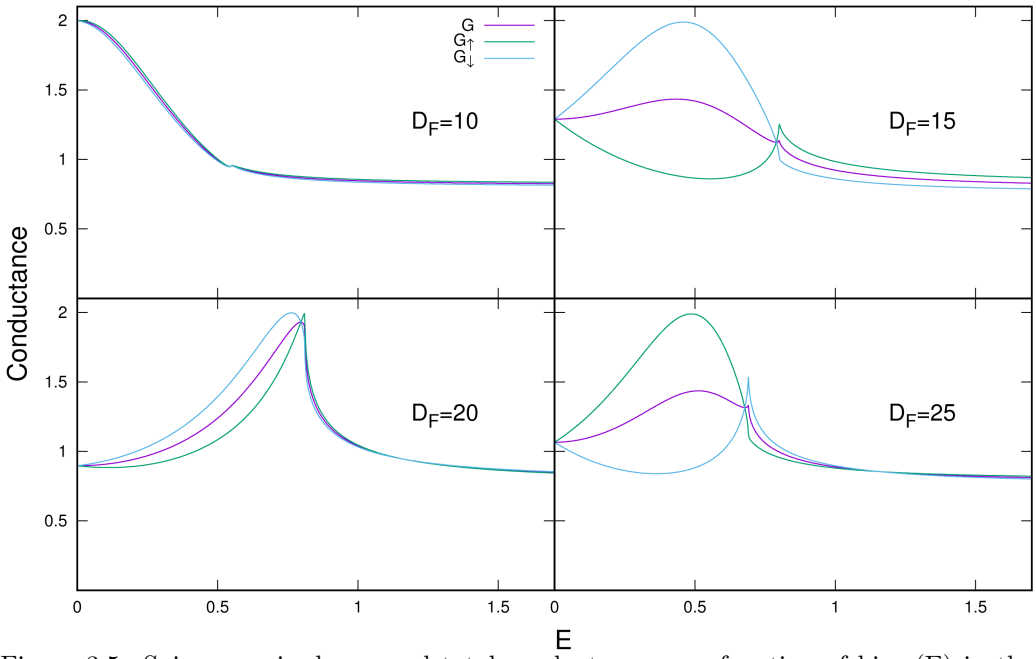

Figure 3.5: Spin-up, spin-down, and total conductance as a function of bias (E) in the finite $N/F/S$ system with $D_N = 90$ and $D_S = 180$. Conductances are calculated numerically using a self-consistent method. A barrier $H_B = 0.5$ is at the N/F interface only. The four panels are for different values of D_F, which are plotted for intervals of a quarter period of the spatial dependence.

self-consistent case, and there is little difference between the spin-up and spin-down conductance curves. Just as in the analytic case, this behavior is periodic with D_F and occurs again near $D_F = 30$ (not shown). In the second panel, we see the transition in the spin-split conductance, with a subgap peak in the total G due to the opposing behavior of the spin-up and spin-down conductance components. The spin-up conductance displays a positive concavity and a cusp feature at the critical bias, while the spin-down conductance displays a negative concavity with a weaker shoulder feature at the CB, similar to those found in our analytic calculation. Although the critical bias conductance depends on the spin, the CB value itself does not. This is because both spin channels interact with the same effective pair potential, which for the single-ferromagnet system, is spin independent since the Hamiltonian commutes with S_z.

In the third panel, we see the spin-split and total conductance peak locations converging towards the critical bias. Although not shown here, the relative behavior of

the spin-up and spin-down conductance switches abruptly for slightly different values of D_F, with a sharp transition similar to what is seen in the ZBC peaks of Fig. 3.4 in the analytic calculation. In the fourth panel, we see another subgap conductance peak similar to that in the second panel but now with the spin-split conductance components switching behavior, as was the case in our analytic calculation.

The spatial period we have considered corresponds to a wavelength π/h for our value of h. We conclude that the self-consistent behavior of the $N/F/S$ conductance qualitatively displays the same periodic behavior as revealed by the analytic non-self-consistent calculations. However, as mentioned above, the CB is now dependent on D_F as can clearly be seen by looking across the four panels. In subsection 3.3.3, we will find a further, more complex behavior by introducing an angular dependence on the system, which affects not only the spin-split conductance peaks but also the critical bias. As in the non-self-consistent, infinite case, the strength H_B of the interfacial scattering at the N/F interface enhances the peak conductance behavior, although we do not display this feature here. Furthermore, the increase in the barrier strength increases the critical bias value, making the analytic result approximation less inadequate in the strong-barrier case. Thus, the existence of the subgap conductance peak is verified for both the analytic and numerical calculation, and the peak value is mostly independent of the barrier height H_B.

3.3.3 F/N/F/S spin-split conductance

We now proceed, in this subsection, to the case of major theoretical and practical interest, where we include the outer ferromagnet, realistic, finite thicknesses and consider all interfacial barriers. We study, in the spin valve configuration, the dependence on the relative orientation of the exchange fields of the charge transport. This angular dependence is particularly important when applied to spin valves, as any angular dependence in the conductance constitutes a "valve effect" that can be exploited. We have studied such effects in in Chapter 2 for a variety of physical parameters. In this subsection we continue to focus on the intermediate F_2 layer dependence and the oscillatory behavior of the peak conductance, which we have already noted in the $N/F/S$ case. Therefore, we keep D_{F1} and D_N fixed (at values 30 and 60 respectively) and vary D_{F2} over a moderate range of values encompassing a full period, as explained above. We concentrate

on a small subset of interfacial scattering parameters, and on the spin-split effects that arise as D_{F2} varies.

In Figs. 3.6 and 3.7 we plot the spin-split and the total conductance as a function of the misalignment angle ϕ for a single interfacial barrier, located at the N/F_2 interface, as was done in Fig. 3.5. Introducing this barrier best exhibits the behaviors of the peak conductance that can occur. We will later include one full set of barriers, in Fig. 3.8. We will also in this case be plotting the dependence of the conductances on the misalignment angle ϕ. Therefore, we subdivide each figure into three parts: (a) The spin-up conductance, (b) the spin-down conductance, and (c) the total conductance. In each of these parts the panels correspond to different values of D_{F2}, as indicated.

In Fig. 3.6 we plot the mentioned quantities as a function of the bias and ϕ for a moderate barrier value $H_{B2} = 0.5$. Here, we see that the spin-up and spin-down components (Figs. 3.6a and 3.6b respectively) are highly dependent on the relative angle of magnetization. It is obviously no coincidence that the spin-up conductance very closely resembles that of the spin-down conductance for supplementary angles. Much of this resemblance is due to the change in ϕ being accounted for, in large part, by a purely mathematical rotation of the spin-split conductance as given by Eq. (3.8). Thus, it is seen that under a rotation by an angle θ, $G_\uparrow(\theta) = G_\downarrow(\pi - \theta)$ and vice versa. The angular dependence of each spin component closely resembles a combination of $\phi = 0$ of the spin-up and spin-down conductance, rotated into the respective ϕ basis via Eq. (3.8) for $\theta \to \phi$. For the same reason, it should be no surprise that a subgap peak in the spin-split conductance is found near $\phi = 90°$, since this can be largely described by a combination of the spin-up and spin-down conductances, as is the case with the total conductance. However, not all the differences in the features between the spin-up and spin-down conductances can be explained by this rotation, and a true angular dependence exists that is different for each component of the spin-split conductance. This yields a much more complex angular dependence in the total conductance (Fig. 3.6c).

In Fig. 3.6a, we plot the spin-up conductance. We see a considerable spread in the critical bias. The angular dependence is relatively weak in the first panel and becomes much stronger in the other three. In the second panel, the CB increases for angles greater than 90° and decreases for angles less than 90°. In the third and fourth panels, we see

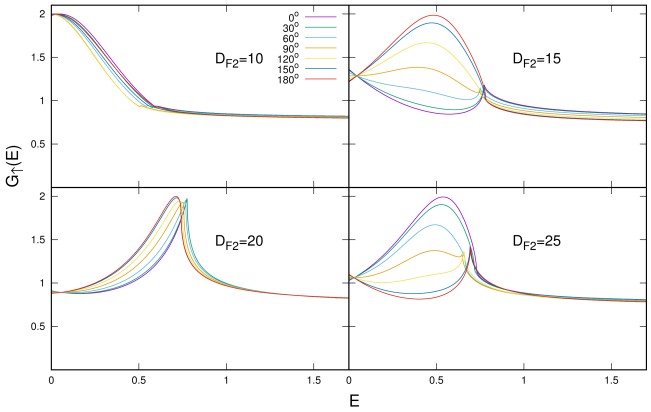

(a) The spin-up conductance.

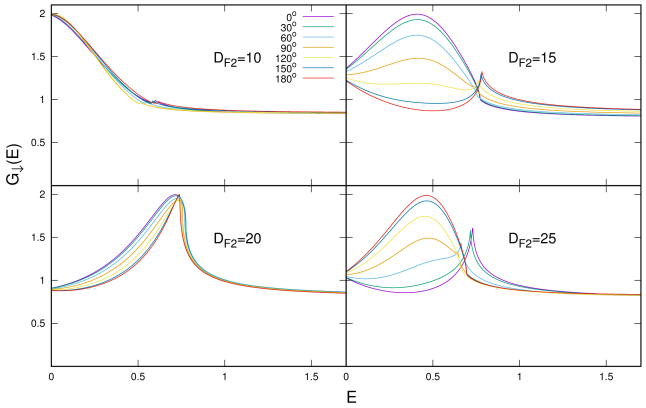

(b) The spin-down conductance.

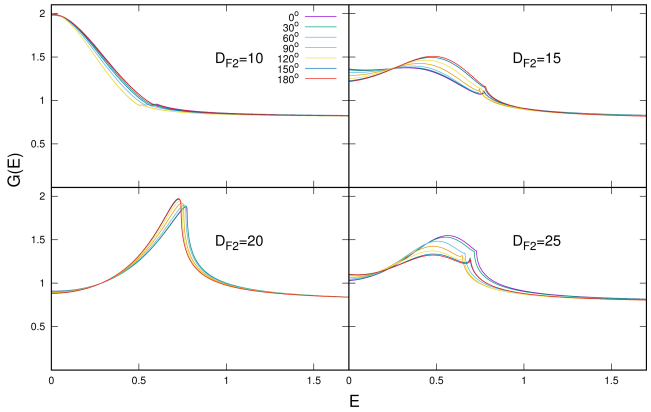

(c) The total conductance.

Figure 3.6: Spin-split and total conductance as a function of the bias and ϕ. The above plots are for the $F_1/N/F_2/S$ system with thicknesses $D_{F1} = 30$, $D_N = 60$, $D_S = 180$ and a single barrier $H_B = 0.5$ at the N/F_2 interface. The four panels in each subfigure are for different values of the intermediate F_2 layer thickness in the periodic intervals of one quarter of a period.

the opposite: the CB decreases for $\phi > 90°$ and increases for $\phi < 90°$. Recall that in the $N/F/S$ case we saw the spin-up and spin-down conductance swap behavior in panels two and four of Fig. 3.5, with a transition occurring in panels one and three. Similarly, we see here the CB behavior also making this transition in its angular dependence. The cusp and shoulder behavior of the CBC is not qualitatively changed by the introduction of the second ferromagnet. We also see a split in the ZBC.

To complement the previous subplot, we next display, in Fig. 3.6b, the spin-down conductance. As mentioned above, the behavior of this quantity is similar to that of the spin-up conductance, but with an angular dependence shifted by π. The angular dependence of the ZBC and the CBC have dramatically changed, with opposite behavior. The ZBC no longer has a crossover in the low bias regime. In effect, the introduction of the second ferromagnet takes the crossover node of the ZBC seen in the $N/F/S$ case (see Fig. 3.5) and moves it to the right in the spin-up conductance and to the left in the spin-down conductance. The CBC for the spin-down conductance experiences broadening, in direct opposition of the spin-up conductance, as can be seen best in the right hand panels (panels two and four). The angular dependence of the CB also broadens in these two panels. In panel three, we see the CB values move closer together and reverse the order of their angular dependence. This is explained by the spin-up conductance and spin-down conductance being at different phases in their D_F periodicity. In panel three, we see the critical bias (and the overall conductance) behavior transition in its angular dependence from that of panel two to that of panel four. From the CB features plotted, we see, due to the spin-valve effect, that the spin-down conductance is slightly advanced in its phase, while the spin-up conductance lags behind.

Finally, in the last panel set, Fig. 3.6c, we analyze the overall impact of the second ferromagnetic layer by plotting the total conductance, which can then be compared to that in Fig. 3.5. The total G, as given by Eq. (3.7), is not, unlike in the $N/F/S$ case, simply the average of the spin-up and spin-down conductances, because the outer electrode F_1 is populated with a majority of spin-up electrons: the total conductance is now weighted more heavily towards the spin-up value. Therefore we see an angular dependence in the total conductance that is more reminiscent of that of the spin-up conductance. This can be seen in the similar CB angular dependence as well as the ZBC and CBC dependence. The combination of spin-up and spin-down conductance

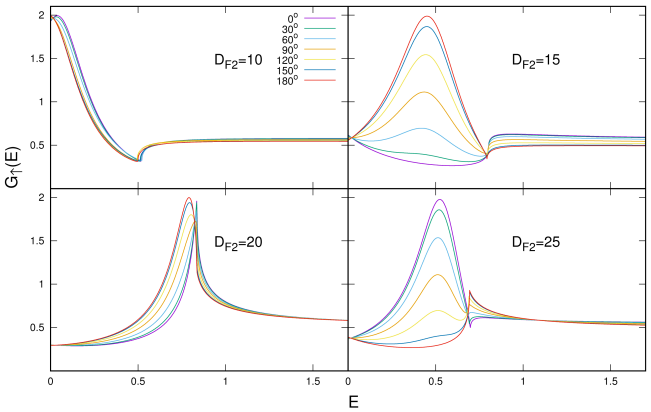

(a) The spin-up conductance.

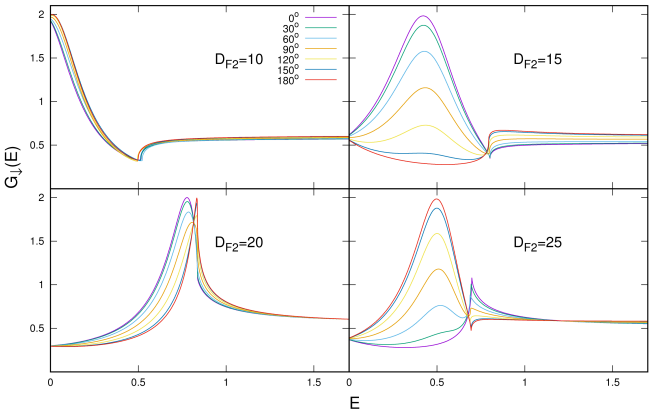

(b) The spin-down conductance.

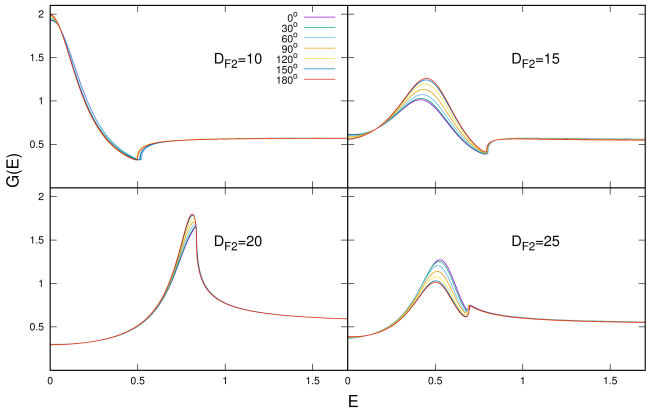

(c) The total conductance.

Figure 3.7: Spin-split and total conductance as a function of the bias and ϕ. The above plots are for the $F_1/N/F_2/S$ system with thicknesses $D_{F1} = 30$, $D_N = 60$, $D_S = 180$ and a single barrier $H_B = 0.9$ at the N/F_2 interface, significantly higher than that used in Fig. 3.6. The four panels in each subfigure are for different values of the intermediate F_2 layer thickness as in Fig. 3.6.

leaves us with a smaller subgap peak in the total G, for all angles. Generally, we see a significantly reduced angular dependence when compared to the spin-split conductance, except for the ZBC and the CBC. We also see that the cusp and shoulder CB features are less pronounced. There is a crossover node in panels two and four as we saw with the spin-up conductance, however this is not an exact "node" as the conductance does not cross over at precisely the same bias for all angles. In panel three, we actually see a monotonically increasing peak conductance, even though neither the spin-up nor spin-down conductance feature this monotonic behavior. In this transition, the phase difference of the spin-up and spin-down oscillations with respect to D_{F2} has a greater impact on the CBC behavior of the total G than for thicknesses such as in panels two and four.

In Fig. 3.7 we study the impact of the barrier strength on the spin-split conductance by increasing the parameter barrier value used in Fig. 3.6 from $H_{B2} = 0.5$ to $H_{B2} = 0.9$, the value used in Fig. 3.2. We have found in previous work [67] that an increase in barrier strength can lead to a decrease in angular dependence, particularly for the critical bias. We have also found above, in the $N/F/S$ case, that increasing the barrier strength can enhance the subgap conductance peak behavior. Below we analyze the combined effect that this change makes on our results.

In Figs. 3.7a and 3.7b we plot the spin-up and spin-down conductances, respectively, for this larger barrier value. We see the supplementary angle relation in the ϕ behavior of the spin-split conductance. We also see an angular dependence arise in the CB and the ZBC, as we did in Figs. 3.6a and 3.6b, but this angular dependence is much smaller: this reflects the overall suppression of the proximity effects by the higher barrier. Furthermore, the difference between the spin-up and spin-down conductances (besides the switching of conductance behavior to supplementary angles) is greatly diminished. We do see a small broadening in the angular dependence of the CB, as well as a better defined cross-over node. This leads to a total conductance that has, in the zero bias and critical bias regions, little angular dependence, as we see in Fig. 3.7c. However, the subgap conductance peak still maintains a strong angular dependence, rivaling that of the $H_{B2} = 0.5$ case. This is because much of the angular dependence here comes from the difference in spin-up and spin-down electron populations emanating from the F_1 layer, in which the large difference between spin-up and spin-down conductance

counteracts the decrease in angular dependence of the other conductance features. We also note that for higher barriers this subgap peak is more pronounced. The reason is twofold: the increased difference between the spin-up and spin-down conductances creates a large peak in the total G, as we saw in Fig. 3.2, and the decrease in the angular dependence of the CB provides less overlap, which prevents the hybridizing of the cusp and shoulder CB behaviors, and makes the drop-off sharper at the CB.

We now examine in Fig. 3.8 the realistic case where there are barriers at all three interfaces: $H_{B1} = H_{B2} = 0.5$, $H_{B3} = 0.3$ for the F_1/N, N/F_2, and F_2/S interfaces respectively. These values are likely a good approximation to real experimental conditions as there are unavoidable interfacial defects even in the best prepared samples of heterostructures. The introduction of the F_2/S barrier can slightly flatten the subgap peak conductance feature because a barrier at that interface reduces the proximity effect. However, this effect remains small, and when coupled with the moderate F/N barriers, it leaves the conductance with well defined peaks, as we will see below. As we saw in Chapter 2, having two interfacial barriers, particularly with similar values, can produce resonance effects in the low bias conductance for certain thicknesses. There are a large number of parameter choices that can affect the conductance features in a variety of ways, but what is of interest here is how robust the oscillatory subgap peak behavior is.

In Fig. 3.8a we plot the spin-up conductance for these barrier values, and in Fig. 3.8b the spin-down conductance. The first thing to observe is the slight change in the D_{F2} values displayed in the first three panels from the values used in previous figures. We show, in the first panel, thickness values closest to the transition where the subgap conductance peak is now closest to zero bias. The ZBC peak conductance in panel one is very sensitive to small changes in D_{F2}, and it is important to try to tune precisely to that value. This sensitivity indicates that these barriers can have a large impact on the phase of the oscillatory behavior of the peak conductance. We see in the first panel of our plots a large angular dependence at the peak bias (which is slightly greater than zero), but very little angular dependence on the ZBC. The angular dependence in the subgap bias range is large, as we found in the single barrier, $H_{B2} = 0.9$ case (see Fig. 3.7). The high bias conductance ($E > 1$) now displays a large angular dependence in panels one, two, and four, but this dependence is much smaller in panel three where the subgap

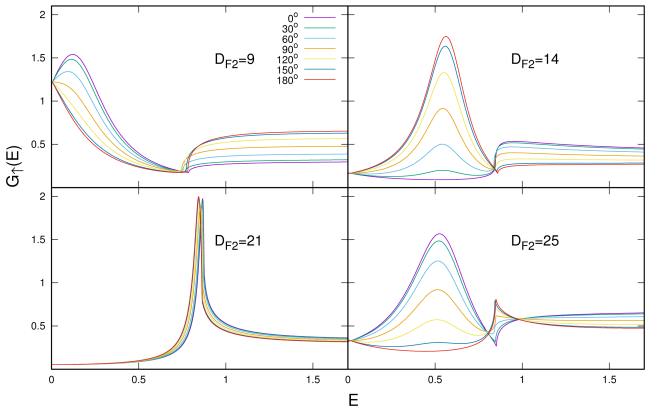

(a) The spin-up conductance.

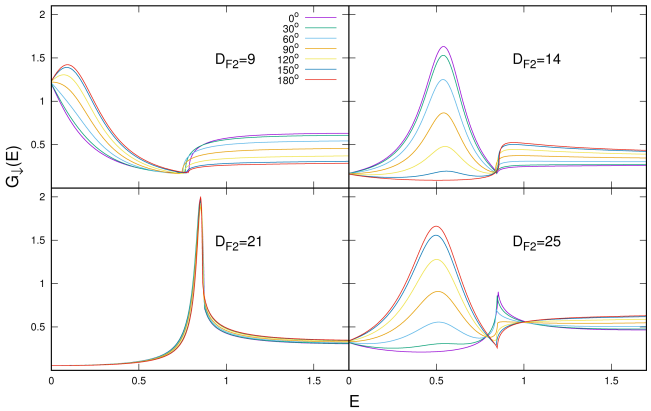

(b) The spin-down conductance.

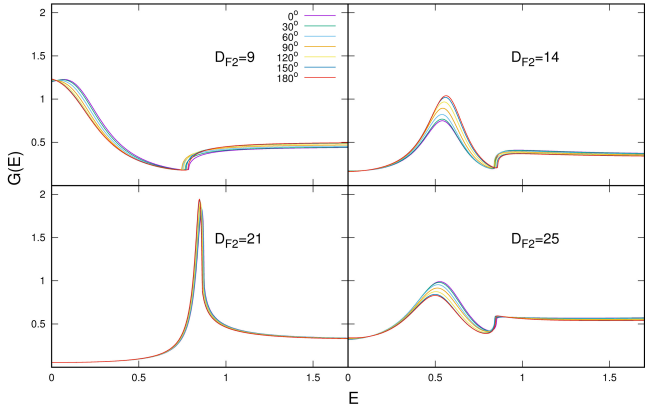

(c) The total conductance.

Figure 3.8: Spin-split and total conductance as a function of the bias and ϕ. The above plots are for the $F_1/N/F_2/S$ system with thicknesses $D_{F1} = 30$, $D_N = 60$, $D_S = 180$ and realistic barriers H_{Bi} equal to 0.5, 0.5, and 0.3 at the F_1/N, N/F_2, and F_2/S interfaces respectively. The four panels in each subfigure are for different values of the intermediate F_2 layer thickness in the intervals of one quarter period.

peak transitions at the CB. Examining the spin-up and spin-down conductances, we see greater broadening with ϕ in the CB and the CBC than we did in Fig. 3.7 in panels two and four. In panels one and two, we see some slight phase advancing/lagging, but the other conductance features are quite similar. These transitional panels have peaks which are sharper than in the previous results, and the ZBC peak is lower in value.

In Fig. 3.8c we plot the total conductance. Its behavior is similar to that of Fig. 3.7c but there are some key differences. Despite the F_2/S barrier, the subgap conductance peak is sharper in panels two and four. Furthermore there is a larger, more noticeable angular dependence in the CB, as well as in the high-bias conductance. The ZBC, however, has a smaller angular dependence, but does still feature a small-bias crossover point before the subgap peak conductance. In panel three we see again an angular dependence in the CBC similar to that in Fig. 3.6c. Overall, the salient point is that the subgap peak behavior is not only still present, but in fact more pronounced, with a large angular dependence in the peak conductance in panels two and four. This peak conductance is oscillatory with D_{F2}, with only a slight change in phase resulting from the introduction of realistic barriers. This robust angular dependence of the peak conductance can potentially be exploited, as the subgap conductance peak leads to an angularly dependent change in the excess currents at high biases.

3.4 Conclusions

We have analyzed here the spin-split conductance in $F_1/N/F_2/S$ spin valve systems using numerical, self-consistent methods. We have also considered $N/F/S$ systems using also an approximate but analytic method. We have done so in the clean limit, but assuming imperfect interfaces that can be approximately described via a delta function scattering potential. We use experimentally relevant parameters in accordance with Ref. [9]. We have found a peak in the subgap conductance that is periodic with the intermediate F layer thickness. This peak conductance is due to the separate behavior of the contributions to the total conductance from incoming spin-up and spin-down electrons. We collectively call these contributions the spin-split conductance. Our results show that the subgap conductance peak position oscillates between the zero bias and the critical bias values as D_F varies. We find that at least one spin band

conductance has a maximum close to $G = 2$ in our natural units at a single bias value in the subgap region, near where the opposite spin band has a minimum. At this subgap bias, we find a pronounced peak in the total conductance due to the spin-up and spin-down conductances being very different at this bias, while they converge in the ZBC and CBC. In N/S systems with moderate or tunneling barriers, a peak in the conductance occurs at the critical bias before decreasing to normal conductance [50]. In the F/S case we now see a second, subgap peak that is robust to interfacial scattering, with large angular dependence in the $F_1/N/F_2/S$ spin valve. The subgap peak and the ZBC resonance peak we find are qualitatively similar to the "double peak spectra" and the "zero peak spectra" seen in the tunneling conductance measurements, reported in Ref. [79], made via scanning tunneling spectroscopy in S/F structures with a non-homogeneous (Holmium) ferromagnet. Our theoretical work, however, focuses on spin-valve structures.

Our spin valve results are numerical. It is usually difficult to gain physical intuition from purely numerical results. In an effort to gain additional intuitive understanding, we have used an approximate, non-self-consistent, analytic approach for an infinite $N/F/S$ structure. We examined the origin of the spatially periodic behavior by examining the ZBC and CBC as a function of the thickness of the F layer. In both cases, we found that the periodic spatial dependence is due to the interaction of the spin dependent plane wave amplitudes in the ferromagnet, which leads to a wavelength of π/h in the conductance peak (h is the exchange field of the intermediate ferromagnet). The location of the subgap conductance peak was found to oscillate between zero bias and the CB. The spin-split conductance as a function of bias consequently switches behavior between spin components with changes in F layer thickness, transitioning across the CBC and ZBC peak conductances. In the analytic non-self-consistent approximation, there is no change to the critical bias itself, which is incorrect. We also established the effect of the interfacial barrier heights on the conductance features. The subgap conductance peak is only weakly dependent on the barrier strength. Furthermore, when this peak occurs in the middle of the subgap region, the ZBC and CBC values decrease at a faster rate with increasing barrier strength, leaving a more pronounced subgap peak at higher barrier strengths.

Turning to the numerical self-consistent results for the $F_1/N/F_2/S$ spin valve, we find

the same periodic effects, with an additional dependence of the spin-split conductance on the CB. This is also found for a finite $N/F/S$ structure. This dependence on the CB is reduced by high barriers. We analyze the dependence of the spin-split conductance on the angle ϕ between the internal exchange fields in the magnets F_1 and F_2, in the $F_1/N/F_2/S$ system. Part of the angular dependence of the spin-split conductance in this system can be attributed to rotations in spin space (see Eq. 3.8) but since (except at $\phi = 0$ and $\phi = \pi$), S_z does not commute with the Hamiltonian, we find that this dependence on ϕ is beyond that arising from a choice of spin quantization axis. This affects the CB, the CBC, and the ZBC in different ways for the spin-up and spin-down components, causing broadening of the CBC peaks and CB values, as well as shifting the cross-over points where G is approximately equal for all angles ϕ. There is a general shift in the spin-split conductance's bias dependence, in opposite directions for each component, with a nodal point, located at zero bias in the $N/F/S$ system, shifting to higher bias values for spin-up and to lower ones for spin-down. The end result is that the total conductance has a complex angular dependence, where the subgap peak becomes less prominent, as the relative shift of the spin-split conductance means that each component's respective (at supplementary angles) extrema are no longer aligned, leaving their combination (i.e. the total conductance) more smeared, and the other conductance features less pronounced. Nevertheless, a subgap conductance peak with a very strong angular dependence remains in the $F_1/N/F_2/S$ structure. This angular dependence is protected by the subgap peak, which does not diminish strongly with increasing barriers.

The sub-gap conductance peak, due to the spin-split conductance, is an important and prominent feature that can be exploited in future superconducting spintronic devices. One of our primary goals here has been to determine and improve the efficacy of a superconducting spin valve in which the valve effect is defined by the angular dependence of the exchange fields. The sub-gap peak is well defined when the interface between the superconductor and the valve is reasonably clean, even when the interfacial scattering within the valve is non-negligible. Although this can lead to very low angular dependence when the peak conductance is at zero bias or at the CB, the angular dependence is large and robust against interfacial scattering for definite values of the intermediate ferromagnetic layer thickness. By tuning the thickness to one of these

intermediate values, a valve effect in the excess current can be attained, as we see then a very large angular dependence in the spin-split and total conductance. This would have a considerable effect on the quality of such spin valve devices.

Chapter 4

Spin Transport in Superconducting Spin Valves

4.1 Introduction

The work presented in this chapter is based on a previous publication Ref. [69] which has been edited for use in this thesis.

In Chapter 2 we introduced our work on charge and spin transport in $F_1/N/F_2/S$ superconducting spin valves. In it, we discussed the charge transport dependence with many realistic parameter values. The spin transport calculations were done only in the $F_1/F_2/S$ system with no normal metal spacer and a very limited set of parameters. In this chapter, we extend our calculations of the spin transport quantities to include realistic interfacial scattering and we study the dependence on the geometrical and physical parameters. Superconducting spintronics garners intrinsic scientific interest because of the intricate proximity effects [22] involved between ferromagnets (F) and superconductors (S). A charge current interacts with the exchange field of the first ferromagnetic component, inducing a polarization in its spin degree of freedom. The second F component is introduced as a spin selector and detector, in which a spin current and spin accumulation is predicted and measured [88, 89]. The charge current and the relative orientation of the exchange fields of the two ferromagnets determine the spin-transport properties of these devices. In their application to non-volatile memory, the magnetic memory is current-switched (as opposed to magnetic field-switched) via the

spin transfer torque (STT) [90, 91, 92, 93]. This gives the devices an advantage in power consumption and scalability [70]. Thus, superconducting spintronic devices, including spin valves $F_1/N/F_2/S$, have been proposed and studied [4, 5, 40, 41, 42, 43, 44]. We found in Chapters 2 and 3 that the charge transport properties are non-monotonic with the relative orientation of the ferromagnetic exchange fields due to the F/S proximity effect [22], which we discussed in Sec. 1.2. We see in this chapter that the spin transport is non-monotonic and highly dependent on the physical parameters such as the layer thicknesses and interfacial quality.

In these $F_1/N/F_2/S$ devices the presence of (usually traditional, well-understood) superconductors in proximity to ferromagnetic materials fundamentally affects spin transport. Furthermore, their ultra-low power consumption offers a distinct advantage over standard spin valves, particularly in memory applications. Many such devices have been proposed [4, 5, 6]. The first spin switch device using a superconducting current was reported in Ref. [94]. Other superconducting spin valves with $F_1/N/F_2/S$ layered structures have since been studied [40, 41, 42]. The currents in such devices are in general spin-polarized and can potentially be controlled by STT in nanoscale devices, just as in traditional spin valves. However, they are not merely regular spin valves with spin currents. Rather, these are novel structures with their own distinct set of spin transport properties due to the F/S proximity effects [22]. Below, we discuss some of the peculiar properties of these devices as they are relevant to our study.

Superconductivity results from the formation of Cooper pairs consisting of opposite momentum electrons [16]. In the usual s-wave superconductivity, these pairs form a singlet state. Ferromagnetism, on the other hand, has a strong tendency to break these singlet pairs, while favoring in principle triplet pairing states with $m_z = \pm 1$. In Sec. 1.2 we see that ferromagnetism and s-wave superconductivity are largely incompatible. Indeed, the ordinary superconducting proximity effects in F/S heterostructures result in a heavily damped, oscillatory behavior of the singlet pair amplitudes in the F layer regions [26, 27], caused by Cooper pairs acquiring a center of mass momentum [25]. This oscillatory behavior is critical to understanding F/S heterostructures, as it makes all transport measurements highly dependent on the thicknesses of each material layer as we saw for charge transport in Chapters 2 and 3. However, proximity effects in F/S structures are by no means limited to those arising from the s-wave

Cooper pairs in the S material. Indeed, there are long range proximity effects from triplet pair correlations that are induced in the structure by the presence of nonuniform exchange fields [29, 30, 31, 32, 81]. This conversion is possible because, unless all exchange fields are collinear, the Hamiltonian does not commute with S_z, the z component of the Cooper pair spins: thus it is not conserved.

Because of the Pauli principle, the triplet correlations for a spatially even Cooper pair configuration must be odd in frequency [33] or equivalently in time [31]. In the presence of a uniform exchange field, only the $m_z = 0$ triplet component may be induced. The required non-uniform exchange field can be introduced in a variety of ways: for example one can have a $F_1/F_2/S$ heterostructure with noncollinear exchange fields, or a single F layer with a non-uniform magnetization texture such as one may have with magnetic domains or, in a more controllable way, by using a magnet such as holmium [45, 46, 47, 71] in which the magnetic structure is spiral. In these cases the presence of $m_z = \pm 1$ pairs is compatible with conservation laws and the Pauli principle, and in fact such pairs are usually induced. The exchange fields do not necessarily break these triplet correlations, and thus the proximity effect can be long ranged [23, 34, 35, 36, 37, 38, 39] in F. In heterostructures which include two ferromagnetic layers F_1 and F_2, as we consider in this thesis, we have seen an interesting angular dependence of the results on the misalignment angle ϕ between the two F layers, as their orientations vary from being parallel, to orthogonal, to antiparallel. In traditional spin valves, this angular dependence is characterized by the magnetoresistance obtained by comparing the parallel (P) and antiparallel (AP) configurations [3]. In the superconducting devices, as triplet pairs are induced, singlet pair amplitudes decrease, diminishing the strength of the superconducting pair potential and influencing the transport properties. As ϕ is varied between 0° and 180° a unique angular dependence that is nonmonotonic is produced.

The superconducting proximity effects discussed above affect both the thermodynamic and the transport properties of the device. A fundamental contribution to both arises from Andreev reflection [49] at the interfaces. Andreev reflection is the process of electron-to-hole conversion by the creation or annihilation of a Cooper pair, occurring at the interface of a superconductor. There are two types of Andreev reflection: conventional and anomalous. In conventional Andreev reflection, the reflected electron/hole

has spin opposite to that of the incident particle. In anomalous Andreev reflection, these electron/hole pairs have the same spin. It has been shown [41, 52, 53, 54, 55] that normal and anomalous Andreev reflection are correlated with triplet proximity effects. Understanding and accurately characterizing the transmission amplitudes of the Andreev reflections is pertinent to all transport calculations in superconducting heterostructures [50, 51, 56, 57], particularly for quantities with spatial dependence such as the spin current and spin transfer torque.

The practical fabrication of $F/F/S$ valve structures results in devices that deviate very significantly from theoretical idealizations. To be able to modify the angle ϕ requires the insertion of a normal metal spacer between the F layers, so that they are decoupled and the magnetization of one of them can be rotated individually. In addition, even high quality interfaces between all layers involved are not perfect: some interfacial scattering is inevitable and transport [5] in superconducting spin valves is very sensitive to it [57, 67], as is also the case [95] for spin transport in traditional spin valves. It has been shown that, if the the normal spacer and the interfacial scattering are properly taken into account, then it is possible to quantitatively characterize to high accuracy [9] the thermodynamic properties of high quality devices. In Chapter 2, we have examined the charge transport properties of $F_1/N/F_2/S$ heterostructures with an emphasis on practical, realistic layer thicknesses and interfacial scattering parameters. However, spin transport properties, such as spin-current and the STT, were calculated only for the "proof of principle" ideal case with no normal metal spacer or interfacial scattering parameters.

Developments in deposition techniques have allowed for the fabrication of spintronic devices [5] that can be described via clean limit methods. These are the high quality devices [9] which are our focus in this chapter. Thus, we assume geometrical (thickness of the layers, including that of N) and material parameters appropriate to the Co, Cu, and Nb layers used there [9]. The charge and spin transport properties depend strongly on the applied bias voltage. Many of their features change [67] rather abruptly when the applied voltage reaches the critical bias (CB) value, which is related to the self-consistent pair potential within the superconductor. This value is less than the pair potential bulk value due to the proximity effects. The transport properties are quite different for an applied voltage bias below and above the CB. This effect is also

dependent on the misalignment angle of the exchange fields, usually in a nonmonotonic way as we saw in Chapter 2. Here, we examine the dependence of the spin-transport properties on the layer thicknesses (the importance of which has been mentioned above), the interfacial scattering strengths, and the applied bias voltage, including CB effects. We hope to establish a broad understanding of how sample quality and geometry affect spin transport results in $F_1/N/F_2/S$ systems so that they may then be compared to experimental results.

In our calculations, we use a self consistent solution to the Bogoliubov de Gennes (BdG) equations [15] to calculate the pair potential. We then employ this potential in the transport calculations via a transfer matrix method (see Sec. 2.2.2). This method correctly incorporates the normal and Andreev reflection and transmission amplitudes of the electrons and holes. We evaluate the spin current, the STT, and the magnetization, all as functions of position within the $F_1/N/F_2/S$ heterostructure and of the applied bias. We examine their dependence on the misalignment angle ϕ. We also vary the layer thickness and the interfacial scattering strengths within bounds similar to those used in the study of the thermodynamic properties of similar systems [9]. Our focus will be the analysis of the physical parameters for experimental use, as well as on the underlying physics of the spin transport.

Spin transport is considerably more complex than charge transport. As opposed to the charge current, which is a constant through the sample due to charge conservation, the spin current varies with position, and this variation is related to the STT. Furthermore, since spin is a vector the spin current is in principle a tensor, although it does reduce to a vector in spin space in the quasi-one dimensional geometry we will consider here. Thus all quantities are spatially dependent. Together with the spatially oscillatory nature of the singlet and triplet amplitudes, we find a strong and intricate dependence of spin transport on the layer thicknesses. Furthermore, the proximity effects are particularly influential on the spin transport properties, as they relate to the spin-pairing and the induced triplets. We thus see a nonmonotonic dependence on ϕ, as well as a strong dependence on the interfacial scattering strengths. Interfacial scattering generally inhibits the proximity effects but, because there are several barriers, resonance features, such as those found in Chapters 2 and 3 for charge transport, can also arise. We will also analyze the average of the spin transport quantities over each layer: we

have found this particularly useful in studying the bias dependencies and in better establishing the underlying physical principles at work. We hope through this work to provide future experiments with some deeper context as to how these parameters may affect their results.

After this Introduction, we briefly review our methods for transport calculations in Sec. 4.2. The results, as well as their discussion, are presented in Sec. 4.3. We summarize our work in Sec. 4.4.

4.2 Methods

4.2.1 The basic equations

The geometry of the system we study is depicted in Fig. 1.3. The layers are assumed infinite in the transverse, x-z plane, and have finite widths in the y direction. This assumption makes the system quasi-one-dimensional. The magnetizations of the outer (F_1) and inner (F_2) layers are misaligned by an angle ϕ in the x-z plane. Our methods and procedures are ultimately based in Ref. [15] and are described extensively in Ref. [41] and Secs. 1.4 and 2.2. Many of the spin transport quantities have nonzero equilibrium values due to the STT and magnetic proximity effects, therefore we review both the equilibrium and transport calculations below.

The Hamiltonian appropriate to our system is

$$\begin{aligned}\mathcal{H}_{eff} &= \int d^3r \left\{ \sum_{\alpha} \psi_{\alpha}^{\dagger}(\mathbf{r}) \mathcal{H}_0 \psi_{\alpha}(\mathbf{r}) + \frac{1}{2} \left[\sum_{\alpha,\beta} (i\hat{\sigma}_y)_{\alpha\beta} \Delta(\mathbf{r}) \psi_{\alpha}^{\dagger}(\mathbf{r}) \psi_{\beta}^{\dagger}(\mathbf{r}) + H.c. \right] \right. \\ &- \left. \sum_{\alpha,\beta} \psi_{\alpha}^{\dagger}(\mathbf{r}) (\mathbf{h} \cdot \hat{\boldsymbol{\sigma}})_{\alpha\beta} \psi_{\beta}(\mathbf{r}) \right\}, \end{aligned} \tag{4.1}$$

where $\Delta(\mathbf{r})$ is the pair potential, and $\mathbf{h}$ is the Stoner field. The field $\mathbf{h}$ is taken along the z axis in the outer ferromagnetic layer F_1 and forms an angle ϕ with the z axis in the inner ferromagnetic layer F_2. This field is then zero in the superconductor S and normal metal spacer N. We have assumed equal magnitude of the fields $h_1 = h_2 \equiv h$ since in experiments the same material is typically employed for both ferromagnetic layers. $\mathcal{H}_0$ is the single-particle Hamiltonian, and it includes the interfacial scattering.

The indices α and β denote spin indices and σ_i are the Pauli matrices.

Performing a generalized Bogoliubov transformation, we take

$$\psi_\sigma = \sum_n \left(u_{n\sigma}\gamma_n - \eta_\sigma v^*_{n\sigma}\gamma^\dagger_n \right) \tag{4.2}$$

where $\eta_\sigma \equiv 1(-1)$ for spin up (down), and $u_{n\sigma}(\mathbf{r})$ and $v_{n\sigma}(\mathbf{r})$ are the spin-dependent quasiparticle and quasihole amplitudes. Due to the geometry of the system being quasi-one dimensional, the spatial dependence on $\mathbf{r}$ becomes a dependence on y alone. Then, we can rewrite the eigenvalue equation corresponding to the Hamiltonian given by Eq. (4.1) as

$$\begin{pmatrix} H_0 - h_z & -h_x & 0 & \Delta \\ -h_x & H_0 + h_z & \Delta & 0 \\ 0 & \Delta & -(H_0 - h_z) & -h_x \\ \Delta & 0 & -h_x & -(H_0 + h_z) \end{pmatrix} \begin{pmatrix} u_{n\uparrow} \\ u_{n\downarrow} \\ v_{n\uparrow} \\ v_{n\downarrow} \end{pmatrix} = \epsilon_n \begin{pmatrix} u_{n\uparrow} \\ u_{n\downarrow} \\ v_{n\uparrow} \\ v_{n\downarrow} \end{pmatrix}, \tag{4.3}$$

We use natural units $\hbar = k_B = 1$ and all terms above are implicitly a function of y. The quasi-one-dimensional Hamiltonian is $H_0 = -(1/2m)(d^2/dy^2) + \epsilon_\perp - E_F(y) + U(y)$ where $\epsilon_\perp$ is the transverse energy, so that Eq. (4.3) is a set of decoupled equations, one for each $\epsilon_\perp$. $U(y)$ is the interfacial scattering, which we take to be spin independent in the form $U(y) = H_1\delta(y - d_{F1}) + H_2\delta(y - d_{F1} - d_N) + H_3\delta(y - d_{F1} - d_N - d_{F2})$ where H_i are the scattering strengths of the respective interfaces. These scattering strengths are best characterized by the dimensionless parameters $H_{Bi} \equiv H_i/v_F$, where v_F is the Fermi speed in S. These scattering parameters are quite essential to characterizing possible devices, as even for clean interfaces, some scattering due to residual surface roughness is inevitable. Transport results turn out to be much more sensitive than thermodynamic quantities to interfacial scattering. The quasiparticle and quasihole amplitudes must be complex in order to calculate the spin current. This was not the case for the conductance, which relied only on the square amplitudes and thus, certain simplifications to the numerical calculations could be made. Greater care must be taken for the spin transport quantities.

All of the calculations must be done self-consistently to preserve charge conservation

(see Sec. 2.2.3). The self-consistency condition allows for the proper inclusion of the proximity effect, which is of primary importance to our study. It can be written as:

$$\Delta(y) = \frac{g(y)}{2}\sum_{n}{}' \left[u_{n\uparrow}(y)v^{*}_{n\downarrow}(y) + u_{n\downarrow}(y)v^{*}_{n\uparrow}(y)\right] \tanh\left(\frac{\epsilon_n}{2T}\right), \tag{4.4}$$

where $g(y)$ is the superconducting coupling constant in the singlet channel and it is nonzero in the S layer only. The set of eigenvalues is found for each $\epsilon_{\perp}$, and the index n in the sum refers now to all eigenvalues, i.e. it includes summation over $\epsilon_{\perp}$, while the prime symbol indicates that the sum is limited to states with eigenenergies within a cutoff ω_D from the Fermi level. The self-consistency procedure is this: we start with a suitable choice for $\Delta(y)$, compute the quasi-particle and quasi-hole amplitudes using Eq. (4.3), and obtain $\Delta(y)$ using Eq. (4.4). Then we repeat this process, substituting the iterated $\Delta(y)$ until the input of Eq. (4.3) matches the output of Eq. (4.4).

Self-consistency is fundamental in all transport calculations. It is a prerequisite for charge conservation [41, 62, 63, 64] as we have shown in Sec. 2.2.3. Another reason why transport is dependent on self-consistency is more obvious: as the pair potential changes, so does the energy spectrum within the superconductor. Proper inclusion of ordinary and Andreev reflection at the interfaces is obviously necessary for a proper account of the transport properties of heterostructures, and the variation of the self-consistent pair amplitudes is most pronounced at the superconducting interface due to proximity effects. Therefore, it is mandatory that we calculate transport using a fully self-consistent pair potential.

4.2.2 Spin transport Quantities

The spin transport related quantities we consider are the spin current, the STT, and the local magnetization. These are all studied as functions of applied bias voltage V. We aim to describe the position dependence of these bias-dependent quantities within the multi-layer structure, for a range of relevant values of the geometrical parameters, including ϕ. In our geometry the spin current is a vector in spin space:

$$S_i \equiv \frac{i\mu_B}{2m}\sum_{\sigma}\left\langle \psi^{\dagger}_{\sigma}\sigma_i\frac{\partial\psi_{\sigma}}{\partial y} - \frac{\partial\psi^{\dagger}_{\sigma}}{\partial y}\sigma_i\psi_{\sigma}\right\rangle. \tag{4.5}$$

The spin current density is not a conserved quantity within the ferromagnetic regions. We can relate its gradient to the local magnetization $\mathbf{m} \equiv -\mu_B \sum_\sigma \psi_\sigma^\dagger \sigma \psi_\sigma$, where μ_B is the Bohr magneton. The Heisenberg equation for the magnetization is

$$\frac{\partial}{\partial t} \langle \mathbf{m}(\mathbf{r}) \rangle = i \langle [\mathcal{H}_{eff}, \mathbf{m}(\mathbf{r})] \rangle . \tag{4.6}$$

From this, we can write the continuity equation for the local magnetization in the form:

$$\frac{\partial}{\partial t} \langle m_i \rangle + \frac{\partial}{\partial y} S_i = \tau_i, \;\; i = x, y, z \tag{4.7}$$

where $\boldsymbol{\tau}$ is the spin-transfer torque $\boldsymbol{\tau} \equiv 2\mathbf{m} \times \mathbf{h}$. In the steady state, $\partial m_i / \partial t$ is zero. This means that the spin current will not be constant within the ferromagnetic layers, and that the local magnetization, even in the steady state, is intrinsically tied to the spin current via the STT.

We can write the magnetization and the spin current in terms of the self consistent quasi particle and quasi hole amplitudes. In the low temperature limit, the expression for the local magnetization reads [41],

$$\begin{aligned}
m_x = &-\mu_B \left[\sum_n \left(-v_{n\uparrow} v_{n\downarrow}^* - v_{n\downarrow} v_{n\uparrow}^* \right) \right. \qquad (4.8a) \\
&\left. + \sum_{\epsilon_{\mathbf{k}} < eV} \left(u_{\mathbf{k}\uparrow}^* u_{\mathbf{k}\downarrow} + v_{\mathbf{k}\uparrow} v_{\mathbf{k}\downarrow}^* + u_{\mathbf{k}\downarrow}^* u_{\mathbf{k}\uparrow} + v_{\mathbf{k}\downarrow} v_{\mathbf{k}\uparrow}^* \right) \right] \\
m_y = &-\mu_B \left[i \sum_n \left(v_{n\uparrow} v_{n\downarrow}^* - v_{n\downarrow} v_{n\uparrow}^* \right) \right. \qquad (4.8b) \\
&\left. - i \sum_{\epsilon_{\mathbf{k}} < eV} \left(u_{\mathbf{k}\uparrow}^* u_{\mathbf{k}\downarrow} + v_{\mathbf{k}\uparrow} v_{\mathbf{k}\downarrow}^* - u_{\mathbf{k}\downarrow}^* u_{\mathbf{k}\uparrow} - v_{\mathbf{k}\downarrow} v_{\mathbf{k}\uparrow}^* \right) \right] \\
m_z = &-\mu_B \left[\sum_n \left(|v_{n\uparrow}|^2 - |v_{n\downarrow}|^2 \right) \right. \qquad (4.8c) \\
&\left. + \sum_{\epsilon_{\mathbf{k}} < eV} \left(|u_{\mathbf{k}\uparrow}|^2 - |v_{\mathbf{k}\uparrow}|^2 - |u_{\mathbf{k}\downarrow}|^2 + |v_{\mathbf{k}\downarrow}|^2 \right) \right] ,
\end{aligned}$$

where the first terms on the right side are the ground state local magnetization components, and the second terms denote the bias dependent contributions. We can define a direct analog of the spin accumulation by removing the first terms on the right side $\delta\mathbf{m}(V) \equiv \mathbf{m}(V) - \mathbf{m}(0)$, revealing the change in magnetization due to the finite bias.

We can use the same procedure for the spin current components, Eq. (4.5), and expand in terms of the u_n and v_n wavefunctions [41, 67]. In the $T = 0$ limit the result is:

$$S_x = \frac{-\mu_B}{m}\mathrm{Im}\left[\sum_n\left(-v_{n\uparrow}\frac{\partial v^*_{n\downarrow}}{\partial y} - v_{n\downarrow}\frac{\partial v^*_{n\uparrow}}{\partial y}\right)\right. \tag{4.9a}$$
$$\left. + \sum_{\epsilon_\mathbf{k}<eV}\left(u^*_{\mathbf{k}\uparrow}\frac{\partial u_{\mathbf{k}\downarrow}}{\partial y} + v_{\mathbf{k}\uparrow}\frac{\partial v^*_{\mathbf{k}\downarrow}}{\partial y} + u^*_{\mathbf{k}\downarrow}\frac{\partial u_{\mathbf{k}\uparrow}}{\partial y} + v_{\mathbf{k}\downarrow}\frac{\partial v^*_{\mathbf{k}\uparrow}}{\partial y}\right)\right]$$
$$S_y = \frac{\mu_B}{m}\mathrm{Re}\left[\sum_n\left(-v_{n\uparrow}\frac{\partial v^*_{n\downarrow}}{\partial y} + v_{n\downarrow}\frac{\partial v^*_{n\uparrow}}{\partial y}\right)\right. \tag{4.9b}$$
$$\left. + \sum_{\epsilon_\mathbf{k}<eV}\left(u^*_{\mathbf{k}\uparrow}\frac{\partial u_{\mathbf{k}\downarrow}}{\partial y} + v_{\mathbf{k}\uparrow}\frac{\partial v^*_{\mathbf{k}\downarrow}}{\partial y} - u^*_{\mathbf{k}\downarrow}\frac{\partial u_{\mathbf{k}\uparrow}}{\partial y} - v_{\mathbf{k}\downarrow}\frac{\partial v^*_{\mathbf{k}\uparrow}}{\partial y}\right)\right]$$
$$S_z = \frac{-\mu_B}{m}\mathrm{Im}\left[\sum_n\left(v_{n\uparrow}\frac{\partial v^*_{n\uparrow}}{\partial y} - v_{n\downarrow}\frac{\partial v^*_{n\downarrow}}{\partial y}\right)\right. \tag{4.9c}$$
$$\left. + \sum_{\epsilon_\mathbf{k}<eV}\left(u^*_{\mathbf{k}\uparrow}\frac{\partial u_{\mathbf{k}\uparrow}}{\partial y} - v_{\mathbf{k}\uparrow}\frac{\partial v^*_{\mathbf{k}\uparrow}}{\partial y} - u^*_{\mathbf{k}\downarrow}\frac{\partial u_{\mathbf{k}\downarrow}}{\partial y} + v_{\mathbf{k}\downarrow}\frac{\partial v^*_{\mathbf{k}\downarrow}}{\partial y}\right)\right],$$

where again the first terms on the right side are the spin current density at zero bias, and the second terms the contribution from the applied bias. This calculation is independent of that of the local magnetization. Thus we can verify the relation between the STT and the spin current in Eq. (4.7), as has previously been pointed out in Sec. 2.2.5.

4.2.3 Transfer Matrix Method and Spin Transport

Here, we give a brief summary of our spin transport calculation methodology. An extensive explanation has been given in Ref. [41] and in Sec. 2.2.2. We review these methods primarily because they focused on charge transport, and it is useful to clarify how they extend to spin transport, which requires some extra care due to the spatial

dependence of the spin transport quantities.

The procedure to calculate the conductance $G(V)$ involved merely evaluating the reflection and transmission amplitudes governed by the continuity of the wavefunction and discontinuity of its derivatives. This has to be done at each interface for both particles and holes, and for each spin, i.e. including both ordinary and Andreev reflection, as one would do in elementary quantum mechanics. In the S electrode, the procedure is to divide it into arbitrarily thin layers, in each of which the y-dependent self-consistent pair potential, as previously determined numerically, can be replaced by a constant.

In the expressions for the local magnetization Eq. (4.8) and the spin current Eq. (4.9) we have two terms in the right sides. The first is the equilibrium result, and can be calculated straightforwardly by the methods of Section 4.2.1. The more important terms are, of course, the bias driven contributions. To evaluate those we have to rebuild the wavefunctions (see Eqs. 2.3, 2.4, 2.6, and 2.9) so that they correspond to the proper boundary conditions of injected spin up or spin down particles. The method is in essence nothing but the elementary quantum mechanical procedure of building plane wave solutions out of stationary state wavefunctions, but it is mathematically much more complicated. The procedure is as fully described in Ref. [41] except for the presence of the N layer, which can be included by a trivial extension of either an F layer with h taken to be zero, or an S layer with $\Delta = 0$, as we do in Sec. 2.2. The transfer matrix method simply transcribes the continuity conditions for each amplitude, and the discontinuity in the derivatives arising from the delta function interfacial scattering, to each adjacent layer. From these rebuilt wavefunctions the second terms in the right sides of the expressions for $\mathbf{m}(y)$ and $\mathbf{S}(y)$ are straightforwardly calculated by adding the appropriate contributions as described in Sec. 2.2.2 This procedure is especially important in spin transport calculations, as the quantities involved depend on position and the simple BTK [50] procedure that one employs for the conductance does not apply.

4.3 Results

4.3.1 General

We report on the spin transport quantities, specifically the spin current, the spin transfer torque, and the bias-dependent portion of the magnetization, which as mentioned above is a measure of the spin accumulation (see Sec. 4.2.2). Each of these quantities depends on the applied bias voltage V, which we normalize to $E \equiv eV/\Delta_0$, where Δ_0 is the bulk value of the pair potential in bulk S material. These quantities depend also on the position y within the sample. All lengths are normalized by k_{FS}, and normalized lengths are denoted by the corresponding capital letter, e.g. $Y \equiv k_{FS}y$. All energies except for the bias are normalized to the Fermi energy in S. The magnetization components m_i are normalized by $-\mu_B(N_\uparrow + N_\downarrow)$, and, correspondingly, the spin current S_i is normalized [41] by $-\mu_B(N_\uparrow + N_\downarrow)E_{FS}/k_{FS}$. The normalization of the scattering strength parameters has been introduced above: values in excess of unity correspond to a tunneling limit situation. We will assume that the two ferromagnetic materials are the same, and hence take the field strengths $h_1 = h_2 = h$ to be equal. We will use the value $h = 0.145$ in our dimensionless units. This value was shown to be appropriate to describe the transition temperature [9] of similar samples in which Co was the ferromagnetic material. Similarly, we will assume that the scattering strengths for the two N/F interfaces are the same $H_{B1} = H_{B2} \equiv H_B$. We will take the effective coherence length of the superconducting order parameter to be $\Xi_0 = 115$ which was found to be appropriate for samples in which the S layer was niobium [9]. We set the superconducting layer thickness to be $D_S = 180$, which is large enough compared to Ξ_0 to allow for superconductivity, but not so large that the proximity effect is negligible within the superconductor. This has been shown in Chapters 2 to provide a more prominent critical bias feature in charge transport due to the variation in the pair potential $\Delta(y)$. For the same reason, we also take the low temperature limit $T \to 0$ in our calculations. We will also fix the thickness of the outer ferromagnet to $D_{F1} = 30$ as we have found that the results are less sensitive to this parameter. We will consider variations of D_N and D_{F2}. We have assumed that any band mismatch parameters are unity. Although this is not generally true in real systems, in practice the effects of such a mismatch can be incorporated into the effective value of the scattering strength parameter when

interpreting and fitting data. This fitting procedure was shown to correctly predict the thermodynamic properties in similar [9] spin valve systems.

Below, we will be showing results for six different sets of the parameters D_{F2}, D_N, H_B, and H_{B3}. For each set of parameters we will examine the following vector quantities: the spin current, the analog of the spin accumulation $\delta\mathbf{m}(V)$, the spatially averaged spin accumulation in S and N, and the spatially averaged STT in both F layers. For the first two, we will examine each component at low-bias, $E = 0.6$, and at high-bias values, $E = 2$. We will study the quantities $\delta m_i \equiv m_i(V) - m_i(0)$ and τ_i as a function of the bias, rather than of position, by averaging these quantities over a layer. Thus, for example $\langle\tau_i\rangle \equiv 1/D_\ell \int dY \tau_i(Y)$ where the integral is over the relevant layer, of thickness D_ℓ. In all cases we plot the results for several values of the mismatch angle ϕ. The number of quantities involved for each set of physical parameters is excessively large, therefore we focus on only the most remarkable features and angular dependencies, and on their distinctive behavior as a function of the physical parameters.

4.3.2 Ideal Interfaces

In Fig. 4.1 we show the results for a physical parameter set with ideal interfaces (zero interfacial scattering). The layer thicknesses for the $F_1/N/F_2/S$ layers are 30/40/25/180 respectively. This case can be compared with previous results obtained in Sec. 2.3.4 in the absence of the normal metal layer N. The normal layer greatly reduces the STT at the interfaces between the ferromagnets. We start by examining the fundamental features of each quantity mentioned, as a baseline for comparison with subsequent figures. The set of panels labeled (a) show the components of the spin current as a function of position, and the set labeled (b) the spin accumulation, also as a function of position. Sets (c) and (d) refer to the spatially averaged spin accumulation and STT respectively, as functions of bias.

In Fig. 4.1a, we examine the spin current components S_i (top to bottom) as a function of position Y at low to high bias ($E = 0.6$, left and $E = 2$, right). The position of the interfaces is indicated by vertical lines. The origin is taken at the F_2/S interface. Only a small part of the S layer is shown, as the behavior of $\mathbf{S}$ is constant in S beyond the region included. In each panel, we plot the results for seven values of the angle ϕ, as indicated by the key in the upper right panel of Fig. 4.1d. In each case we see that

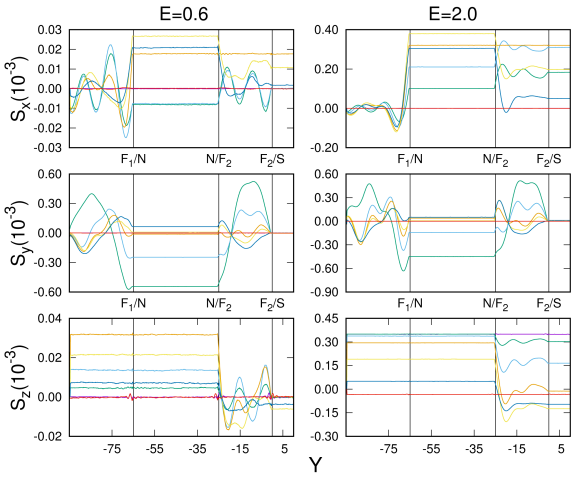

(a) Local Spin Current

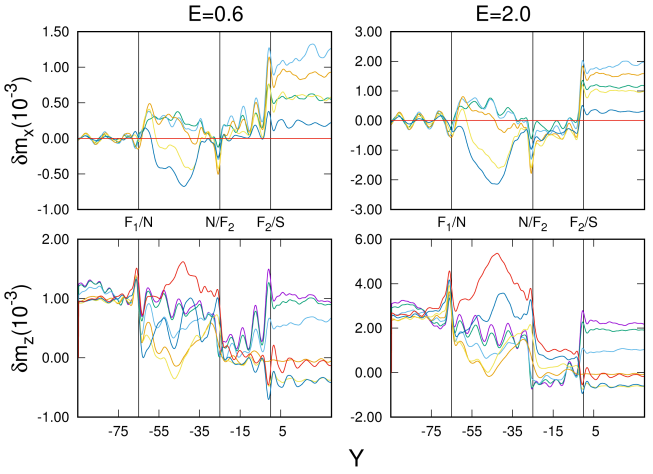

(b) Local Spin Accumulation

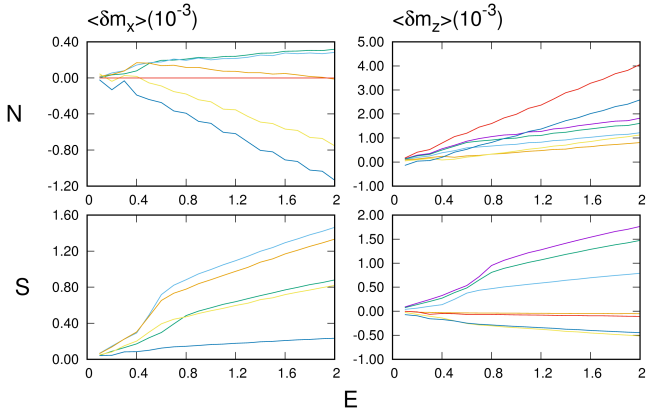

(c) Spatially Averaged Local Spin Accumulation

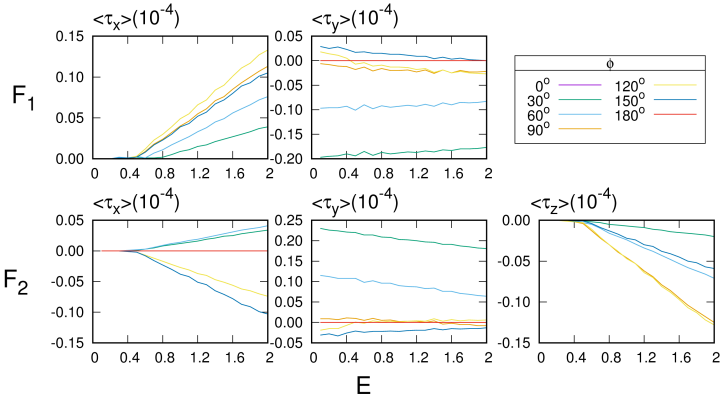

(d) Spatially Averaged Spin Torque

Figure 4.1: Results for ideal interfaces. The layer thicknesses for the $F_1/N/F_2/S$ layers are 30/40/25/180 respectively, and the interfacial barriers H_B and H_{B3} are both zero. The key for the angular dependence is in the upper right panel of set (d). See text for details.

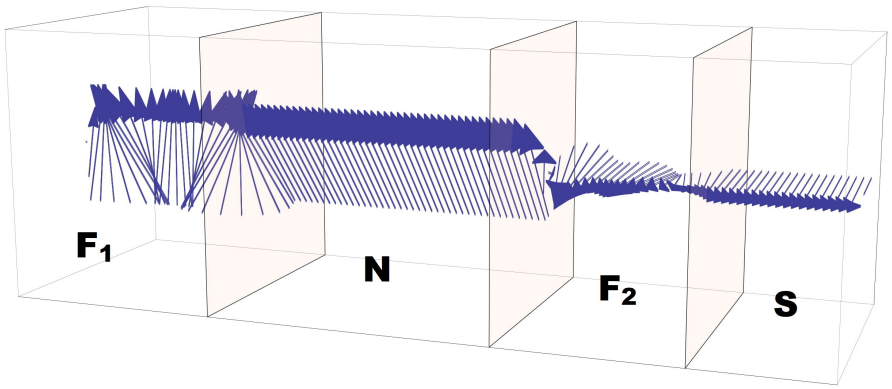

Figure 4.2: A 3D representation of the spin current from Fig. 4.1a at $\phi = 90°$ and $E = 2.0$. From left to right, the boxes comprise the layers $F_1/N/F_2/S$ respectively. The spin current precesses about the exchange field in F, while also dampening in F_2. The orientation of the field in S is rotated to 90° from the z axis.

the spin currents at $\phi = 0$ and $\phi = 180°$ are constant, as there are no spin torques when $\mathbf{h_1}$ and $\mathbf{h_2}$ are collinear. Furthermore, S_x for $\phi = 90°$ is constant in F_2 since $\mathbf{h_2}$ in this case is along the x-axis. Similarly S_z is constant for all ϕ in F_1 since, with our choice of coordinates, $\mathbf{h_1}$ is along the z-axis. As the bias increases, the magnitude of the spin current increases, except for the y-component, normal to the layers, which is nearly bias independent. This is because S_y is driven primarily by the static spin torque that exists near the boundary of the ferromagnetic layers: this torque is entirely in the y-direction. We see that $S_y = 0$ for all ϕ and all biases within the S layer. This is possibly because the excess current in S is due to triplets, and there are none formed in the y direction. On the other hand, the S_x and S_z components within the superconductor become nonzero at high bias for all angles ϕ.

These nonzero spin currents, in S, occur when the applied bias is greater than the critical bias (CB). This bias corresponds to a value smaller than Δ_0: it represents the effective gap energy that the superconductor provides near the interface due to the singlet correlations. The singlet pair amplitudes have previously been shown to be angularly dependent, and the changes in these amplitudes were shown to correspond with the change in critical temperature (see e.g. Ref. [48] Figures 2 and 3). The reduction or increase in the CB directly correlates to the corresponding change in the

singlet amplitudes and thus has a nonmonotonic dependence on ϕ. This dependence of the CB is due to the proximity effect between the F_2 and S layers. The angular dependence comes from the formation of triplet pairs where there is angular mismatch in the system. In this case, with perfect interfaces, the angular dependence of the CB is large, confirming previous results for the charge current [67]. It can be observed that at $E = 0.6$, the critical bias values for each angle are sometimes above and sometimes below that value of E. For angles such that the CB is greater than the bias ($E = 0.6$ in this case), the spin current is zero in the superconductor. However, when the CB is lower than the applied bias, the excitations have energy greater than the effective gap energy and at those angles we find non-zero spin current in S.

By viewing the spin current in 3D, we can get a better grasp of its overall orientation within the multilayer. In Fig. 4.2, in the high bias limit and at $\phi = 90°$, we see that the spin current rotates in the x-z plane from near the z direction in F_1 to an angle close to the mismatch angle ϕ in F_2 and S. In the ferromagnetic layers, we see the spin current precessing about the exchange fields $\mathbf{h_1}$ and $\mathbf{h_2}$ in F_1 and F_2 respectively. The precession in F_2, however, is damped due to the proximity effect of the superconductor, the current becoming constant at the F_2/S boundary. The spin current in the normal metal layer is also constant, since there are no torques there. The orientation of the spin current in N is rotated in the x-z plane to an angle between 0 and ϕ, with a nonzero y-component that is due to the net STT in both ferromagnetic layers.

In Fig. 4.1b we examine the x and z components of $\delta\mathbf{m}$ for low to high biases (left to right) as functions of Y. The y-component is several orders of magnitude smaller and we do not show it. The component δm_x is zero for $\phi = 0$ and $\phi = 180°$. δm_z is nonzero and only weakly ϕ dependent in F_1, whereas δm_x is oscillatory and small in this region. Furthermore, δm_z and δm_x are nonzero and nearly constant with position in the S region at large bias. In general the magnitude of the spin accumulation $\delta\mathbf{m}(V)$ is oscillatory everywhere at low biases, but with small amplitudes. It oscillates in N and irregularly rotates in the x-z plane, particularly for mismatch angles near $\phi = 90°$. The overall magnitude increases with bias with very little change in the angular dependence. The spin accumulation vector tends to align with $\mathbf{h_2}$ within the superconductor: this is similar to the spin current behavior. The magnitude of $\delta\mathbf{m}$ also decreases, in all layers, as ϕ increases from 0 to 180°.

In Fig. 4.1c we examine the spatial average (as defined earlier in this section) of $\delta\mathbf{m}(V)$ in the N and S layers (upper and lower plots, respectively), as a function of bias. In both regions, $\langle \delta m_x \rangle$ vanishes for $\phi = 0$ and $\phi = 180°$. In S we can see a critical bias behavior in $\langle \delta m_x \rangle$, at which value the magnitude begins to rise quickly with bias, becoming approximately linear. In both regions each component is nonmonotonic in ϕ. In S, $\langle \delta m_x \rangle$ is maximized between $\phi = 60°$ and $\phi = 90°$ while in N it is most negative at $\phi = 150°$, $\langle \delta m_z \rangle$ features a similar, but less dramatic critical bias feature only in S, with this component decreasing for angles $\phi > 90°$.

In Fig. 4.1d we consider the average spin transfer torques as a function of E, as just done with the average spin accumulation. We do so only in the ferromagnetic regions where the torques are nonzero. The component τ_z is zero in the outer ferromagnetic region F_1, since the field $\mathbf{h_1}$ is along the z direction, and it is not plotted: the angular key for the entire figure is shown instead. The torque τ is always zero for $\phi = 0$ and $\phi = 180°$, and $\tau_x = 0$ for $\phi = 90°$ in F_2: this follows from our geometry. We see a strong critical bias feature in the x component in both F_1 and F_2, and also in the z components in F_2: the averaged torque is zero below the CB, and then grows linearly with increasing bias. The x component in F_1, and the z component in F_2 show similar behavior, with a steady increase or decrease in value respectively for all angles, and a maximum magnitude between $\phi = 90°$ and $\phi = 120°$. $\langle \tau_x \rangle$ in F_2 is different: it increases with E for angles $\phi < 90°$ and decreases for angles $\phi > 90°$. $\langle \tau_y \rangle$ has very different behavior from both of the other components: it is nonzero at zero bias due to the static ferromagnetic proximity effect. Because of this, $\langle \tau_y \rangle$ is nearly independent of bias, slightly decreasing in magnitude in both ferromagnetic regions. It follows from Eq. 4.7 in the steady state that the net change in spin current in N and S is directly proportional to the average torque. Indeed, the constant S_y in the normal metal can be described by the net average torque τ_y in both ferromagnetic regions.

In this subsection we have analyzed the spin current and spin accumulation for the ideal interface case. Although such perfect samples can not be fabricated, much that is learned in this simple case can be applied to more realistic systems. A good part of the discussion for Fig. 4.1 will apply to the results for other physical parameter values presented below. We have seen that in the high bias limit the spin current precesses in the F layers about the respective internal exchange fields $\mathbf{h_i}$, while being a constant

in N and S with an orientation determined by that of the neighboring exchange fields of the ferromagnets. We also see that the in-plane components of the spin current (S_x and S_z in our coordinate system) are bias dependent, and the plane-perpendicular component (S_y) is bias independent. The latter is due to the proximity effect between the two ferromagnetic layers, which produces a torque solely in the y direction without an applied bias. More remarkable is the bias dependence in the x and z components of the spatially averaged spin torque, which shows a critical bias behavior of its own. Above the CB value, the magnitude of the torque and the spin current increases linearly, while below there is no bias dependence. This is similar to the charge current behavior in the tunneling limit. Consistent with this, there is no penetration of the spin current within the superconductor below this CB. The spin accumulation behaves similarly to the spin current, but is not constant in magnitude in N or S, nor in orientation within N, and the overall behavior is highly oscillatory. The spatially averaged local $\delta\mathbf{m}(V)$ also features a CB feature, separately from that of the torque. For this ideal case, the bias feature is less pronounced than in the non-ideal case (see below), but a clear transition can be seen in the quasi-linear bias trends below and above the bias thresholds that are not obviously related to those of the spin current features.

4.3.3 Interfacial Scattering

We now turn on the effect of interfacial scattering. First we consider, in Fig. 4.3, the case where only a barrier at the F_2/S interface exists, with a qualitatively large scattering parameter value $H_{B3} = 0.9$. The layer thicknesses are as in the previous figure. When the scattering is large at this interface, the superconducting proximity effect is reduced. We compare this case to the zero scattering limit of Fig. 4.1 in order to examine closely how the basic features of the proximity effect influence the spin currents. The organization of the panels in Fig. 4.3 is the same as in Fig. 4.1.

In Fig. 4.3a we see that the x and z components of the spin current are now driven to zero, within numerical precision, at low bias. This is due to the increase in the CB due to the barrier, which weakens the proximity effect and thereby makes it more difficult for the Cooper pairs to propagate out of the superconductor and convert to long ranged triplets. The y component, however, is still nonzero due to the static spin torques from the ferromagnetic proximity effect. Unlike in the other cases discussed, S_y

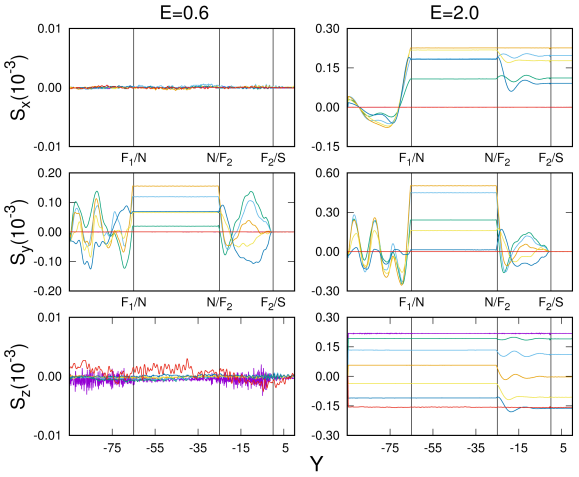

(a) Local Spin Current

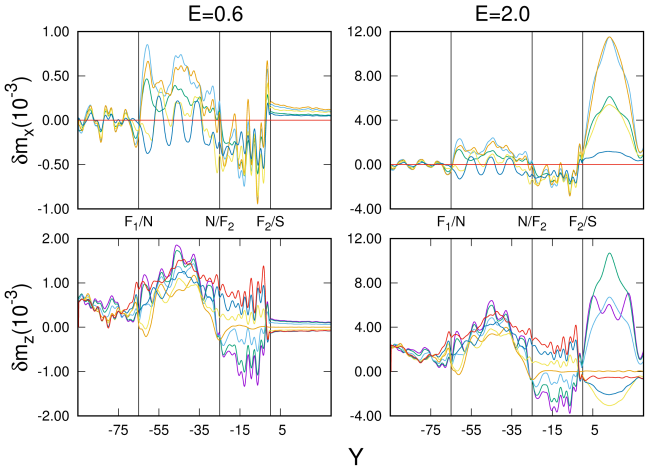

(b) Local Spin Accumulation

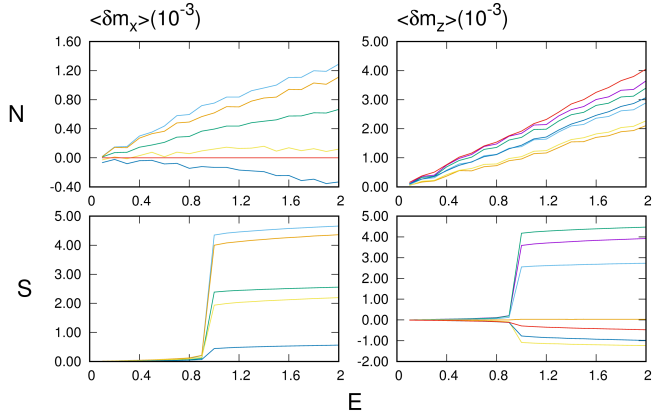

(c) Spatially Averaged Local Spin Accumulation

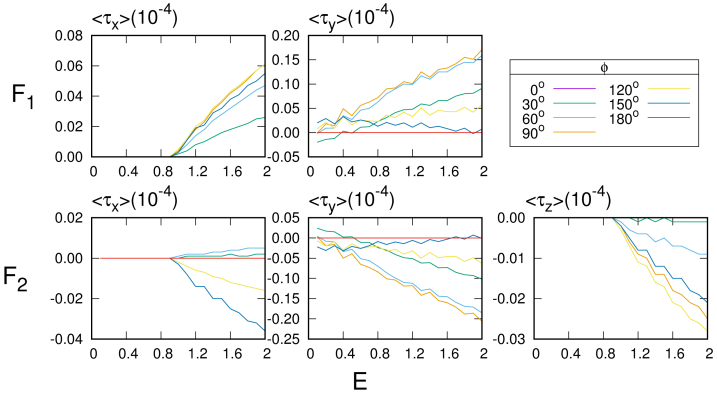

(d) Spatially Averaged Spin Torque

Figure 4.3: Results for a nonzero tunneling barrier at the F_2/S interface. The layer thicknesses are as in Fig. 4.1 and the interfacial barriers are $H_B = 0$ and $H_{B3} = 0.9$. See text for details.

now increases significantly at higher biases, although not as dramatically as the other two components. In the high bias regime, the system returns to precessing about $\mathbf{h}$ in the ferromagnetic regions. $\mathbf{S}$ is also rotated about the x-z plane, this time closer to the second ferromagnetic field $\mathbf{h_2}$ which is oriented at an angle ϕ. The overall magnitude of the spin current is of course reduced by the barrier.

In Fig. 4.3b we see that the spin accumulation is significantly decreased in magnitude within the superconductor at the low bias limit. The magnitude increases dramatically in S at high bias, although it remains smaller than for perfect interfaces. Furthermore, we see that the magnitude of $\delta\mathbf{m}$ is highly oscillatory in the superconductor. The orientation remains fixed to that of the exchange field $\mathbf{h_2}$. In the normal metal, the spin accumulation rotates counterclockwise within the x-z plane for $\phi < 90^\circ$ and then reverses direction to become aligned with the z axis again for $\phi = 180^\circ$. The rotation in the x-z plane is uniform throughout the N layer in the high bias case, but not for low bias values. In the spatially averaged results of Fig. 4.3c we note a remarkable feature in the superconducting layer: a dramatic, sharp increase in the magnitude of $\langle\delta\mathbf{m}\rangle$ at the critical bias, after which the magnitude grows at a much slower rate. The angular dependence remains approximately the same as in Fig. 4.1c. The low bias spin accumulation is heavily impeded by the high barrier. In Fig. 4.3d we show that the average STT exhibits the same critical bias features as in Fig. 4.1d. However, the high barrier causes the critical bias to increase and to become nearly ϕ independent. Its value is seen to be $E \approx 0.85$ in the results for $\langle\tau_x\rangle$ (in both F_1 and F_2) and for $\langle\tau_z\rangle$ in F_2. Furthermore, $\langle\tau_x\rangle$ in F_2 shifts to become almost entirely negative. The y component is changed dramatically by the barrier: $\langle\tau_y\rangle$ steadily increases in magnitude with increased bias for all angles except $\phi = 150^\circ$. The static spin torque is heavily reduced by the introduction of a large barrier between F and S, which increases the pair potential at the interface.

In Fig. 4.4 we turn to the converse case where the scattering potentials at both of the F/N interfaces are nonzero, while the F_2/S barrier is ideal, thereby complementing the study in the previous figure. The layer thicknesses are again 30/40/25/180. For the interfacial barriers we take $H_B = 0.5$ (a value not so high as to be in the tunneling limit) and $H_{B3} = 0$. Thus, there is a full proximity effect between S and F_2. We now are interested in how the scattering within the spin valve structure affects the spin

transport. Perhaps unsurprisingly, the introduction of these barriers turns out to be very important, as the spin-valve effect, which determines much of the spin-transport features, is quite sensitive to these scattering potentials.

In Fig. 4.4a we see that the spin current is nonzero in the N region at low bias, as in the zero barrier case. S_y in N is now almost entirely bias independent and its angular dependence is symmetric about $\phi = 90°$, positive for $\phi > 90°$ and negative for $\phi < 90°$. Similarly, the ϕ dependence of S_x at low bias is nearly symmetrical with respect to ϕ in all layers. At high bias, we again see that the x and z components of the spin current increase, penetrating the superconductor. Due to the significant interfacial scattering, the overall magnitude decreases from the zero barrier case, especially for the x and z components.

In Fig. 4.4b we see that, in comparison to the corresponding perfect interface case of Fig. 4.1b, the angular dependence is decreased in the normal metal layer, with more oscillations in δm_x about the zero value and a peak forming in δm_z in both the low and high bias cases. In Fig. 4.4c we see that the average spin accumulation in S has an angular dependence and critical bias features similar to those found in the zero barrier case, but with decreased magnitude. An exception is for the x component at $\phi = 150°$, which is significantly larger. In the normal metal, $\langle \delta m_x \rangle$ increases up to a ϕ dependent CB, then steadily decreases for increasing bias. $\langle \delta m_z \rangle$ monotonically increases with bias, and has a greater magnitude than $\langle \delta m_x \rangle$.

In Fig. 4.4d we see significant differences in the behavior of the average STT, as compared to the single high barrier case of Fig. 4.3d. $\langle \tau_x \rangle$ in F_1 no longer features a CB behavior: it is nearly constant with E. In both ferromagnets, $\langle \tau_y \rangle$ is again only weakly dependent on bias, with a slight increase in the F_1 layer and a decrease in the F_2 layer. The overall magnitude is significantly smaller, in all layers and for all components, than in the zero barrier case. In F_2, we see a remarkable symmetry emerge in the angular dependence of the averaged τ_x and τ_z. For $\langle \tau_x \rangle$, the values for $\phi = 30°$ and $\phi = 60°$ are both increasing and positive, while those for $\phi = 120°$ and $\phi = 150°$ are decreasing by an equivalent amount. Similarly, for $\langle \tau_z \rangle$, we see an equivalent decrease in value with increasing bias for supplementary angles ($\phi = 30°, 150°$ and $\phi = 60°, 120°$).

In Fig. 4.5 we finally examine the experimentally relevant situation where there are scattering barriers at all interfaces. Thus, in addition to the two interfacial scattering

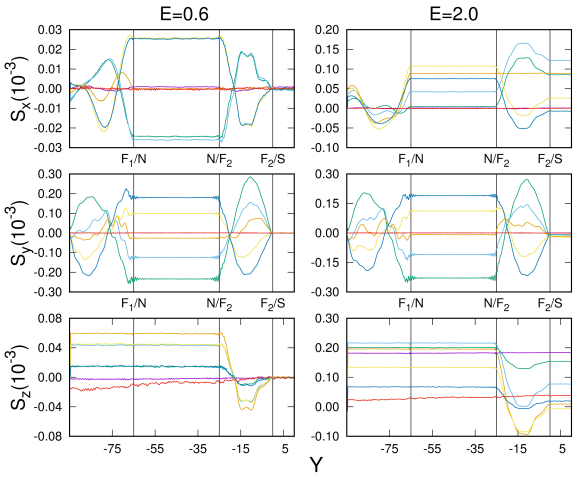

(a) Local Spin Current

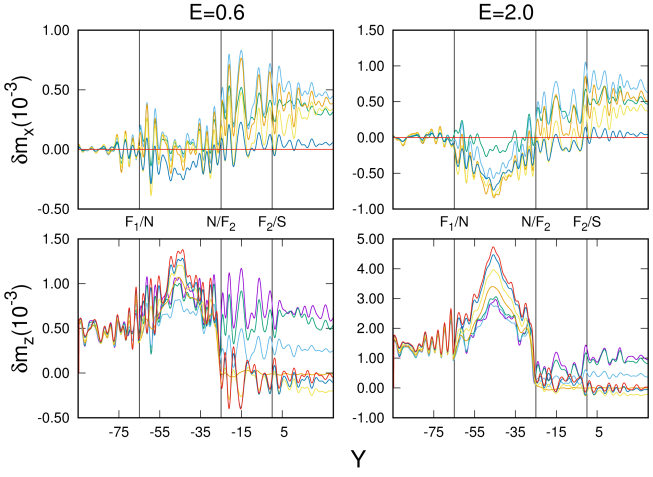

(b) Local Spin Accumulation

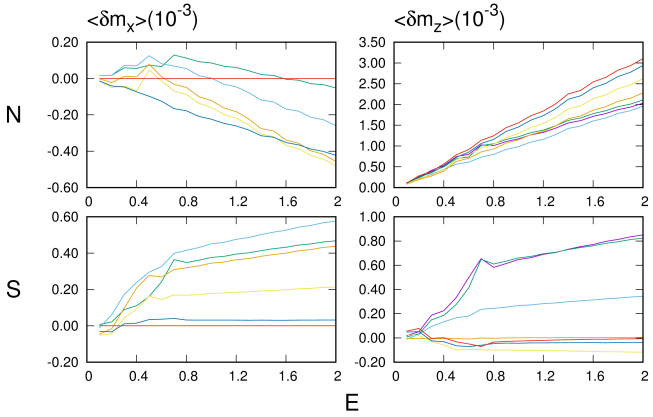

(c) Spatially Averaged Local Spin Accumulation

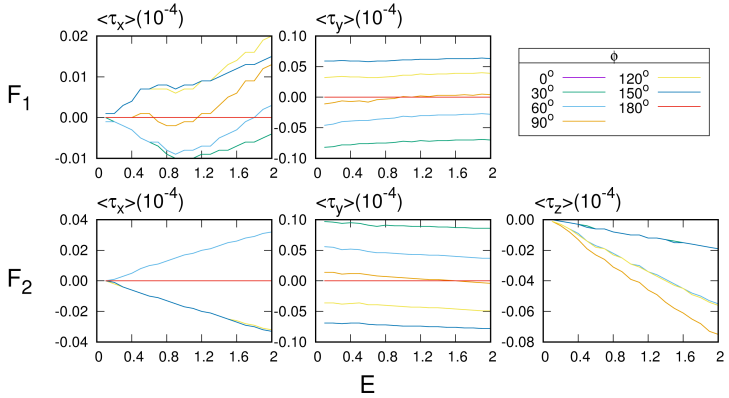

(d) Spatially Averaged Spin Torque

Figure 4.4: Results for nonzero barriers in the F_1/N and N/F_2 interfaces. The layer thicknesses are as in Figs. 4.1 and 4.3. The interfacial barriers are $H_B = 0.5$ and $H_{B3} = 0$. See text for details.

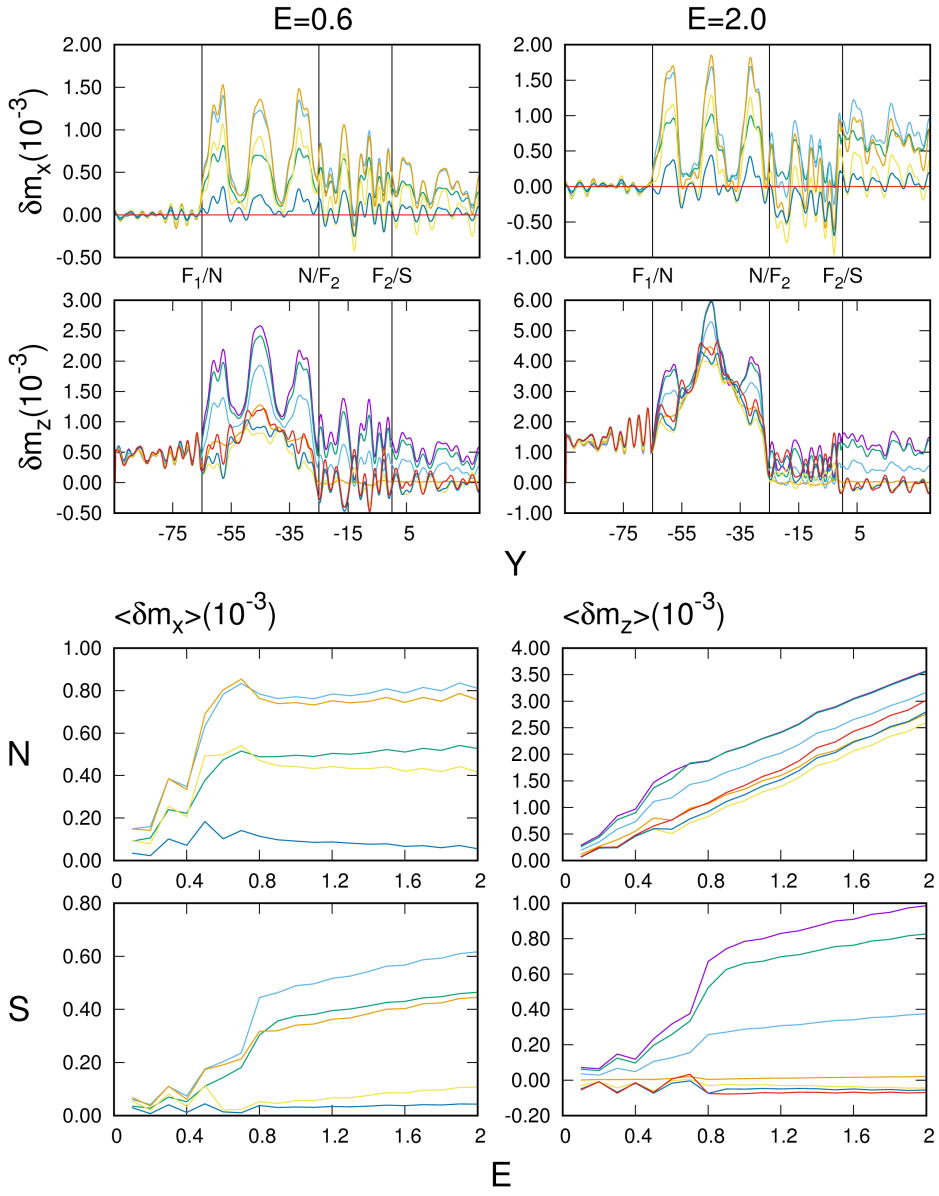

Figure 4.5: Results with nonzero interfacial barriers at all interfaces. The layer thicknesses are as in the previous figures, and the interfacial barriers are $H_B = 0.5$ and $H_{B3} = 0.3$. The top four panels are the local spin accumulation, and the bottom four panels are the spatially averaged spin accumulation. The color key for the angular dependence is as in Fig. 4.1d. See text for details.

barriers with $H_B = 0.5$ in Fig. 4.4 we include an additional scattering barrier at the F_2/S interface, with $H_{B3} = 0.3$. Although it is reasonable to assume that efforts will be made to minimize the scattering at this interface, unavoidable experimental limitations and wavevector mismatch (as mentioned above) imply that one can never assume that any barrier will perfectly vanish. The layer thicknesses are as in the previous figures. The organization of this figure is simplified, when compared to the previous ones. The local spin current is not shown in Fig. 4.5 because it is very similar to that in Fig. 4.4a. We see then that the introduction of a third barrier of intermediate size at the F_2/S interface does not significantly affect the spin current. The spin transfer torques also remain unaffected: this is because the proximity effect is not seriously inhibited by this additional barrier, and the spin-valve effect dominates the spin transport, in these cases. Hence, the sets of panels corresponding to (a) and (d) in the previous figures are omitted, and we focus in this figure on the spin accumulation and its spatial average, panels (b) and (c) in the previous figures, now in the top four and bottom four panels respectively. The color key for the ϕ dependence is as indicated in Figs. 4.1d and 4.3d.

In the top panels we see that $\delta\mathbf{m}$ in the normal metal layer departs significantly from what we found in Fig. 4.4b at $H_{B3} = 0$. In δm_z we observe a transition from the single peak result seen in Fig. 4.4b to a triple peak structure particularly prominent for $\phi < 90°$. The x component also forms three peaks at low and high biases in N, at all angles. As in the previous cases, $\delta\mathbf{m}$ is rotated in the x-z plane in N. However, these rotations are non-uniform, and strongly non sinusoidal, with the troughs aligning with the z axis while the peaks align at an angle less than the mismatch angle ϕ.

In the bottom panels we see, in $\langle\tau_i\rangle$ an enhancement in the critical bias feature in S seen in Fig. 4.4c, There is a steep growth in the magnitude of $\delta\mathbf{m}$, averaged in S, at the critical bias. In the normal metal, we see a behavior for $\langle\delta m_z\rangle$ similar to that in Fig. 4.4c but with a remarkably different angular dependence. For $\langle\delta m_x\rangle$ in N we see a very different high bias behavior, where $\langle\delta m_x\rangle$ increases dramatically at the critical bias and then abruptly levels off to a flat or slightly decreasing bias dependence. The behavior in the average δm_x in N is now much more similar to that of δm_x or δm_z in S.

The dependence of the spin current and $\delta\mathbf{m}(V)$ on interface quality, which we have considered in this subsection, is particularly important, not only because ideal interfaces

are not possible, but also because interfacial quality cannot be perfectly replicated between samples. Therefore, understanding this dependence is vital to explain differences in measured quantities of similarly constructed samples. We started with a tunneling barrier between the F and S layer, which produced results that differ greatly from the more ballistic, low barrier cases, both for the spin current and the spin accumulation. We find a stronger critical bias behavior in the spin current and torque, where the CB moves to unity in our units. This is because of the weakening of the proximity effects in the tunneling limit. The spin current is strongly driven to zero for bias values below the CB. The spin accumulation in the S region is similarly driven low below this value, but no such strong CB feature is seen in the local $\delta\mathbf{m}(V)$ within the normal metal. The behavior in the tunneling limit directly contrasts with that found for the intermediate barrier strengths of the next two cases (barriers $H_B = 0.5$, $H_{B3} = 0$ and $H_B = 0.5$, $H_{B3} = 0.3$ respectively) whose spin current features are similar to each other. We see a vanishing CB effect in the magnitude of the spin current and torque in F, possibly due to resonance effects in the intermediate barriers. However, we do still see a CB effect in the penetration of the spin current into the superconductor, as found for the ideal barrier case. In both cases, we also see a prominent, although weaker, critical bias effect in the local $\delta\mathbf{m}(V)$ in the S layer. However, we also see a CB effect in the normal metal, absent in the tunneling case. The behavior of the local spin accumulation in N depends on the value of H_{B3}. There is a regular oscillatory pattern in $\delta\mathbf{m}(V)$ for nonzero H_{B3} that results in three peaks that have a regular rotation in orientation within the normal metal. This leads us to conclude that the critical bias behavior of the spin accumulation in N is distinguishable from that of the spin current. We also see a completely new phenomenon in the oscillatory local spin accumulation that is bias independent and solely dependent on the physical parameters of the system.

4.3.4 Dependence on Layer Thickness

In the next two figures, Fig. 4.6 and Fig. 4.7, we consider the dependence of the results on geometry, i.e. on layer thickness. The scattering barriers are all nonzero and have the same values as in Fig. 4.5, namely $H_B = 0.5$ and $H_{B3} = 0.3$, but we now vary the intermediate layer thicknesses of the normal metal, D_N (Fig. 4.6), and then that of the the inner ferromagnet, D_{F2} (Fig. 4.7). The layer thicknesses of the F_1 and S layers

remain $D_{F1} = 30$ and $D_S = 180$ in both figures. In Fig. 4.6 we increase the normal metal layer spacing from the previous value $D_N = 40$ to $D_N = 60$, leaving $D_{F2} = 25$, while in Fig. 4.7 we decrease the inner ferromagnetic layer thickness from $D_{F2} = 25$ to $D_{F2} = 15$, while leaving $D_N = 40$. Geometric changes can strongly affect the transmission and reflection amplitudes, just as they do in elementary quantum mechanics problems such as that of transmission across two barriers, where the results can depend drastically on the separation between the two scattering centers. Here we examine how these rather minor changes in the geometry affect the spin-transport quantities. We have found little change in the spin current and spin torque when increasing D_N, thus in Fig. 4.6 we only include plots of the spin accumulation and its average, following the scheme of Fig. 4.5, in the top four and bottom four panels respectively. For Fig. 4.7, on the other hand, we include the results for spin current and torque components as we find nontrivial changes in the magnitude and orientation of the spin current, following then the organizational scheme of Figs 4.1, 4.3, and 4.4.

In the top panels of Fig. 4.6 we observe a three peak structure for the spin accumulation in N similar to that found in the top panels of Fig. 4.5, but with several distinctions. First, we see that δm_z has now fully transitioned to the three peak behavior for all ϕ and all biases. Also, the three peak behavior is inverted in δm_x. Indeed, $\delta\mathbf{m}$ makes a clockwise rotation in the x-z plane in N, contrary to both the spin current and spin accumulation behaviors we have seen thus far. The orientation in S remains unaffected. We also see a significant increase in the magnitude of $\delta\mathbf{m}$ in all layers for high biases, indicating greater growth in the spin accumulation. In the bottom panels we see a behavior in the average spin accumulation in S similar to that in the bottom panels of Fig. 4.5, with increases to the x component for angles $\phi = 30°$, $90°$, and $120°$. The behavior in N is significantly different from that found in the previous cases, where in the x component we now see no major critical bias behavior and a steadily decreasing bias dependence: this is now similar to the behavior of the magnitude of the z component. The z component has the usual steady increase with bias, but the angular dependence is now most similar to that in Fig. 4.4c. We see then that the angular dependence is very sensitive to both the layer thickness and the barriers.

For Fig. 4.7 we revert to the full set of plots used e.g. in Fig. 4.1, with the same internal organization. In Fig. 4.7a we see (when comparing with the results shown

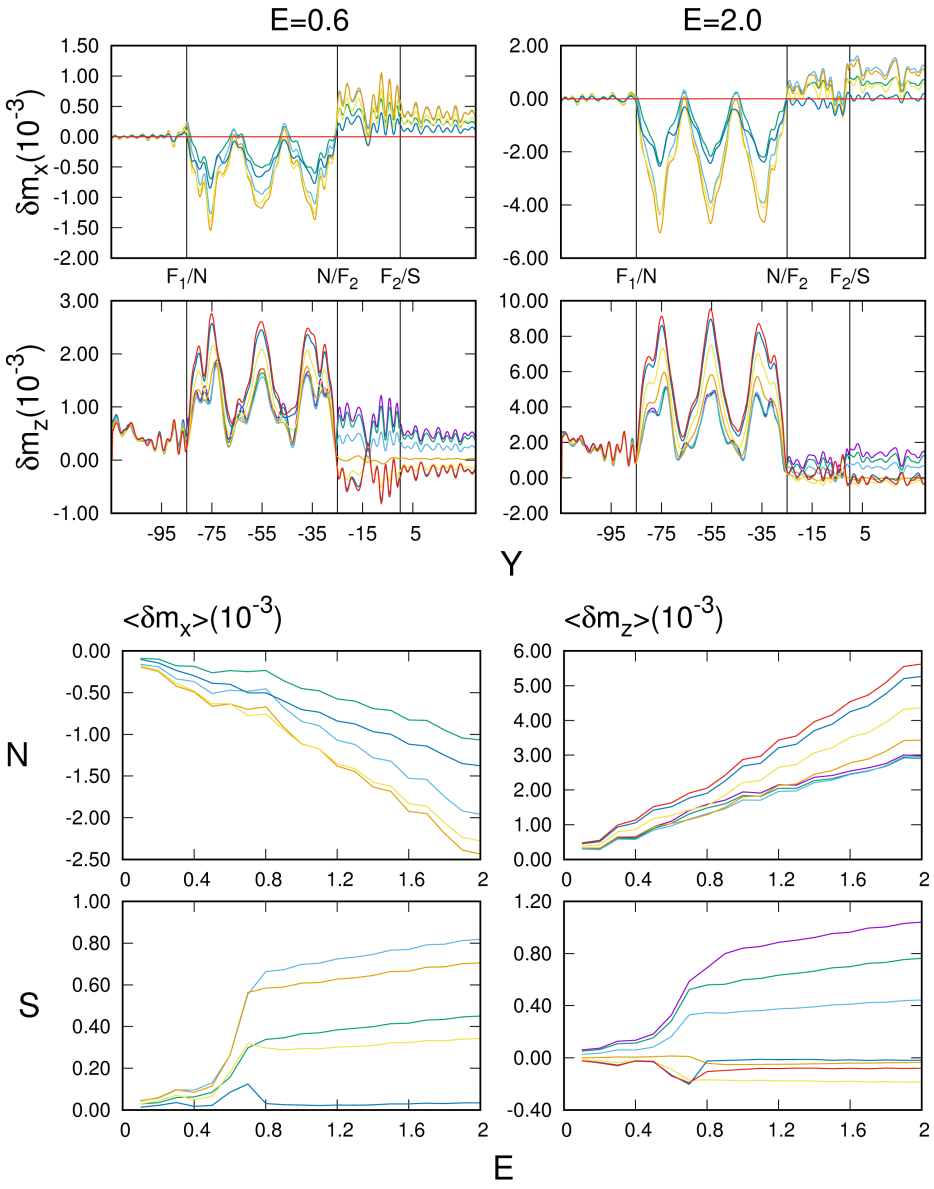

Figure 4.6: Results with an increased normal metal layer thickness, emphasizing the D_N dependence. The layer thicknesses for the $F_1/N/F_2/S$ layers are 30/60/25/180 respectively, and the interfacial barriers H_B and H_{B3} are 0.5 and 0.3 respectively. The top four panels are the local spin accumulation, and the bottom four panels are the spatially averaged spin accumulation. The color key for the ϕ dependence is as in e.g. Fig. 4.1d.

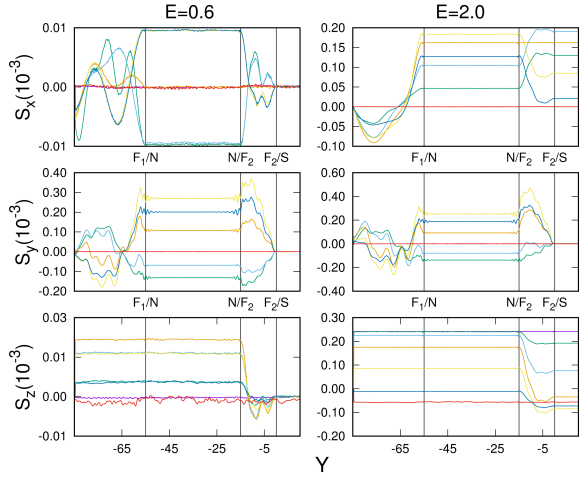

(a) Local Spin Current

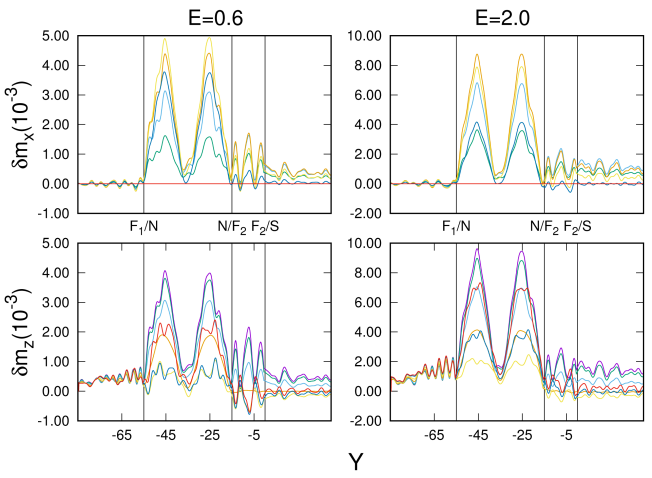

(b) Local Spin Accumulation

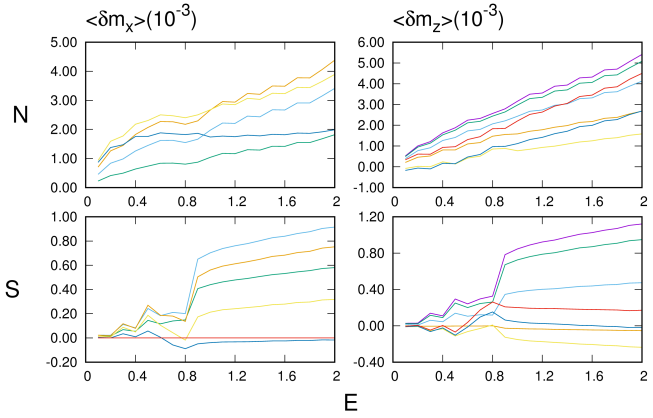

(c) Spatially Averaged Local Spin Accumulation

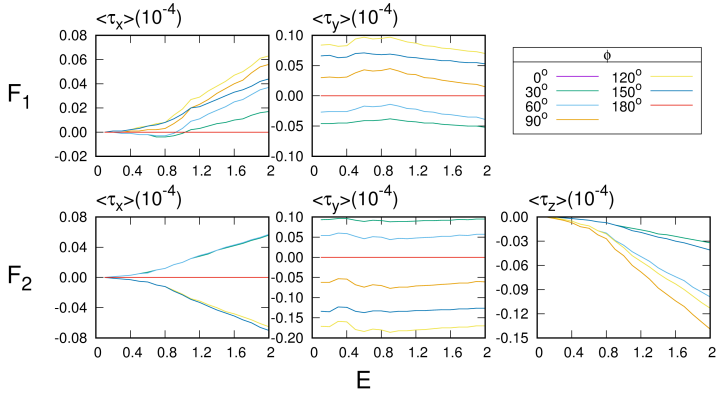

(d) Spatially Averaged Spin Torque

Figure 4.7: Results with a decreased intermediate ferromagnetic layer thickness, emphasizing the D_{F2} dependence. The $F_1/N/F_2/S$ layer thicknesses are 30/40/15/180 respectively, and the interfacial barriers are $H_B = 0.5$ and $H_{B3} = 0.3$.

in Fig. 4.4a which, as mentioned, are quite similar to those for the case shown in Fig. 4.5) that when decreasing the intermediate ferromagnetic layer spacing, the x and z components of the spin current decrease quite significantly in the low bias limit. On the other hand, they increase somewhat in the high bias limit, especially the S_x component. The orientation of $\mathbf{S}$ in the superconductor is now rotated closer to the negative z direction, much more significantly so for orientations with $\phi > 90°$. This feature is complemented by Fig. 4.7d, where the average spin torque is seen to increase its rate of growth. This may seem counter-intuitive at first, but it is important to note that the superconducting pair amplitudes are damped by the ferromagnetic layer.

In Fig. 4.7b we see, comparing now directly with Fig. 4.5, that decreasing D_{F2} changes the spin accumulation in N from a three-peak to a two-peak structure with the same angular dependence and greater magnitude. The peaks also show a greater rotation in orientation compared to those in Fig. 4.5, where the spin accumulation is more closely aligned to the orientation of $\mathbf{h_2}$ than before. The troughs of these oscillations are still oriented along the z axis. The overall magnitude of the spin accumulation also increases dramatically with bias, at a much greater rate than those in the systems discussed previously, as can be seen in Fig. 4.7c. However, $\langle \delta m_x \rangle$ in N steadily increases with bias, with a slight peak near the critical bias. The average spin accumulation at angle $\phi = 150°$ does not increase with bias, and remains an outlier.

In considering the geometry dependence in this subsection, we have focused on the thickness of the intermediate layers, as these tend to be the thinnest in actual systems and the impact of small deviations in the design and fabrication process needs to be understood. We have found in the previous two chapters that these layers have the greatest impact on charge transport. However, we see almost no dependence of the spin current on the normal metal layer thickness (see Figs. 4.5 to Fig. 4.6). This is likely due simply to this layer being nonmagnetic. The spin accumulation shows a similar critical bias behavior and a three-peak oscillating pattern in the normal metal layer, but with a curious distinction: the orientation, and in general the x component bias dependence, of the local $\delta\mathbf{m}(V)$ reverses direction, rotating $\delta\mathbf{m}$ clockwise in the x-z plane in N. This is in the opposite direction of the general rotation between the $\mathbf{h_1}$ and $\mathbf{h_2}$ exchange fields. We have not yet determined why this may happen and it warrants further study. We do find a strong dependence on the spin current on the intermediate

ferromagnetic layer thickness D_{F2}. By decreasing D_{F2}, we see a reemergence of the CB effect in the spatially averaged torque, as well as greater growth of the spin current magnitude with bias. We also see a dramatic change in the spin accumulation in N, where from Fig. 4.5 to Fig. 4.7 changes in the oscillation of the local spin accumulation occur, resulting in only two-peaks. Between these figures D_N does not change, nor does the value of the exchange field. We conclude that the D_{F2} dependence is the most important layer thickness quantity for the spin current and spin transfer torque properties of the system, whereas the spin accumulation is highly dependent on both the D_N and D_{F2}, in addition to the interfacial scattering dependence as was seen in the previous subsection.

4.4 Conclusions

We have investigated spin transport for $F/N/F/S$ structures. Through our study, we have predicted the main characteristics of the relevant spintronic quantities, namely the spin current, the spin transfer torque, and the local magnetization (a proxy for spin accumulation). We have done so for multiple variations of the geometrical and interfacial parameters of the spin valve. Our focus has been on clean samples with thicknesses similar to those that have been fabricated, and which include a normal metal spacer and good interfaces. The material parameters employed, such as the internal field and coherence length, have been shown to be valid for such samples where Nb is the superconductor, Cu the normal spacer, and Co the ferromagnet: these values were successfully used previously to quantitatively fit, using our theoretical methods, the transition temperatures [9] of similar spin valve heterostructures. This quantitative success makes us confident as to the validity of the predictions presented here. Our main results are given as a function of position within the spin valve, and of the applied bias. We consider both low-bias values and the high bias limit where the bias exceeds the bulk superconductor gap. We emphasize the dependence of all results on the misalignment magnetization angle ϕ between the F layers; the misalignment determines the triplet pair formation, hence the range of the proximity effects and indeed the valve action. Our analysis includes variation of the interfacial scattering parameters and intermediate layer thicknesses to better encompass a full picture of possible real world results.

However, the parameter space is exceedingly large with no possible extrapolation due to the oscillatory behavior of many quantities and the complexity of the self consistent calculations required. Therefore, what we present here is merely a subset of our results with the expressed purpose of establishing the main characteristics of the outcomes and exhibiting a glimpse of the richness and variety of what can be done.

Our results are presented in detail in Sec. 4.3. We begin by discussing the dependence of the results on the scattering potential barriers that would be prevalent in even the most ideal fabrication processes. Then, starting with a realistic geometry, we vary the intermediate layer thicknesses while keeping them within an experimentally realistic range. In our results we see a distinct critical bias behavior where, for a certain value of the bias, which is in general ϕ dependent and always smaller than the bulk S gap value, the spin transport behavior changes, with both the spin current and the spin accumulation beginning to penetrate into the superconductor. By analyzing the spatially averaged spin accumulation and STT within each layer, we also see the critical bias behavior featured in the magnitude of these quantities. We are then able to analyze the trends both above and below the critical bias. These averages show distinct growth in the spin accumulation in S, and also in N for certain sets of both interfacial scattering and thickness parameters. The spin transfer torque also shares this behavior within the ferromagnetic regions, with an additional symmetrical behavior in the angular dependence when the interfacial barriers are fully introduced.

We also observe, at fixed higher bias, the spatial precession of the spin current within the ferromagnets due to the spin transfer torque. The spin current precesses about the internal field of the ferromagnet, with a decaying amplitude within the intermediate F_2 layer due to the proximity effect of the superconductor. This results in both the spin current and the spin accumulation being oriented within the superconductor at an angle near the field misalignment angle ϕ, and at an angle between zero and ϕ within the normal metal layer. This is only one way in which the misalignment angle plays a factor. Indeed, the critical bias features are angularly dependent chiefly because of the angular dependence of the triplet amplitudes, resulting in a very complex and in general non-monotonic behavior in ϕ for all of our spin transport quantities. The angular dependence of the critical bias was already exhibited in Chapter 2 for the charge current, and they correlate with the critical bias features found in the averages.

Another noteworthy feature of the spin accumulation occurs within the normal metal layer, where the system transitions, as parameters vary, from a situation where the magnitude of this quantity has a single peak at the center of the normal layer, to multiple peak behavior. We find that by varying *either* the interfacial scattering parameters *or* the normal metal layer thickness, we get a transition into a three-peak behavior. Naively, one would assume this to be due to the to the normal quantum mechanical effects of the spacial oscillations alone. However, by varying the thickness of the intermediate ferromagnetic layer D_{F2}, we see a two-peak behavior for the same normal metal layer thickness and interfacial scattering values. This is unique to these spin valve systems, which are highly sensitive to the exact set of parameters, both geometrical and physical. Indeed, the spatial spin current and spin accumulation features can not be extrapolated to trends within the set of parameters we have analyzed. However, the average quantities of the spin accumulation and spin transfer torque may be at least sometimes extrapolated at high bias values, as the spatial averages tend to be quasilinear in this limit.

We have calculated both the spin current and spin accumulation in superconducting spin valves for a set of experimentally relevant parameters. The dependencies of these quantities on the parameters (including the misalignment angle ϕ) are complex, non-monotonic, and extremely rich in features. We expect these results to be a footstool onto which more understanding can be developed for the spin transport properties of these nanoscale superconducting spin valves, both through experiment and through continued theoretical work.

Chapter 5

Quasi-particle Conductance in Ferromagnetic Josephson Structures

5.1 Introduction

So far we have discussed transport in superconducting spin valves and have found many promising features that could be useful in future application. We now wish to consider a spintronic, ferromagnetic Josephson structure with two intermediate ferromagnetic layers ($S/F/N/F/S$). Josephson junctions are electronic devices with high magnetic sensitivity due to the Josephson effect. This effect comes in two parts: The DC effect and the AC effect [7]. In the DC effect, an applied DC current runs through the Josephson junction at zero bias, up to a critical value, via the tunneling of the Cooper pairs. The AC effect describes the AC current driven by an applied bias with frequencies in the GHz range for an applied bias of 10 μeV [10]. These devices are ultra sensitive to magnetic fields due to the modulation of the critical Josephson current on the order of the magnetic flux quantum $\Phi_0 = 2\pi\hbar/2e$. Because of this, there is growing interest in using Josephson junctions in digital electronic devices such as the Rapid Single Flux Quantum (RSFQ) device, where information is stored and transmitted rapidly via the flux quanta. However, these devices can be made to be more efficient if it were to trade

its transistor components for magnetic memory such as the spin valve ($F/N/F$) [8]. Because of this, there has been a lot of interest in studying ferromagnetic Josephson structures such as the $S/F/S$ and $S/F/N/F/S$ structures. Most of the focus on these devices has been on the phase relationship of the Josephson junction. The relative phase of the superconductor with zero current is in either the 0 or π state. For the ferromagnetic Josephson structures, the equilibrium state can be changed between the 0 and π state by varying the thickness of the ferromagnetic layer [96] or the relative magnetization angle [97]. In addition, the critical current is also oscillatory with the layer thickness and exchange field strength [98, 99]. However, there are other important aspects of the Josephson structure that are independent of the phase.

Beyond the tunneling of Cooper pairs in the Josephson effect, there is the transport of a quasiparticle current through the sample. In the RCSJ model (Eq. 1.18), this would be the GV term of the net current [58, 59]. One can measure this GV current by shunting the junction, as we discussed at the end of Sec. 1.3. This leaves a hysteretic I-V characteristic at very low biases where the "capture" current is small (and the minimum nonzero voltage is small) in the DC Josephson effect for decreasing current. In the case of a non-tunnel junction, such as a clean or weak-link junction, there may exist unique subgap conductance features. A metallic weak-link is an $S/N/S$ structure in which the Josephson junction is separated by a thin metal, sometimes the same material as the superconductor. For example, a point contact may be formed with one superconductor in contact with a superconducting substrate. Another example is the microbridge, where a thin bridge is etched between two superconducting "banks" [100]. Although continuously connected, the intermediate region in each case is considered a normal metal constriction. This is because the constriction is smaller than the coherence length ($\ell \ll \xi_0$) which destroys superconductivity within the region. These constrictions are therefore studied in the dirty limit [20]. In the clean limit theory, the transport properties are not affected by a constriction or by impurity scattering [100]. We wish to study the quasiparticle current in the clean limit for $S/F/N/F/S$ structures using our self-consistent method which we present below. We are particularly interested in the subgap structure of the conductance.

In 1969, L. J. Barnes discovered multiple conductance peaks within the subgap bias region using superconducting point contacts [101]. In these Josephson structures, the

subgap region is considered to be any bias below 2Δ (or $\Delta_1 + \Delta_2$ in the case of two different superconductors). He found conductance peaks using niobium contacts for values of the bias of approximately $eV = 2\Delta/n$ where n is an integer. This subgap structure (SGS) has since been verified in other experiments on metallic weak-link junctions [102, 103, 104]. In 1982, BTK determined how Andreev reflections change the conductance features of an N/S heterostructure where in the subgap region ($eV < \Delta$ in this case) the conductance may be twice that of the normal conductance [50]. For nonzero interfacial scattering, this leads to peaks in the conductance at the critical bias ($eV = \Delta$). This peak represents the increase in energy needed for an electron in the normal metal to transport into the superconductor just above the superconducting energy gap, where the density of states is the highest. For biases less than the gap potential, the right-moving electron will instead Andreev reflect as a left-moving hole. In 1983, Octavio, Blonder, Tinkham, and Klapwijk (OBTK) described the phenomenon known as multiple Andreev reflection (MAR) [105]. In a superconducting junction that is biased between the two superconductors, an electron leaving the left superconductor will gain in energy before impinging on the right superconductor. If the energy is lower than the gap, it will reflect as a hole which then gains energy before impinging on the left superconductor. This process repeats itself until the original electron has gained enough energy to escape the gap, making multiple reflections in the process. There is thus a peak in conductance when the number of reflections n times the bias applied eV is equal to the energy gap 2Δ. OBTK go on to describe the subgap structure in $S/N/S$ junctions via the MAR, although what they find are peaks in the *resistance* for non-zero temperatures and/or non-zero scattering at the S/N interfaces. One important distinction is the plane wave assumptions of the clean limit theory as opposed to diffusive theory describing the weak-links. In OBTK (Ref. [105]), they use plane waves to describe the reflection coefficients at the N/S interfaces but assumed no interference of the reflected waves from each interface. In general, the plane waves may interfere upon multiple reflections which would diminish the subgap structure. However, as with any junction, there are quantum resonance effects due to the finite thickness of the layers separating the superconductors. In addition, OBTK assumes a non-self-consistent pair potential, and we have shown in the previous chapters of this thesis that a self-consistent pair potential is necessary to accurately describe transport [41, 67, 68, 69].

Other theoretical work on MAR in weak-link metallic junctions [106, 107] has been in the dirty limit [108, 109, 110]. We study these reflections and the resulting interference and resonance phenomenon in our ballistic, self-consistent theory for the ferromagnetic Josephson structure.

In the previous chapters we have studied the quasiparticle transport in superconducting spin valve structures ($F_1/N/F_2/S$). In these structures, the singlet Cooper pair correlations are short-ranged and oscillatory within the ferromagnet [26, 27]. The presence of a second ferromagnet allows for the formation of induced same-spin triplet correlations of the Cooper pairs which are long ranged within the ferromagnet [23, 34, 35, 36, 37, 38, 39]. Due to this, and the oscillatory nature of the singlet pair, we found that the subgap features of the system are highly dependent on the magnetic misalignment angle ϕ and the thickness of the F_2 layer. In Chapter 2 we found that the critical bias (CB), i.e. the bias value equal to the saturated pair potential $eV = \Delta$, was spatially and angularly dependent. In Chapter 3 we saw that the conductance features are spin-split between incoming spin-up and spin-down electrons where, in the subgap region, one spin-band features a peak in conductance while the other spin-band has a minimum. This lead to a peak conductance that is oscillatory between the zero bias and critical bias. It was also shown that these conductance features were highly dependent on the interfacial scattering. In fact, nonzero scattering is paramount to the formation of conductance peaks. These dependencies also apply to the $S_1/F_1/N/F_2/S_2$ system, and we will study the thickness and angular dependence in the results of this chapter.

In Sec. 5.2, we review our methods, which are the same as those in Sec. 1.4 and those used in Chapters 2 and 3, to study the $S_1/F_1/N/F_2/S_2$ spin valve Josephson structure. In that section, we also review our analytic approximation of the system to determine the relationship of the electron-hole resonance in $N/F/S$ and $S/F/S$ multilayers with interfacial scattering due to a normal metal contact. In Sec. 5.3 we present our results, starting with our analytic calculations on the simple $N/F/S$ and $S/F/S$ models, before moving on to the fully self-consistent, numerical calculations of the $S_1/F_1/N/F_2/S_2$ heterostructure. In all our calculations, we determine the thickness dependence of the F (or F_2) layer in relation to the resonance effects determined in Sec. 5.2.3. In addition, we determine the angular dependence for our numerical calculation. We find that the angular dependence is unique to that found in the $F_1/N/F_2/S$ systems previously

studied. We present our results for two sets of interfacial scattering parameters: clean interfaces and imperfect N/F interfaces. In each case, we assume nonzero scattering due to a normal metal contact. Finally, we summarize our results in Sec. 5.4.

5.2 Methods

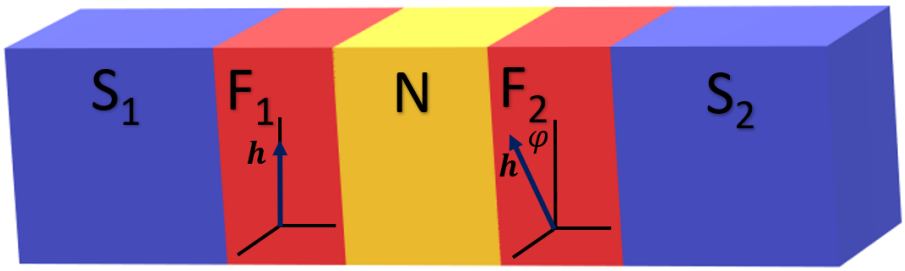

Figure 5.1: Sketch of the $S_1/F_1/N/F_2/S_2$ heterostructure. The magnetizations of the outer magnetic layer F_1 is along the z axis while that in F_2 it is rotated in the x-z plane by an angle ϕ. The y axis is normal to the layers. This sketch is not to scale.

5.2.1 Self-consistent calculation of the pair potential

The methods in this section are largely related to those used in the Introduction Sec. 1.4 for the calculation of the pair potential, and those used in Chaps. 2 and 3 for calculating the conductance. The primary difference is the inclusion of a second superconducting layer (see Fig. 5.1). The Hamiltonian for the $S_1/F_1/N/F_2/S_2$ multilayer is:

$$\begin{pmatrix} H_0 - h_z & -h_x & 0 & \Delta \\ -h_x & H_0 + h_z & \Delta & 0 \\ 0 & \Delta^* & -(H_0 - h_z) & -h_x \\ \Delta^* & 0 & -h_x & -(H_0 + h_z) \end{pmatrix} \begin{pmatrix} u_{n\uparrow} \\ u_{n\downarrow} \\ v_{n\uparrow} \\ v_{n\downarrow} \end{pmatrix} = \epsilon_n \begin{pmatrix} u_{n\uparrow} \\ u_{n\downarrow} \\ v_{n\uparrow} \\ v_{n\downarrow} \end{pmatrix} \tag{5.1}$$

where $H_0 = -(1/2m)(d^2/dy^2) + \epsilon_\perp - E_F(y) + U(y)$ is the usual single particle Hamiltonian with interfacial scattering $U(y) = \sum_i H_i \delta(y - y_i)$ where H_i is the barrier strength at the ith interface located at y_i. h is the exchange field within the ferromagnetic layers

and Δ is the pair potential within the superconducting layers. Each element in the matrix equation is implicitly a function of the position (y) within the multilayer. The form of the Hamiltonian is the same as was given in Sec. 1.4 except now we introduced the complex conjugate of the pair potential Δ^*. With a single superconductor, there is only one phase associated with the s-wave symmetry and thus we took the pair potential to be real. With two superconductors there may exist a phase difference. Using our self-consistent method, we initialize the pair potential within each layer to a selected starting phase difference, $\Delta_1(y) = \Delta_0$ and $\Delta_2(y) = \Delta_0 e^{i\theta}$ where Δ_1 is the value of Δ for y values within the S_1 layer, and similarly for Δ_2, then solve Eq. (5.1). We then evaluate the self consistent equation,

$$\Delta(y) = \frac{g(y)}{2} \sum_n{}' \left[u_{n\uparrow}(y) v^*_{n\downarrow}(y) + u_{n\downarrow}(y) v^*_{n\uparrow}(y) \right] \tanh\left(\frac{\epsilon_n}{2T}\right) \tag{5.2}$$

where $g(y)$ is zero *except* in the S layers and the sum is over all eigenstates with energies less than ω_D. We iteratively solve for $\Delta(y)$ as explained in Sec. 1.4. The phase of the complex pair potential will also iterate using this method. For the equilibrium calculation (zero current), there are always two local stabilities in the phase: 0 and π. For an initial guess where the phase difference is not equal to 0 or π, the final self-consistent phase will always converge to the phase which minimizes the free energy. The phase which minimizes the free energy is dependent on the thickness [96] and relative magnetization angle [97] of the ferromagnets. At zero temperature, this is equivalent to maximizing the average value of the pair potential within the superconductor. In our numerical, self-consistent results presented, the overall phase corresponding to the plot displayed is that which minimizes the free energy, i.e. the equilibrium phase. The self-consistent method is made necessary to preserve charge conservation, as explained in Sec. 2.2.3.

Using this method, it is possible to allow for two different superconductors ($\Delta_{0,1} \neq \Delta_{0,2}$) where the coherence length is different for each S layer. We focus our attention here to the case in which the two superconductors are made of the same material. This does not mean that the pair potential $\Delta(y)$ will be symmetric or have the same magnitude in each S layer, as the proximity effect does not impact both superconductors equally as we vary the F layer thicknesses. It should be noted that one could achieve

the same result by varying the thickness of the individual S layers.

5.2.2 Quasi-particle Conductance

In the previous subsection, we determined the equilibrium properties of the $S/F/N/F/S$ system, in particular the spatial dependence of the pair potential. In this subsection, we review our methods for calculating the conductance which are similar to those presented in Chapters 2 and 3. In order to simplify our calculation, we introduce a thin normal metal contact, denoted by 'X', located to the left of the S_1 layer (see Fig. 5.1). This makes the ferromagnetic Josephson structure effectively $X/S_1/F_1/N/F_2/S_2$. This layer is taken to be small enough to not affect the calculation of the pair potential through the proximity effect. For this reason, it is not necessary to include it in the equilibrium calculation above. We explain our reasoning for introducing this X contact at the end of this subsection after we have introduced our methods.

We use the same BTK [50] method to calculate the conductance as we had done in the previous chapters. The BTK method calculates the conductance from the reflection amplitudes of spin-dependent ordinary (b_σ) and Andreev (a_σ) reflections within the left-most layer via Eq. (2.14). We determine the reflection amplitudes by writing the incoming wavefunctions using these amplitudes and applying the boundary conditions at the end layers and the continuity conditions at the interfaces. If a spin-up incoming electron in the left-most layer is traveling in the normal metal contact X, the incoming wavefunction is:

$$\Psi_{X,\uparrow} \equiv \begin{pmatrix} e^{ik_N^+ y} + b_{\uparrow,\uparrow} e^{-ik_N^+ y} \\ b_{\downarrow,\uparrow} e^{-ik_N^+ y} \\ a_{\uparrow,\uparrow} e^{ik_N^- y} \\ a_{\downarrow\uparrow} e^{ik_N^- y} \end{pmatrix} \tag{5.3}$$

and for a spin-down incoming electron:

$$\Psi_{X,\uparrow} \equiv \begin{pmatrix} b_{\uparrow,\uparrow} e^{-ik_N^+ y} \\ e^{ik_N^+ y} + b_{\downarrow,\uparrow} e^{-ik_N^+ y} \\ a_{\uparrow,\uparrow} e^{ik_N^- y} \\ a_{\downarrow\uparrow} e^{ik_N^- y} \end{pmatrix} \tag{5.4}$$

where the second spin index of the reflection amplitudes denotes the spin of the incoming particle and $k_N^{\pm} = \left[E_F \pm \epsilon - k_\perp^2\right]^{1/2}$ is the normal metal wavenumber. The procedure follows that used in Chapters 2 and 3. The continuity condition of the wavefunctions at each interface can be represented by a matrix equation $M_{i,r}x_i = M_{i+1,\ell}x_{i+1}$ where $M_{i,r}$ and $M_{i,\ell}$ are the wavefunction coefficients of the ith layer evaluated at the right and left interface respectively, and x is the vector of the reflection/transmission amplitudes. At the X layer, this equation becomes $M_X x_X + c_\sigma = M_{S1,\ell}x_{S1}$ where c_σ is the vector of the incoming spin σ electron coefficients. The wavefunctions are described in Chapter 2 for the ferromagnetic (F) and superconducting (S) layers. The addition of a second superconducting layer is straight forward as it uses the same self-consistent approach as in Chapter 2. The conductance is then calculated via the BTK method using Eq. (2.14).

In each system we study in this chapter we introduce a normal metal contact X. This way we can describe the left-most layer using incoming electrons and holes, as opposed to the electron-like and hole-like quasiparticles of the superconductor (see e.g. Ref. [50]). Although a description using incoming electron/hole-like quasiparticle amplitudes has been used in studies on the phase relationship in Josephson structures [111], this approach is not well suited for determining the transport properties within the subgap region as these amplitudes can not describe excitations with a subgap energy – only energies above the gap. To probe the subgap energies means describing incoming Cooper pairs instead of the excitation amplitudes. With the X layer we are able to describe the quasiparticle states for the subgap in terms of the incoming electron/hole excitation amplitudes. In addition, the BTK method for extracting the conductance (see Eq. 2.14) is described via the reflected electron and Andreev reflected hole amplitudes. To describe the system using the electron-like and hole-like quasiparticle reflection coefficients would require an entirely new formalism. Adding a normal metal contact is justified on the basis that all real systems have contacts from which measurements are made. In addition, we can study the effects of the interfacial scattering due to imperfect contact interfaces. The introduction of a scattering interface allows for multiple Andreev reflections in both single superconductor heterostructures and the Josephson structures, the results of which are conductance peaks in the subgap region sometimes known as the subgap structure (SGS).

In the next subsection, we go over our analytic approach to better understand the

origins of the subgap conductance peaks.

5.2.3 Analytic Approximation

In this subsection we describe our analytic approximation. The purpose of this approximation is to provide some physical intuition and a qualitative description of the finer details in the full numerical $S_1/F_1/N/F_2/S_2$ results. To do this we start with a simple $N/F/S$ model (see Figs. 5.2 and 5.3) and extend it to a ferromagnetic Josephson structure $S_1/F/S_2$ with normal metal contact X (see Figs. 5.4 and 5.5). In order to make our calculation analytic, we make the following assumptions: The analytic model is one-dimensional (as opposed to quasi-one dimensional) with infinite layer thicknesses at the left and right ends. Therefore, the only thickness dependencies come from the intermediate layers F and S_1. We assume a non-self consistent pair potential where $\Delta_1 = \Delta_2 = \Delta_0$ is a constant for both the single S and Josephson structures. In our analytic calculations, the 0 and π phases are degenerate due to the non-self-consistent pair potential, and thus we leave the phase to be zero. In the case of the ferromagnetic Josephson structure, we include a normal metal contact X to the S_1 layer with nonzero interfacial scattering at the X/S_1 contact interface, for reasons described above. The calculation of the conductance is then the same as in the numerical calculation. The reflection amplitudes can be solved using $x_N = \mathcal{M}_N^{-1}\mathcal{M}_{F,\ell}\mathcal{M}_{F,r}^{-1}\mathcal{M}_S x_S - \mathcal{M}_N^{-1}c_\sigma$ in the $N/F/S$ case and $x_X = \mathcal{M}_X^{-1}\mathcal{M}_{S1,\ell}\mathcal{M}_{S1,r}^{-1}\mathcal{M}_{F,\ell}\mathcal{M}_{F,r}^{-1}\mathcal{M}_{S2}x_{S2} - \mathcal{M}_X^{-1}c_\sigma$ in the $S/F/S$ case with normal contact X. In addition, this can be extended to the case of an intermediate normal metal N instead of a ferromagnet simply by taking the exchange field h to be zero.

The conductance is then calculated via the BTK method and Eq. (2.14). The full form, analytical solution involves inverting multiple 8×8 matrices (which can be done simply using Mathematica). However, the full solution is inscrutable and can not be simplified. Despite having an analytic solution, the form of the conductance is complicated due to the sheer number of plane wave combinations of the $\mathcal{M}$ coefficients that are present in each reflection amplitude. Therefore, we do an analysis similar to the one we did in Chapter 3 in connection to Figs. 3.3 and 3.4. There, for the $N/F/S$ system, we considered some of the possible plane wave combinations to derive the periodic structure. We found that the reflection amplitudes have a periodicity of

$2\pi/h$ (in dimensionless units) on the thickness of the F layer. This leads to a periodicity of the conductance peak position of π/h, where the subgap peak conductance oscillates between the zero bias and critical bias for increasing thickness of the F layer. However, there is another plane wave combination we should consider which describes the SGS for $h = 0$.

In the N/S system with a non-zero barrier at the interface, there is a peak in conductance at the critical bias due to Andreev reflections [50]. Now consider an $N'/N/S$ system (for example, if there is a normal metal contact N'). If the additional normal metal has an interfacial scattering barrier at the N'/N interface, it is possible for the Andreev reflected holes at the N/S interface to interfere with the reflections at the N'/N interface. We may look for resonance effects by examining the plane wave combination $e^{ik_N^+ D_N} e^{-ik_N^- D_N}$ at the critical bias $\epsilon = \Delta_0$. The wavenumber in the normal metal is then

$$k_N^{\pm} = [1 \pm \Delta_0]^{1/2} \approx 1 \pm \Delta_0/2 \tag{5.5}$$

The combination is in resonance when $e^{i\Delta_0 D_N} = e^{2\pi i n}$ where n is the integer of the harmonic resonance. Thus, the resonance of the amplitudes are expected to occur for

$$D_N = \frac{2\pi}{\Delta_0} n = \pi^2 n \Xi_0 \tag{5.6}$$

where the normalized pair potential Δ_0 is related to the (dimensionless) coherence length Ξ_0 by $\Delta_0 = \frac{2}{\pi \Xi_0}$ [10, 16]. The conductance is proportional to the absolute square of the amplitudes, thus the periodicity in the conductance peak resonance occurring at the critical bias should be

$$\lambda_n = \frac{\pi^2}{2} n \Xi_0 \tag{5.7}$$

In Sec. 5.3.1, we plot the calculated conductance for varying thicknesses $D_N = \lambda_n$. What we see is that the λ_n periodicity describes the formation of *new* peaks at the critical bias, shifting the previous n numbered peak into the subgap, as we discuss in greater detail therein. This resonance is the result of multiple Andreev reflections, where an electron/hole is Andreev reflected off the S layer and is again reflected at the N'/N interface. The integer n is the harmonic of this resonance effect. For $h \neq 0$, there is an additional oscillatory behavior due to the spin-split effect described in Chap. 3, which

we discuss in Sec. 5.3.1 as well.

In the Josephson structure $S/N/S$, we introduce an additional S layer. This leads to another layer thickness dependence on the conductance that is different from the N/S case. Andreev reflected electrons and holes from the N/S_2 interface may be Andreev reflected again at the S_1/N interface. If we again consider a normal metal contact X with interfacial scattering at the X/S_1 contact, the quasiparticles which transmit through the S_1 layer may also reflect at the X/S_1 contact. The net result is a complex resonance effect that can be divided into two parts: resonance from reflections at the X/S_1 interface and those reflected at the S_1/N interface. We do not have a simple argument for the exact resonance behavior and must use a more phenomenological approach. We first assume a resonance effect similar to Eq. (5.7). Then, we introduce a term Q to take into account the dependence of the resonance on D_S. We find two harmonic resonance effects on the thickness of the intermediate N layer, labeled as the even and odd harmonics:

$$\begin{aligned} \frac{\lambda_{n,even}}{\Xi_0} &= \frac{\pi^2}{2}n, \quad n = 0, 2, 4, ... \\ \frac{\lambda_{n,odd}}{\Xi_0} &= \frac{\pi^2}{2}n - Q\left(\frac{D_{S_1}}{\Xi_0}\right), \quad n = 1, 3, 5, ... \end{aligned} \tag{5.8}$$

where we find $Q\left(D_{S_1}/\Xi_0\right) \approx 1.2 \ln\left(D_{S_1}/\Xi_0\right) + 1.94$ approximates the resonance values. The even terms are due to reflections at the S_1/N interface and have the same form as Eq. (5.7) while the odd terms are due to reflections at the X/S_1 contact interface. The odd resonance values are reduced by a coefficient Q which is dependent only on the ratio D_{S_1}/Ξ_0. The critical bias forms peaks which are equally separated between each harmonic n for constant D_{S_1}/Ξ_0. We study these peaks for multiple harmonics in the $h = 0$ case and the $h \neq 0$ case in Sec. 5.3.2.

In this work, we will not study the higher harmonics ($n \geq 1$) using our numerical method. This is for two reasons: first, the peak positions are much more difficult to predict as the saturated pair potential (or the "effective" coherence length $\Xi = \frac{2}{\pi\Delta}$) is not constant for increasing intermediate layer thicknesses due to the proximity effect. Second, the $n = 1$ harmonic occurs for very large intermediate thicknesses: about five times the coherence length of the superconductor. The nanostructures we wish to study (those built by experimentalists) typically have a total intermediate thickness less than

or on the same order as the coherence length, which is why we study these systems in the ballistic limit. By introducing ferromagnets we can probe the higher harmonic peaks at lower intermediate thicknesses due to the oscillatory behavior of the peaks. We do this analytically in Sec. 5.3.2 and numerically in Sec. 5.3.3 for the $S_1/F_1/N/F_2/S_2$ ferromagnetic Josephson structure.

5.3 Results

In this section we present our results on the conductance in the ferromagnetic Josephson structures ($S/F/S$ and $S/F/N/F/S$). As in the previous chapters we focus on the forward conductance at the $T \to 0$ limit. We introduce a normal metal contact X which simplifies the model as discussed in Sec. 5.2.2. We start our analysis with a simplified analytic model of the $N/F/S$ structure and work our way up to the $S/F/S$ structure. Although this model is quantitatively inaccurate, it does highlight the qualitative features of the subgap conductance. This qualitative description is very useful when describing the fully self-consistent numerical results of the $S_1/F_1/N/F_2/S_2$ structure. In all our results on Josephson structures, we introduce a normal metal contact X such that the system is $X/S/F/S$ or $X/S_1/F_1/N/F_2/S_2$. In our numerical results, we determine the thickness dependence of the F_2 layer as well as the dependence of ϕ, the misalignment angle of the F layer magnetizations. The thickness dependence will be described in relation to the analytic results.

Our results are parameterized by the layer thicknesses and the coherence length of the superconductor. These length scales are made dimensionless by normalizing them to k_F. The dimensionless bias E is normalized by the bulk pair potential Δ_0 and the conductance is in units of $2\pi e/\hbar$. The interfacial scattering barriers H_B are normalized by v_F. In each figure below, we take the scattering at the left-side contact interfaces (X/S, N/F, and N'/N) to be $H_B = 0.5$. This barrier enhances many of the subgap conductance features by making the peaks sharper. In the analytic results we assume no interfacial scattering at the N/S and F/S interface for simplicity, and in the numerical calculations we consider both zero and non-zero interfacial scattering at the intermediate F/N interfaces. We take the ferromagnetic exchange field to be $h = 0.145$, normalized by E_F, and the dimensionless coherence length to be $\Xi_0 = 115$ for each ferromagnetic

and superconducting layer respectively. These values have been found to be suitable to describe systems using cobalt and niobium [9].

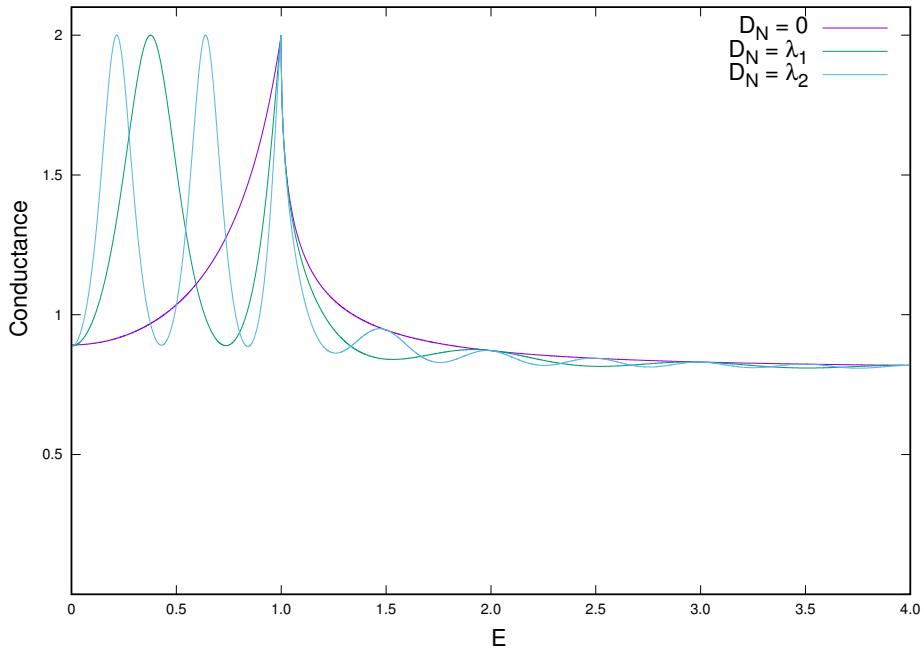

Figure 5.2: Conductance (G) vs. Bias (E) in the $N'/N/S$ structure for varying D_N. $\lambda_n \equiv \frac{\pi^2}{2} n \Xi_0$ are the resonance values at which a new peak forms at the critical bias, moving the previous peaks into the subgap region. We assume a single barrier at N'/N interface with $H_B = 0.5$. Analytic approximation.

5.3.1 N′/N/S and N/F/S analytic results

We start our discussion with the analytic $N/F/S$ and $N'/N/S$ structures. In Fig. 5.2 we plot the conductance for the $N'/N/S$ multilayer for multiple layer thicknesses of the intermediate N layer $D_N = \lambda_n$ and a single barrier $H_B = 0.5$ at the N'/N interface. This interfacial scattering is representative of an imperfect metallic contact interface, but it is still far from the tunneling limit. The left- and right-most layers (N' and S) are assumed infinite in thickness in the analytic approximation. The thicknesses λ_n are the resonance values found in Eq. (5.7) and represent the interference of the Andreev reflected electrons and holes with those reflected at the N'/N interface. The case $D_N = 0$ is equivalent to the N/S system studied by BTK for $Z = 0.5$ [50]. As

seen in BTK, the effect of the barrier decreases the conductance in the subgap region (and at the high bias limit) without decreasing the conductance at the critical bias (CB) $eV = \Delta_0$. This forms a sharp peak in the conductance. As the thickness D_N increases, the critical bias peak shifts into the subgap region and a new peak is formed at the CB when the thickness reaches a resonance value. Increasing D_N further, another peak forms shifting the other peaks further towards zero bias, and so on for each resonance value. We see that the peaks are evenly spaced for each thickness plotted. In addition, we see an additional oscillatory behavior in the conductance just above the critical bias. This oscillatory pattern decays at the same rate as in the N/S case ($D_N = 0$) towards the normal conductance. The frequency of the oscillations is proportional to the harmonic n of the N layer thickness resonance. The thicknesses of the intermediate layer depicted in Fig. 5.2 are quite large, about five times the coherence length of the superconductor for λ_1 and ten times for λ_2. This makes the results less relevant to the nanoscale heterostructures that we intend to study, where the intermediate layer thicknesses are on the order of the coherence length or less. However, this analytic calculation provides an excellent illustration of the subgap peak structure. We will see that this structure plays a prominent role in ferromagnetic Josephson structures $S/F/S$. Below we will further probe this structure by replacing the intermediate normal metal with a ferromagnet.

In Chapter 3 we discussed the spin-split conductance for the superconducting spin valve ($F/N/F/S$). In Sec. 3.3.1 we studied the effect in a similar analytic approximation for the $N/F/S$ model. However, we did so for only small thicknesses D_F. What we found was that the peak conductance oscillates between the critical bias and near zero bias with increasing thickness. This is due to the spin-split conductance, where the conductance features differ for incoming spin up and spin down electrons. From our analysis we found the wavelength of the oscillations to be π/h. For these small thicknesses, there is only one resonance peak attributed to the $n = 0$ harmonic. In Fig. 5.3 we plot the conductance for the $N/F/S$ system, but for D_F values close to the λ_1 resonance thickness. The periodicity of the spin-split conductance peak is significantly smaller ($\pi/h \approx 22$) than the resonance thickness ($\lambda_1 \approx 568$). We plot in Fig. 5.3 one full period of the spin split oscillation. We see that the conductance oscillates between two different two-peak states: one with the peaks located at the CB and near the middle

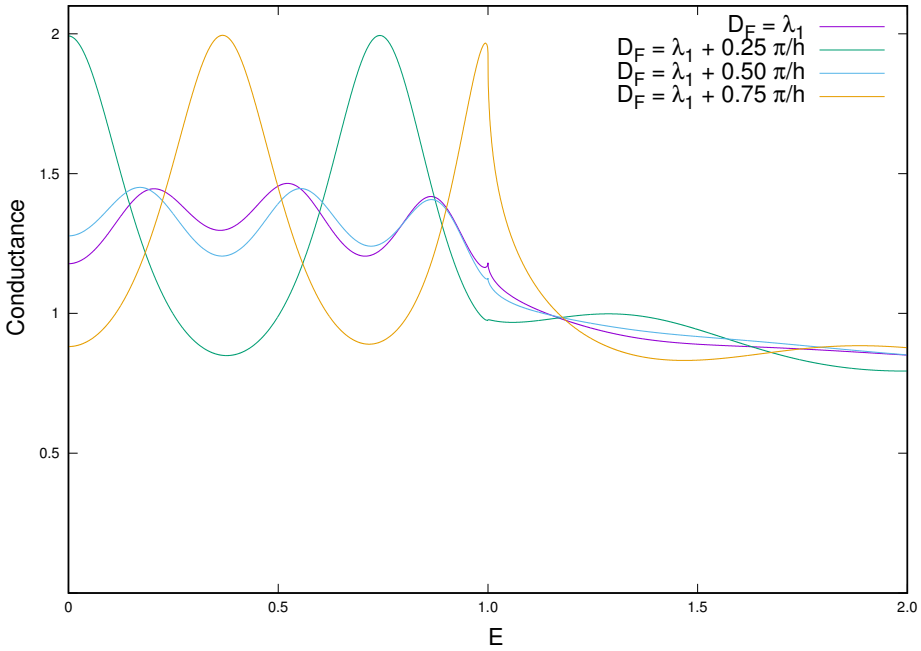

Figure 5.3: Conductance (G) vs. Bias (E) in the $N/F/S$ structure for varying D_F. $\lambda_1 = \frac{\pi^2}{2}\Xi_0 \approx 568$ is the first harmonic resonance and $\pi/h \approx 22$. The figure is plotted for one full oscillation of the thickness dependence. We assume a single barrier at N/F interface with $H_B = 0.5$. Analytic approximation.

of the subgap, and one with the peaks located near zero bias and the middle of the subgap. As the thickness increases, the set of two peaks oscillate between low biases and the critical bias, similar to that for the small F thicknesses studied before. Between these states, each peak splits into two, which is equivalent to the subgap peaks found in the small D_F case, and features a cusp peak near the CB. These subgap peaks are a split of the two resonance peaks for the first ($n = 1$) harmonic. Because this oscillatory behavior effectively shifts all resonance peaks further into the subgap, it is possible to have multiple subgap peaks for thicknesses less than the first harmonic resonance thickness as the higher order resonance peak will shift from the CB into the subgap region. However, the thickness must still be much larger than the coherence length to see this effect in $N/F/S$ systems.

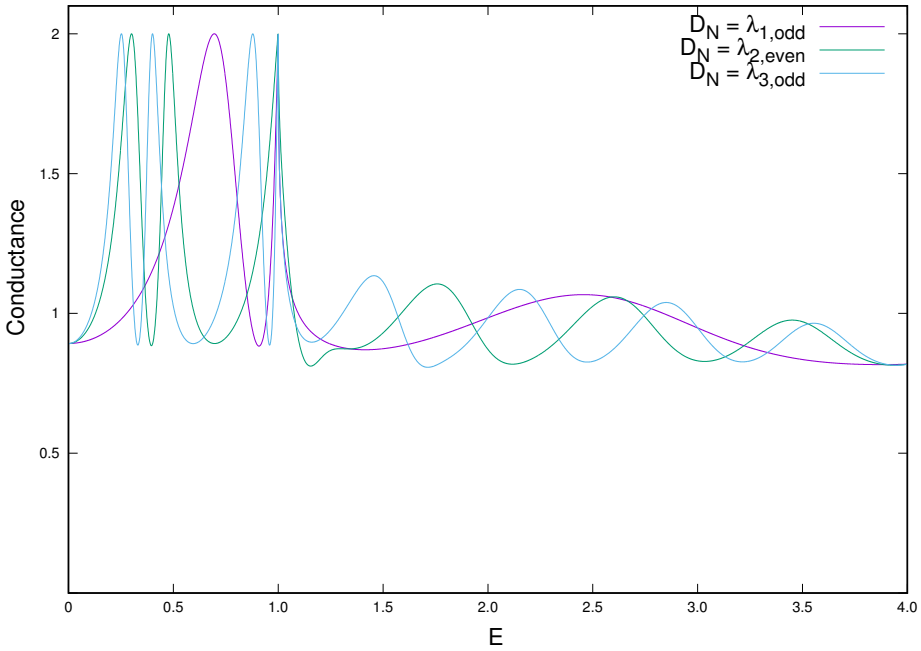

Figure 5.4: Conductance (G) vs. Bias (E) in the $S_1/N/S_2$ structure for $D_{S1} = 180$ varying D_N. See Eq. (5.8) for thicknesses λ_n and relevant discussion. The "odd" peaks are shifted by a constant in their resonance values. We assume a single barrier at the X/S_1 contact with $H_B = 0.5$. Analytic approximation.

5.3.2 S/N/S and S/F/S analytic results

We now turn our attention to the analytic $S_1/N/S_2$ and $S_1/F/S_2$ Josephson structures. In Fig. 5.4 we plot the conductance for the $S_1/N/S_2$ structure with $D_{S1} = 180$ and for resonance values of the N layer thickness (Eq. 5.8). We also include a normal metal contact X with nonzero interfacial scattering at the X/S_1 contact $H_B = 0.5$. As discussed in Sec. 5.2.3 the Josephson structure has two resonance values on D_N: the "even" and "odd" resonances. The even resonances are the same as for the $N'/N/S$ case, but the odd resonances have an extra factor $Q\,(D_{S1}/\Xi_0)$ (see Eq. 5.8) that decreases the resonance thickness for the odd n harmonics (from $\lambda_1 \approx 568$ to 282). This split in resonances is due to the difference in the reflections at the S_1/N and the X/S_1 interfaces. The exact form of this constant was not determined, but from analyzing results such as those shown in Fig. 5.4 we were able to approximate the value of Q in the resonance Eq. (5.8). We plot a range of thicknesses which include the first two odd resonances

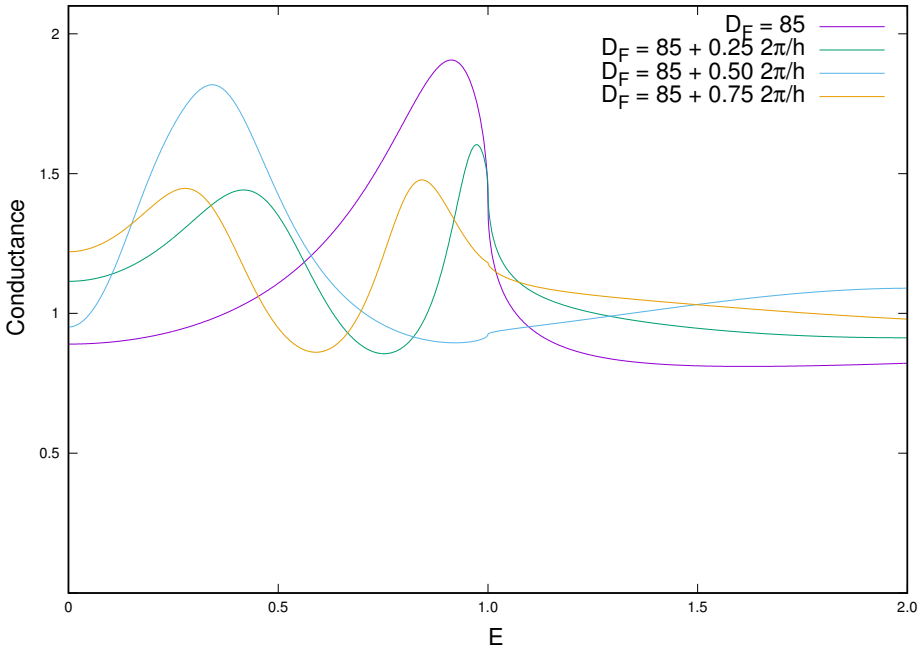

Figure 5.5: Conductance (G) vs. Bias (E) in the $S_1/F/S_2$ structure for $D_{S1} = 180$ varying D_F. We plot the conductance for one full oscillation of the thickness periodicity $2\pi/h \approx 43$. We assume a single barrier at the X/S_1 contact with $H_B = 0.5$. Analytic approximation.

$(n = 1, 3)$ as well as the $n = 2$ even resonance. As D_N increases, we see the same movement of the critical bias peaks into the subgap region. However, due to the dual resonance structures, these peaks are not evenly spaced. Furthermore, the oscillations above the gap are not in phase and the frequency is not directly proportional to the harmonic n for the odd resonances.

In Fig. 5.5 we plot the conductance for the $S_1/F/S_2$ structure in our analytic approximation which includes an imperfect contact X. We have previously established in Chapter. 3 that the conductance peak is oscillatory between low biases and the CB for varying D_F thicknesses in $N/F/S$ structures. In the previous subsection, we have shown this extends to all resonance peaks. We now do the same analysis for the ferromagnetic Josephson structure. We see an oscillatory behavior due to the spin-split conductance that is similar to the $N/F/S$ case, except the total periodicity is now $2\pi/h \approx 43$. We set the minimum thickness to be $D_F = 85$ which is less than the first $n = 1$ resonance value $(\lambda_{1,odd} \approx 282)$. We use this value for two reasons; First, this value is the minimum total

thickness of the intermediate layers (between S_1 and S_2) in our numerical calculations on the $S_1/F_1/N/F_2/S_2$ ferromagnetic Josephson structure. Second, we wish to show how the oscillations of the resonance peaks can shift a higher order harmonic peak into the subgap region, allowing for multiple subgap peaks. Indeed, in Fig. 5.5 we see a single conductance peak at $D_F = 85$. As D_F increases, it splits into two subgap peaks (with one being very near the CB). Then, the two peaks reform at $D_F = 85 + \pi/h$ into a single subgap peak. Increasing further, this peak splits into two subgap peaks with one being at very low biases. This is quite different than that found in the $N/F/S$ structure. Not only is the overall periodicity of the behavior doubled, but here there may exist multiple, distinct subgap peaks instead of a single peak and a cusp at the critical bias. This occurs for realistic thicknesses of the intermediate layers, at least in our analytic approximation. In the next subsection, we analyze the fully self-consistent $S_1/F_1/N/F_2/S_2$ structure.

5.3.3 Self-consistent, numerical $\mathbf{S_1/F_1/N/F_2/S_2}$ conductance: $\mathbf{F_2}$ layer thickness dependence

Through our approximate analytic study, we have found that there are two sources of resonance in the $S/F/S$ Josephson structure that form conductance peaks in the subgap region. Furthermore, these peaks are oscillatory with increasing thickness of the F layer. We now discuss the numerical results of the ferromagnetic Josephson structure $S_1/F_1/N/F_2/S_2$. We include a normal metal contact X, with nonzero interfacial scattering at the X/S_1 contact, which allows us to simplify our methods in Sec. 5.2.2. In our numerical calculations, the pair potential within each superconductor is a function of position within the multilayer, as determined by our self-consistent method. Furthermore, each layer has a finite thickness. The metallic contact is small enough not to affect the proximity effect. Our results focus on the quasiparticle current, and do not reflect the zero bias current due to the Josephson effect. Therefore, in interpreting our results, it should be noted that the ultra-low bias conductance may be inaccessible in experiment, even with a hysteresis current from a shunted Josephson circuit, due to the Josephson current.

In all the figures below we display two sets of plots labeled (a) and (b). Subfigures (a) have only a single barrier at the X/S_1 contact while (b) have additional barriers at the

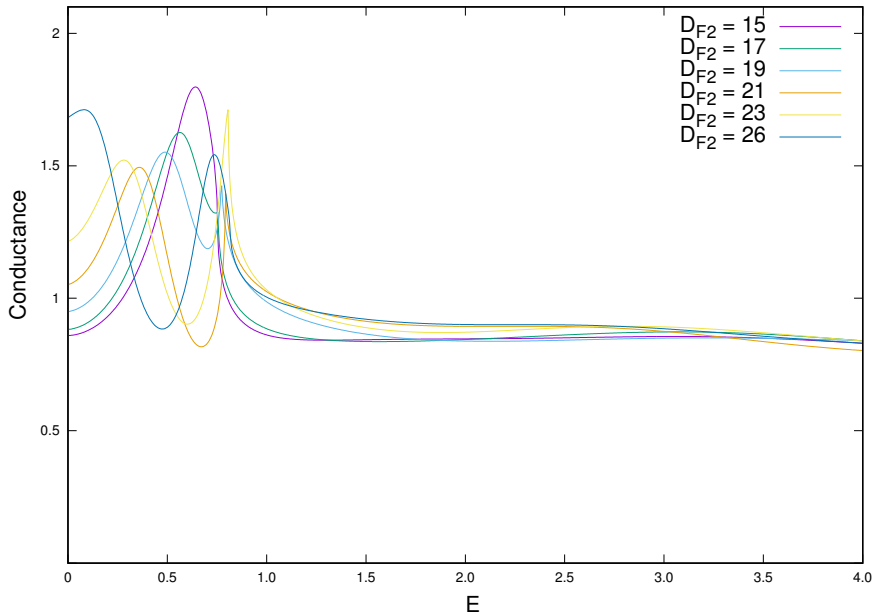

(a) Single barrier at the X/S_1 contact with $H_{B,0} = 0.5$.

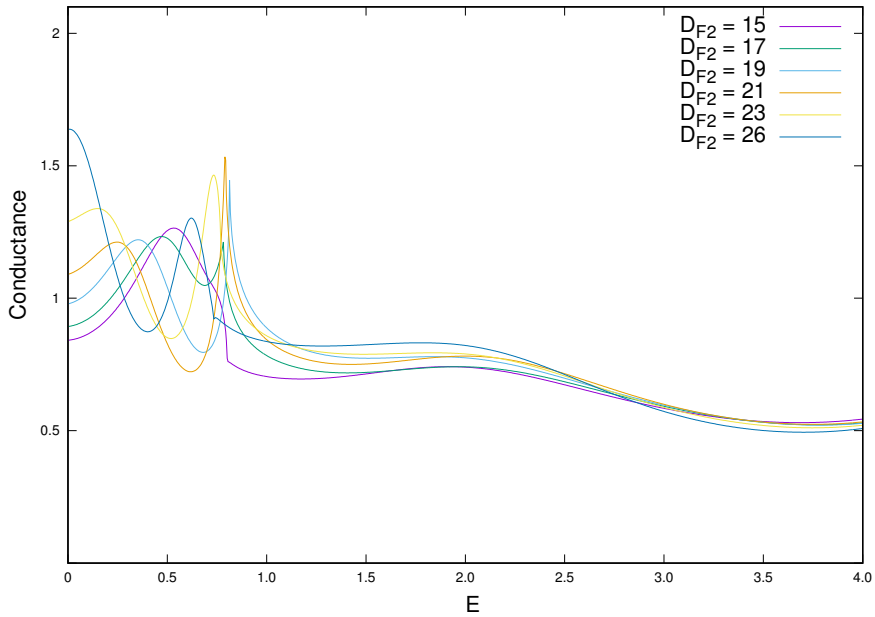

(b) Barrier at the X/S_1 and F/N interfaces with $H_{B,0} = H_{B,2} = H_{B,3} = 0.5$.

Figure 5.6: Self consistent, numerical results for the Conductance (G) vs. Bias (E) in the $S_1/F_1/N/F_2/S_2$ structure for varying D_{F2} and $\phi = 0$, plotted for approximately one quarter of the D_{F2} periodicity.

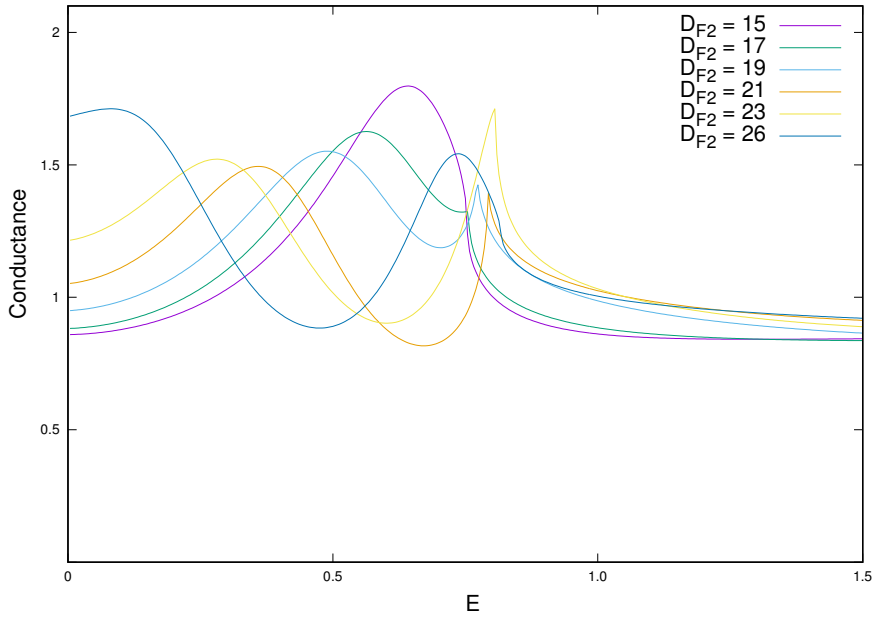

(a) Single barrier at the X/S_1 contact with $H_{B,0} = 0.5$. Subgap region of Fig. 5.6a.

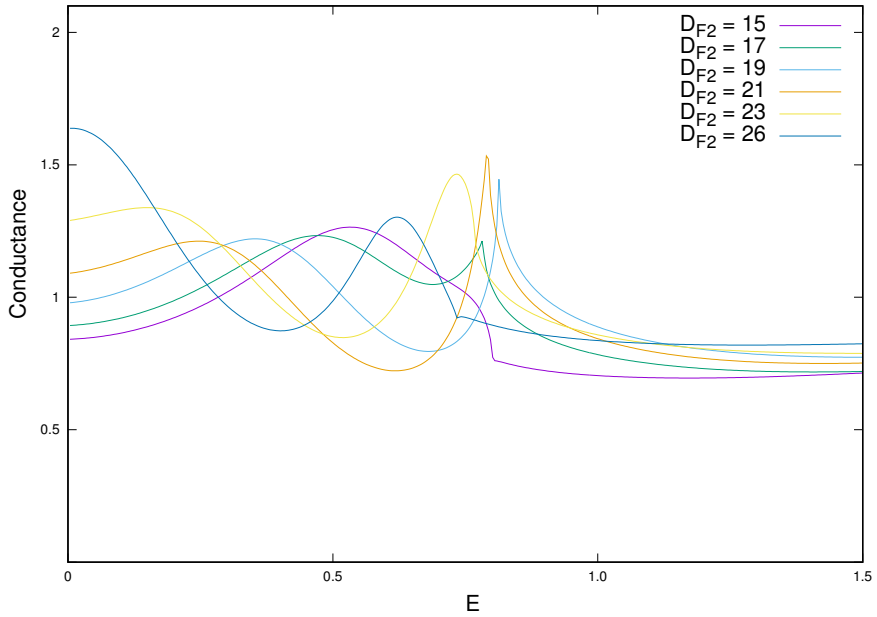

(b) Barrier at the X/S_1 and F/N interfaces with $H_{B,0} = H_{B,2} = H_{B,3} = 0.5$. Subgap region of Fig. 5.6b.

Figure 5.7: Self consistent, numerical results for the Conductance (G) vs. Bias (E) in the $S_1/F_1/N/F_2/S_2$ structure for varying D_{F2} and $\phi = 0$. Subgap region of Fig. 5.6 for (a) and (b) respectively.

F_1/N and N/F_2 interfaces, which account for more realistic samples with imperfections in the $F/N/F$ spin valve portion. We always assume no barriers at the F/S interfaces in order to maximize the proximity effect due to the ferromagnets. The interfacial scattering strengths $H_{B,i}$ are indexed from the far left X/S_1 to the right F_2/S_2 starting from zero. So at the X/S_1 contact, $H_{B,0} = 0.5$ in all figures, $H_{B,2} = H_{B,3} = 0$ at the F/N interfaces for the (a) subfigures, and $H_{B,2} = H_{B,3} = 0.5$ for the (b) subfigures. In the numerical calculation, all layers are finite in width. We keep all layer thicknesses constant except the F_2 layer: $D_{S1} = D_{S2} = 180$, $D_{F1} = 30$ and $D_N = 40$. The normal metal contact thickness is $D_X = 5$. We set $h = 0.145$ and $\Xi_0 = 115$. In this subsection, the magnetization of the ferromagnetic layers are parallel ($\phi = 0$) and we determine the dependence of the conductance features on D_{F2}. In Sec. 5.3.4 we determine the dependence on the misalignment angle ϕ.

In Figs. 5.6 and 5.7 we plot the conductance for $\phi = 0$ and varying D_{F2}. The difference in the two figures is in the x-axis scale where in Fig. 5.6, for biases above the gap, we can see an oscillatory structure and in Fig. 5.7 we focus on the subgap bias region. In Subfigure 5.6a we see small oscillations of the conductance at high bias values. The phase of these oscillations depends on the thickness of the F_2 layer. In Subfigure 5.6b, which includes barriers at the F/N interfaces, we see that these oscillations are relatively larger as the conductance exponentially decrease at high biases to that of the normal conductance. This enhances the oscillatory structure above the gap for all layer thicknesses shown.

In Fig. 5.7 we can more clearly see the subgap structure of the conductance. From $D_{F2} = 15$ to $D_{F2} = 26$ we go from a single peak near the CB to a two-peak structure, one at low bias and one just below the critical bias. As D_{F2} increases from 15, we see the single peak shift into the subgap until a second peak forms at the CB at around $D_{F2} = 21$. The thickness difference between $D_{F2} = 15$ and $D_{F2} = 26$ is about $\pi/2h$, which is one quarter of the total oscillatory pattern (see Fig. 5.5 for reference). Comparing Figs. 5.7a and 5.7b, we see the effect that the F/N barriers have on the system. We see that the phase of the oscillatory spin-split behavior shifts slightly and the conductance decreases. The subgap peak structure is *not* enhanced by the barriers, but instead the conductance is decreased in all peak values.

5.3.4 Self-consistent, numerical $S_1/F_1/N/F_1/S_1$ conductance: angular dependence

Much of the interest in the spin-valve Josephson structure is the ability to store information in the relative orientation of the magnetization in the F layers. The angular dependence of the conductance constitutes a valve effect in the system. In the superconducting spin valve structure ($F/N/F/S$) studied in Chapter 3, we found a large valve effect in the subgap conductance for certain thicknesses of the F_2 layer. We aim to determine the angular dependence of the $S_1/F_1/N/F_2/S_2$ structure and determine the viability of the valve effect found. To do this, we analyze two of the thicknesses plotted in Fig. 5.7, $D_{F2} = 15$ and $D_{F2} = 26$. We choose these two thicknesses because they are separated by a value of $\pi/2h \approx 11$, one quarter of the full periodicity. We will then compare the angular dependence of ϕ with the spatial dependence found in Fig. 5.7.

In Fig. 5.8 we plot the conductance for $D_{F2} = 15$ and determine the angular dependence. The $\phi = 0$ results are the same as those in Fig. 5.7. In Fig. 5.8a we see a single peak conductance at $\phi = 0$. At $\phi = 90°$ the single peak splits into a subgap peak and a CB peak. Then, at $\phi = 180°$, the conductance has two subgap peaks, one at low bias and one just below the critical bias. This angular dependence is qualitatively the same as the thickness dependence going from $D_{F2} = 15$ to $D_{F2} = 26$. This is a striking result: in the superconducting spin valve, the angular dependence constitutes a uniformly increasing or decreasing conductance peak going from a parallel to antiparallel configuration with the position of the peak being dependent on D_{F2} only. In the ferromagnetic Josephson structure, the angular dependence does not affect the height of the peaks, but instead the position of the peaks just like with the D_{F2} dependence. This allows for an extremely large valve effect for almost *any* bias value, as seen in Fig. 5.8a where we see a difference in conductance on the order of the quantum of conductance between 0 and 180° at low biases, and 0 and 90° near the CB. For more realistic interfacial scattering such as in Fig. 5.8b, we see the same qualitative features in the angular dependence. However, unlike in the superconducting spin valve case, the introduction of these barriers does not enhance the valve effect. The peaks decrease in value with increased barrier. This does not apply to $H_{B,0}$ at the X/S_1 contact as this barrier is required for the resonance effects of the odd harmonics.

In Fig. 5.9 we show the angular dependence for $D_{F2} = 26$. The conductance for

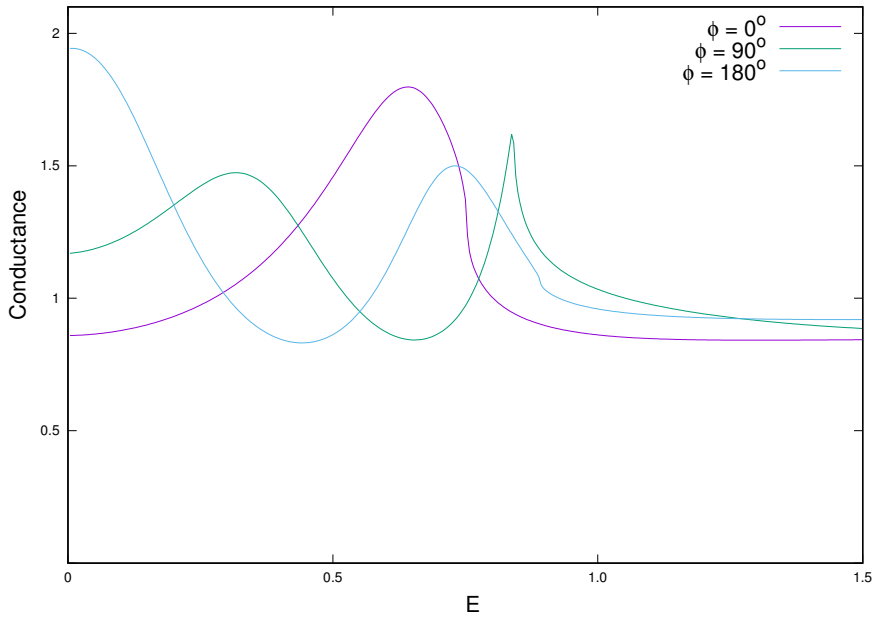

(a) Single barrier at the X/S_1 contact with $H_{B,0} = 0.5$.

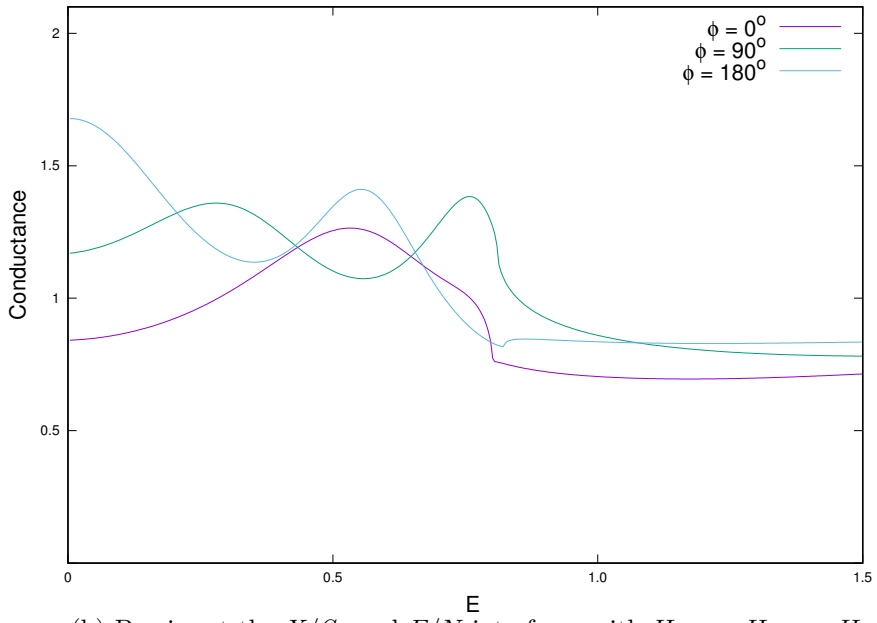

(b) Barrier at the X/S_1 and F/N interfaces with $H_{B,0} = H_{B,2} = H_{B,3} = 0.5$.

Figure 5.8: Self consistent, numerical results for the Conductance (G) vs. Bias (E) in the $S_1/F_1/N/F_2/S_2$ structure for $D_{F2} = 15$ and varying ϕ. The angular dependence closely resembles the D_{F2} dependence for one-quarter of a period.

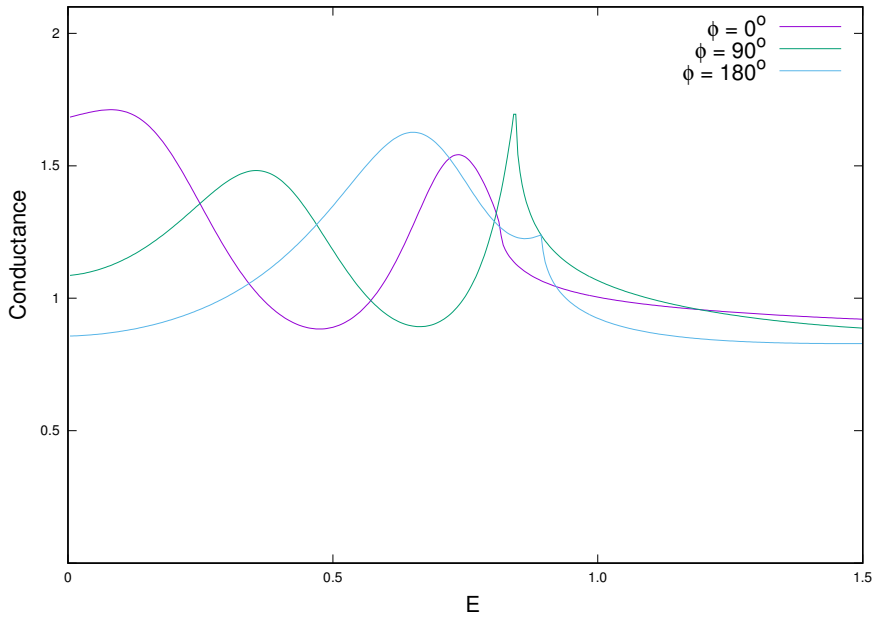

(a) Single barrier at the X/S_1 contact with $H_{B,0} = 0.5$.

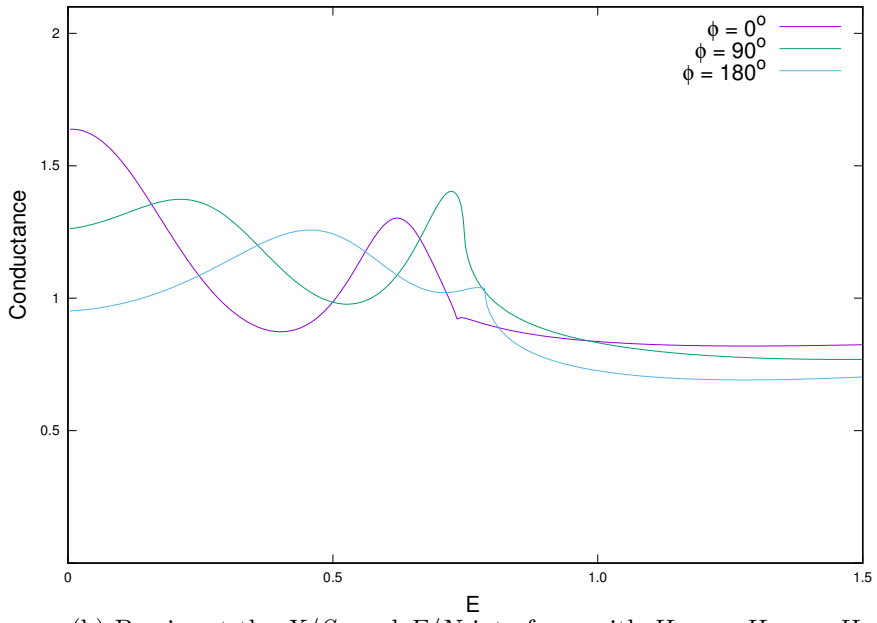

(b) Barrier at the X/S_1 and F/N interfaces with $H_{B,0} = H_{B,2} = H_{B,3} = 0.5$.

Figure 5.9: Self consistent, numerical results for the Conductance (G) vs. Bias (E) in the $S_1/F_1/N/F_2/S_2$ structure for $D_{F2} = 26$ and varying ϕ. The angular dependence closely resembles the D_{F2} dependence for one-quarter of a period.

$\phi = 0$ is the same as in Fig. 5.7 where at $D_{F2} = 26$ we see two peaks: one at low bias and one within the subgap region. For $\phi = 90°$ we see the two peaks shift to the right, with the right peak moving into the critical bias. Finally at $\phi = 180°$ the conductance has merged into a single peak just below the critical bias. This is the same behavior as seen in Fig. 5.5. Indeed, the angle ϕ advances the phase of the overall oscillatory spin-split behavior by $\pi/2$. Comparing Figs. 5.9a and 5.9b, we see again that the presence of the F/N barriers does not enhance the valve effect and slightly decreases the peak conductance. In the $F/N/F/S$ case, only for certain ranges of thicknesses would the valve effect be noticeable (when the peak was in the middle of the subgap region). We see now that in the $S/F/N/F/S$ structure, the peaks change in position with ϕ. This means the valve effect is apparent for any thickness, as any minimum found at $\phi = 0$ will become a maximum when the magnetization is rotated by a certain angle ϕ.

In Sec. 5.4 we summarize our results and how they may apply to real devices and experiments.

5.4 Conclusion

In this chapter we have analyzed the $S_1/F_1/N/F_2/S_2$ ferromagnetic Josephson structure using our numerical approach. Our analysis is in the ballistic limit which includes interfacial scattering characterized by delta-function barrier parameters. In our analysis we have included a normal metal contact X, with interfacial imperfections, which simplifies the calculation of the conductance using the BTK method. In the calculation of the pair amplitude we use a self consistent method that allows both superconductors to have an independent phase. We found that the total phase difference in equilibrium is either 0 or π. In this study, we have focused only on the quasiparticle conductance.

In order to better understand the numerical results, we have used an analytic approximation for both the $N'/N/S$ and $S/N/S$ systems. In this approximation, we assumed a one-dimensional multilayer with a constant pair potential Δ_0. We also assume an imperfect normal metal contact (with interfacial scattering) for the $S/N/S$ system as well as interfacial scattering at the N'/N interface for the $N'/N/S$ system. We found that for large thicknesses D_N the conductance forms a new peak at the critical bias which we call the resonance peaks. In the $N'/N/S$ case the peaks form at equally

spaced intervals λ_n which we call the resonance thicknesses, with harmonic number n. For higher ordered harmonics ($n \geq 1$) there exists multiple peaks which are also evenly spaced between the zero bias and critical bias conductance. We determined in Sec. 5.2.3 that these resonances were due to the interference of Andreev reflected particles at the N/S interface with those reflected at the N'/N interface with non-zero scattering barriers. We also noted that at higher harmonics ($n \geq 1$) the conductance is oscillatory just above the critical bias and slowly decays at the same rate for all harmonics. The frequencies of these oscillations are approximately proportional to the harmonic number n. In the $S/N/S$ case we found two resonance behaviors: "even" and "odd". The even harmonic resonances are the same as those in the $N'/N/S$ case for even values of n, but the odd harmonics have an additional term that depends on the ratio of D_{S1}/Ξ_0 (see Eq. 5.8). This term reduces the resonant thickness of the odd conductance peaks. The oscillatory conductance above the gap is also shifted by this S_1 thickness dependence in the odd harmonic thicknesses.

We then applied our analytic approximation to the ferromagnetic $N/F/S$ and $S/F/S$ systems. In Chapter 3 we studied the spin-split conductance of the $N/F/S$ system, where the conductance peak oscillates between the critical bias and near zero bias for varying thicknesses of the F layer over a wavelength of π/h. We did so for only small thicknesses of D_F, just above the $n = 0$ harmonic. In this chapter, we used our model to study the same effects on the $n = 1$ harmonic where there are two conductance peaks. We saw that both peaks oscillate in position together between the subgap region and the zero bias conductance for the left peak, and the critical bias and subgap region for the right peak. Between those two thickness values, each peak splits, resulting in multiple subgap peaks in the conductance. This also applies to the $S/F/S$ case. In our analysis of the Josephson structure, we saw that for even relatively small values of the F layer thickness (less than the coherence length of the superconductor), the conductance displays multiple subgap peaks. This is because the spin-split oscillations can pull the higher order harmonic peaks into the subgap region since the first harmonic ($n = 1$) is reduced by the presence of the S_1 layer.

Armed with a qualitative understanding of the F layer thickness dependence of our $S/F/S$ analytic calculation, we were then ready to tackle the fully self-consistent

$S_1/F_1/N/F_2/S_2$ ferromagnetic Josephson structure. We studied the F_2 thickness dependence in the parallel configuration of the F layer magnetizations ($\phi = 0$) for the case of clean F/N interfaces and imperfect F/N interfaces. In all cases we assume a nonzero scattering barrier due to a normal metal contact X, which we found to enhance the conductance peaks by decreasing the average subgap conductance. In our numerical calculations we found the same qualitative features of the subgap conductance as found in the analytic $S/F/S$ system. By closely observing one quarter of the total spin-split oscillation with D_{F2} we could see how a single subgap peak at $D_{F2} = 15$ becomes two subgap peaks at $D_{F2} = 26$, with one peak being near the critical bias and one being at low bias. This is in contrast to the $F_1/N/F_2/S$ superconducting spin valve where, for similar thicknesses of the $F_1/N/F_2$ layers, we only saw a single subgap conductance peak.

Finally we conclude the chapter with a study on the the angular dependence of the ferromagnetic Josephson structure. We calculated the conductance for multiple angles ϕ of the relative orientation of the ferromagnetic layer magnetizations (see Fig. 5.1) in the $S_1/F_1/N/F_2/S$ configuration. We saw that the angular dependence was similar to the D_{F2} dependence. By rotating ϕ between the parallel and antiparallel configuration, we advance the phase of the spin-split conductance oscillations by $\pi/2$. This is in stark contrast to the $F_1/N/F_2/S$ case, where the angular dependence was found only in the subgap peak height and *not* in the position of the peaks within the subgap. This allows for a very large valve effect, on the order of the quantum of conductance per channel, which may prove useful in future spintronic devices.

Although we have learned about many new exciting features unique to the ferromagnetic Josephson structures, there are still many unanswered questions. For instance, we were unable to analytically determine the odd resonance thicknesses and had to settle for a phenomenological approximation instead. In addition, it has not yet been determined how the $S_1/F_1/N/F_2/S_2$ angular dependence is related to the spin-split conductance oscillations. There are also many more questions that could be asked, such as the barrier dependence of the S/F interfaces, the S and N layer thickness dependencies, and even the study of the $\Delta_1 \neq \Delta_2$ Josephson structure. We also assumed one imperfect contact, and have yet to study the effect of two imperfect contacts. We believe that this chapter, however, leaves a good foundation and highlights some of the more unique aspects

worthy of future study. We hope that this work will be useful for future experiments into ferromagnetic Josephson structures and their application in spintronic devices.

Chapter 6

Conclusion and Discussion

In this thesis I presented my study on charge and spin transport in ferromagnet, superconductor (F/S) heterostructures. This includes both the $F/N/F/S$ superconducting spin valve and the $S/F/N/F/S$ ferromagnetic Josephson structure, where N is a normal metal spacer. Part of the interest in these structures is their possible application to spintronic devices, with the $F/N/F$ structure (spin valve) acting as a magnetic memory element. The $F/N/F/S$ and $S/F/N/F/S$ devices are unique due to the F/S proximity effect. We discuss the basic theory of superconductivity and the proximity effect in Chapter 1. To summarize, the formation of singlet pairs (Cooper pairs) gives rise to a gap in energy near the Fermi surface. In the N/S proximity effect, the singlet pair amplitude of the s-wave superconductor leaks into the normal metal, reducing the pair potential of the superconductor near the interface. In the F/S proximity effect, the singlet pair amplitude is heavily damped and oscillatory due the exchange field of the ferromagnet. By adding another ferromagnetic layer, with noncollinear magnetization, the singlet pairs may induce long ranged triplet pair correlations. The proximity effects are also directly involved with the transport via Andreev reflections, in which an incoming electron reflects as a hole at the N/S and F/S interfaces. These proximity effects lead to the unique transport properties within these devices which are non-monotonic with the magnetization misalignment angle ϕ between the F_1 and F_2 layers.

Our work is part of a theory/experiment collaboration with the University of California, Irvine. For this reason, we characterize the transport properties and their dependence on the physical parameters such as the layer thicknesses and interfacial

quality. We do so assuming realistic material parameters based on cobalt and niobium, which have been fitted to thermodynamic results in similar systems [9]. We use a self-consistent, numerical method to study the transport in these systems. The self-consistent condition is essential to characterize the full proximity effect and is required for charge conservation.

In Chapter 2 we study the charge and spin transport in $F_1/N/F_2/S$ superconducting spin valve devices. The work presented in this chapter is an edited version of a previous publication Ref. [67]. In this chapter, we present the self-consistent method used in the chapters that follow. We studied charge transport for realistic material and geometrical parameters for use in nanoscale devices using cobalt and niobium. We determined the dependence of the conductance on the layer thicknesses and interfacial quality in addition to the dependence of the magnetization misalignment angle ϕ between the F_1 and F_2 layers. Due to the oscillatory nature of the proximity effect in F/S heterostructures, we found that our results were non-monotonic with many of the parameters studied. We found that the greatest layer thickness dependencies comes from the intermediate N and F_2 layers (the F_2 layer in particular). In addition, we studied the effects due to interfacial barriers and saw that for certain thicknesses of the intermediate F_2 layer, a resonance feature occurs where, at zero bias, there is a peak in conductance that is not affected by the barrier strength. For other values of the thickness, the zero bias conductance decreases monotonically with the barrier strength. We also determined a viable "valve effect" of the angular dependence in the critical bias feature. The critical bias (CB) is the bias at which the conductance transitions to a normal conductance. The angular dependence in the critical bias is non-monotonic and the separation decreases for increasing barrier strengths, but it is still prevalent for realistic scattering parameter values. In this chapter we also studied, in a more limited way, the spin current and spin transfer torque (STT) in a clean $F/F/S$ system. We found that the spin current does not penetrate the superconductor for biases below the critical bias. We also determined that the STT, calculated independently from the spin current, was consistent with the conservation laws (Eq. 2.19). This study forms the foundation for the chapters that follow.

Motivated by the resonance effects found in the charge transport, which were dependent on the F_2 layer thickness, we extended our study on the conductance in superconducting spin valves in Chapter 3 . The work presented in this chapter is an edited version of a previous publication Ref. [68]. We begin this study using an approximate, analytic $N/F/S$ model which was not self-consistent in order to gain a qualitative understanding of the observed phenomenon before moving on to the fully self-consistent $F/N/F/S$ system. We found a subgap (below the critical bias) peak structure in the conductance that was oscillatory with thickness. The subgap peak position oscillates between zero bias and the critical bias. We determined that the oscillations have the same periodicity as the Cooper pair amplitudes of the F/S proximity effect. The peaks form due to a difference in the conductance contributions from incoming spin-up and spin-down electrons, which we call the spin split conductance. These peaks were found to be resilient to the interfacial scattering strength, while the conductance at other biases would decrease with increasing barrier strength. This leads to sharper peaks in the conductance features. In addition, we studied the angular dependence of the magnetization misalignment (the valve effect) and found that the subgap conductance peak value was monotonic with angle ϕ. This angular dependence was also resilient to increased barrier strengths. We believe the work presented in this chapter will be useful in the development of experimental samples and that the valve effect presented may be exploitable in future spintronic devices.

In Chapter 4 we follow up on the spin current and spin transfer torque study presented in Chapter 2. The work presented in Chapter 4 is an edited version of a previous publication Ref. [69]. Previously, we had only studied the idealized $F/F/S$ system. In Chapter 4 we study the realistic $F/N/F/S$ system. Using experimentally relevant parameters such as the layer thicknesses and interfacial scattering barriers, we calculated both the spin current and spin accumulation in superconducting spin valves. The dependencies of these quantities on the parameters, including the misalignment angle ϕ are complex, non-monotonic, and extremely rich in features. Many of these features are not yet fully understood, and only the most prominent ones have been discussed in this work to a sufficient extent. In the greater context, we can make a few general conclusions: We see no penetration of the spin current below the critical bias. We find a critical bias feature in the quasilinear growth of the spin current and spin torque

both above and below the CB. The value of the CB varies with ϕ, as it does for charge current. The prominence of the features observed varies with interfacial scattering and with the intermediate ferromagnetic F_2 layer thickness. The spin accumulation is highly dependent on the physical parameters. The CB features of the local magnetization are different from those of the spin and charge current, and have a greater dependence on the interfacial barrier strengths. We also see a peculiar behavior in the normal metal region, with regular oscillations and rotations of the spin accumulation vector, which emerges as a feature only with non-zero interfacial scattering. The description of the spin accumulation, such as the wavelength of oscillation and its orientation, is dependent on the thickness of the F_2 and N layers. The results presented justify further study, both theoretical and experimental, into the spin transport of $F/N/F/S$ superconducting spin valves. We hope our work lays a proper foundation in understanding the complex spin transport phenomenon.

Finally, in Chapter 5, we study charge transport in the ferromagnetic Josephson structure ($S_1/F_1/N/F_2/S_2$). In this chapter, we focus our attention to the quasiparticle current in the subgap bias region for experimentally relevant parameters. The quasiparticle current is the electron/hole current that flows in addition to the DC and AC Josephson current. We assume that the DC Josephson effect is minimized and the AC oscillations are averaged out as we calculate the forward conductance in these samples. We have also assumed a normal metal contact X with interfacial scattering at the X/S_1 interface. In order to aid our analysis, we study the simpler $N/F/S$ and $S/F/S$ systems using an approximate, non-self consistent method similar to that used in Chapter 3. From this we were able to describe "harmonic resonance" effects which are due to multiple Andreev reflections (MAR). These resonance effects describe the formation of new peaks at the critical bias which shifts lower order harmonic peaks into the subgap. In the Josephson structure, the harmonic peak structure is split between "even" and "odd" peaks which are evenly spaced between even/odd pairs. We then study these resonance features for the numerical and self-consistent $S_1/F_1/N/F_2/S_2$ structure. We found that in the ferromagnetic Josephson structure, these peaks are oscillatory with rich behavior over a thickness periodicity of $2\pi/h$ in F_2, where h is the normalized exchange field. For experimentally relevant thicknesses, the conductance has multiple subgap peaks with oscillations that go between low biases and the critical bias. We also

studied the angular dependence of ϕ, i.e. the valve effect, in our numerical calculation. We found that the conductance structure is oscillatory in the same manner as in the D_{F2} dependence, advancing the phase by $\pi/2$ between the parallel and antiparallel configuration. This is in stark contrast to the valve effect studied in Chapter 3, in which the valve effect was in the height of the conductance peaks and the bias position was dependent on D_{F2} only. In the future, we plan to publish a paper based on these results.

Our primary result in each of these chapters is the self-consistent calculation of the charge and spin transport. Due to the oscillatory and non-monotonic nature of these transport features, in addition to the numerical calculation of the self-consistency condition, it is not possible to extrapolate the results to cover all possible configurations of our physical parameters. Each set of parameters requires its own calculation. The total number of configurations is exceedingly large, and the results presented are only a subset of what we have calculated. In order to aid our investigation, I have created a database for our numerical calculations and a Mathematica program which allows for the easy comparison of the conductance vs bias plots and their dependence on any of the physical parameters. We hope that in the future, the results we have presented and the tools developed will aid future studies in ferromagnetic/superconductor devices, both theoretical and experimental. We have already seen just how rich the transport properties can be and yet we have only scratched the surface. Someday, I expect these devices to become an everyday part of our technology and I am glad to have a part in making it happen.

References

[1] E. Tsymbal and I. Žutić, *Handbook on spin transport and magnetism*, (CRC Press, Boca Raton, Florida 2012).

[2] G. Binasch, P. Grnberg, F. Saurenbach, and W. Zinn, Phys. Rev. B 39, 4828(R) (1989).

[3] A. Fert, Rev. Mod. Phys. 80, 1517 (2008).

[4] M. Eschrig, Rep. Prog. Phys. **78**, 104501 (2015).

[5] I. Žutić, J. Fabian, and S. Das Sarma, Rev. Mod. Phys. **76**, 323 (2004).

[6] Ya. V. Fominov, A. A. Golubov, T. Yu. Karminskaya, M. Yu. Kupryanov, R. G. Deminov, and L. R. Tagirov, JETP Lett. **91**, 308 (2010).

[7] B. D. Josephson, Physics Letters 1 251 (1962).

[8] D. S. Holmes, A. L. Ripple, M. A. Manheimer, IEEE Trans. Appl. Supercond. 23, 1701610 (2013).

[9] A. A. Jara, C. Safranski, I. N. Krivorotov, C.-T. Wu. A. N. Malmi-Kakkada, O. T. Valls, and K. Halterman, Phys. Rev. B **89**, 184502 (2014).

[10] C. Kittel, *Introduction to Solid State Physics – 7th ed.*, (John Wiley and Sons, Inc., New York, NY, 1996).

[11] W. Meissner and R. Ochsenfeld, Naturwiss. **21**, 787-788 (1933).

[12] F. and H. London, Proc. Roy. Soc. (London) **A149**, 71 (1935).

[13] V. L. Ginzburg and L. D. Landau, Zh. Eksperim. i Teor. Fiz. **20**, 1064 (1950).

[14] M. Tinkham, *Introduction to Superconductivity*, (McGraw-Hill, New York, NY, 1975).

[15] P. G. de Gennes, *Superconductivity of Metals and Alloys*, (Addison-Wesley, Reading, MA, 1989).

[16] J. Bardeen, L. N. Cooper, and J. R. Schrieffer, Phys. Rev. **108**, 1175 (1957).

[17] L. N. Cooper, Phys. Rev. **104** 1189 (1956).

[18] N. N. Bogoliubov, Nuovo Cimento **7**, 794 (1958).

[19] J. G. Valatin, Nuovo Cimento **7**, 843 (1958).

[20] G. Deutscher and P. G. de Gennes, Proximity Effects in Superconductivity, edited by R. D. Parks (Dekker, New York), pp. 1005-1034 (1969).

[21] H. Meissner, Phys. Rev. **117**, 672 (1960).

[22] A. I. Buzdin, Rev. Mod. Phys. **77**, 935 (2005).

[23] F. S. Bergeret, A. F Volkov, and K. B. Efetov, Rev. Mod. Phys. **77**, 1321 (2005).

[24] Images courtesy of Chen-Te Wu.

[25] E. A. Demler, G. B. Arnold, and M. R. Beasley, Phys. Rev. B **55**, 15174 (1997).

[26] Buzdin, A. I., and M. Y. Kuprianov, Pis'ma Zh. Eksp. Teor. Phys. **52**, 1089-1091 [JETP Lett. **52**, 487-491 (1990)].

[27] K. Halterman and O. T. Valls, Phys. Rev. B **66**, 224516 (2002).

[28] K. Halterman and O. T. Valls, Phys. Rev. B **65**, 014509 (2001).

[29] F. S. Bergeret, A. F Volkov, and K. B. Efetov, Phys. Rev. Lett. **86**, 3140 (2001); Phys. Rev. B **68**, 064513 (2003); Rev. Mod. Phys. **77**, 1321-1373 (2005).

[30] K. Halterman and O. T. Valls, Phys. Rev. B **80**, 104502 (2009).

[31] P. H. Barsic, O. T. Valls and K. Halterman, Phys. Rev. B **75**, 104502 (2007).

[32] V. I. Zdravkov, J. Kehrle, G. Obermeier, D. Lenk, H.-A. Krug von Nidda, C. Müller, M. Yu. Kupriyanov, A. S. Sidorenko, S. Horn, R. Tidecks, and L. R. Tagirov Phys. Rev. B **87**, 144507 (2013).

[33] V. L. Berezinskii, JETP Lett. **20**, 287 (1975).

[34] M. Eschrig and T. Löfwander, Nature Physics **4**, 138 (2008).

[35] P. V. Leksin, N. N. Garif'yanov, I. A. Garifullin, Ya. V. Fominov, J. Schumann, Y. Krupskaya, V. Kataev, O. G. Schmidt, and B. Büchner, Phys. Rev. Lett. **109**, 057005 (2012).

[36] F. S. Bergeret, A. F. Volkov, and K. B. Efetov, Appl. Phys. A **89**, 599 (2007).

[37] Y. Kalcheim, O. Millo, A. DiBernardo, A. Pal and J.W. Robinson, Phys. Rev. B **92**, 060501 (2015).

[38] A. Singh, S. Voltan, K. Lahabi, and J. Aarts, Phys. Rev. X **5**, 021019 (2015).

[39] K. Halterman and M. Alidoust, Phys. Rev. B **94**, 064503 (2016).

[40] J. Zhu, I. N. Krivorotov, K. Halterman and O.T. Valls, Phys. Rev. Lett. **105**, 207002 (2010).

[41] C.-T. Wu, O. T. Valls and K. Halterman, Phys. Rev. B **90**, 054523, (2014).

[42] T. Yu. Karminskaya, A. A. Golubov, and M. Yu. Kupryanov, Phys. Rev. B **84**, 064531 (2011).

[43] E. C. Gingrich, B. M. Niedzielski, J. A. Glick, Y. Wang, D. L. Miller, R. Loloee, W. P. Pratt Jr, N. O. Birge, Nature Physics **12**, 564-567 (2016).

[44] I. P. Nevirkovets, O. Chernyashevskyy, G. V. Prokopenko, O. A. Mukhanov, and J. B. Ketterson, Superconducting-ferromagnetic transistor. IEEE Trans. Appl. Supercond. **24**, 1800506 (2014).

[45] F. Chiodi *et al.*, EPL **101**, 37002 (2012).

[46] C.-T. Wu, O. T. Valls, and K. Halterman, Phys. Rev. Lett. **108**, 117005 (2012).

[47] C.-T. Wu, O. T. Valls, and K. Halterman, Phys. Rev. B **86**, 184517 (2012).

[48] C.-T. Wu, O. T. Valls, and K. Halterman, Phys. Rev. B **86**, 014523 (2012).

[49] A. F. Andreev, Sov. Phys. JETP **19**, 1228 (1964).

[50] G. E. Blonder, M. Tinkham, and T. M. Klapwijk, Phys. Rev. B **25**, 4515 (1982).

[51] S. Kashiwaya, Y. Tanaka, M. Koyanagi, and K. Kajimura, Phys. Rev. B **53**, 2667 (1996).

[52] J. Linder, T. Yokoyama, and A. Sudbø, Phys. Rev. B **79**, 224504 (2009).

[53] C. Visani, Z. Sefrioui, J. Tornos, C. Leon, J. Briatico, M. Bibes, A. Barthélémy, J. Santamaría, and Javier E. Villegas, Nature Phys. **8**, 539 (2012).

[54] Z. P. Niu, Europhys. Lett. **100** 17012 (2012).

[55] Y.-Q. Ji, Z.-P. Niu, C.-D. Feng, and D.-Y. Xing, Chinese Phys. Lett. **25**, 691 (2008).

[56] M. J. M. de Jong and C. W. J. Beenakker, Phys. Rev. Lett. **74**, 1657 (1995).

[57] I. Žutić and O. T. Valls, Phys. Rev. B **61**, 1555 (2000).

[58] T. P. Orlando and K. A. Delin, *Foundations of Applied Superconductivity* pp. 393-488 (Addison-Wesley Publishing Company, Reading, MA, 1991).

[59] P. W. Forder, J. Phys. D: Appl. Phys. 10 1413 (1997).

[60] S. Pottorf. *Subgap qusiparticle transport and low frequency critical current fluctations in $Nb/AlO_x/Nb$ Josephson junctions*, pp. 27 Chapter 3. PhD dissertation, Stony Brook University, Dept. of Physics and Astronomy (2007).

[61] J. Hajer, M. Kessel, C. Brüne, M. P. Stehno, H. Buhmann, and L. W. Molenkamp, arXiv: 1905.09593 (2019).

[62] P. F. Bagwell, Phys. Rev. B **49**, 6841 (1993).

[63] F. Sols and J. Ferrer, Phys. Rev. B **49**, 15913 (1994).

[64] J. Sanchez-Canizares and F. Sols, Phys. Rev. B **55**, 531 (1997).

[65] P. H. Barsic and O. T. Valls Phys. Rev. B **79**, 014502 (2009).

[66] K. Halterman, O. T. Valls and P. H. Barsic, Phys. Rev. B **77**, 174511 (2008).

[67] E. Moen, O. T. Valls, Phys. Rev. B **95**, 054503 (2017).

[68] E. Moen, O. T. Valls, Phys. Rev. B **98** 104512 (2018).

[69] E. Moen, O. T. Valls, Phys. Rev. B **97**, 174506 (2018).

[70] S. Bhatti, R. Sbiaa, A. Hirohata, H. Ohno, S. Fukami, S. N. Piramanayagam, *Spintronics based random access memory: a review*, Materials Today, ISSN 1369-7021 (2017).

[71] Y. Gu, G. B. Halász, J. W. A. Robinson, and M. G. Blamire, Phys. Rev. Lett. **115** 067201 (2015).

[72] Q. Cheng and B. Jin, Physica C: Superconductivity **473**, 29 (2012).

[73] G. Baym and L. P. Kadanoff, Phys. Rev. **124**, 287 (1961).

[74] A. Spuntarelli, P. Pieri, G. C.Strinati, Phys. Rep. 488, 111 (2010).

[75] N. W. Ashcroft and N. D. Mermin, *Solid State Physics*, (Philadelphia, PA 1976). See Appendix C.

[76] D. C. Ralph and M. D. Stiles, J. Magn, Magn. Mater. **320**, 1190 (2008).

[77] V. V. Ryazanov, V. A. Oboznov, A. Yu. Rusanov, A. V. Veretennikov, A. A. Golubov, and J. Aarts Phys. Rev. Lett. 86, 2427 (2001).

[78] B. M. Niedzielski, T. J. Bertus, J. A. Glick, R. Loloee, W. P. Pratt, Jr., and N. O. Birge Phys. Rev. B **97**, 024517 (2018).

[79] A. Di Bernardo, S. Diesch, Y. Gu, J. Linder, G. Divitini, C. Ducati, E. Scheer, M. G. Blamire, and J. W. A. Robinson, Nat. Commun. **6**, 8053 (2015).

[80] N. Banerjee, C. B. Smiet, R. G. J. Smits, A. Ozaeta, F. S. Bergeret, M. G. Blamire, and J. W. A. Robinson, Nat. Commun. **5**, 3048 (2014).

[81] K. Halterman, P. Barsic and O.T. Valls, Phys. Rev. Lett. **99** 127002 (2007).

[82] M. Johnson, Phys. Rev. B **58**, 9635 (1998).

[83] M. Johnson, Physica E **10**, 472 (2001).

[84] L. R. Tagirov, Phys. Rev. Lett. **83**, 2058 (1998).

[85] A. F. Volkov, A. V. Zaitsev, T. M. Klapwijk, Physica C **210**, 21 (1993).

[86] A. Ozaeta, A. S. Vasenko, F. W. J. Hekking, and F. S. Bergeret, Phys. Rev. B **86**, 060509(R) (2012).

[87] P. V. Leksin, N. N. Garifyanov, I. A. Garifullin, J. Schumann, V. Kataev, O. G. Schmidt, and B. Büchner, Phys. Rev. B **85**, 024502 (2012).

[88] M. Johnson, Phys. Rev. B **70**, 2142 (1993).

[89] F. J. Jedema, A. T. Filip, and B. J. van Wees, Nature **410** 345 (2001).

[90] J. C. Slonczewski, J. Magn. Magn. Mater. **159** L1 (1996).

[91] E. B. Myers et al., Science **285**, 867 (1999).

[92] L. Berger, Phys. Rev. B **54**, 9353 (1996).

[93] E. B. Myers, D. C. Ralph, J. A. Katine, R. N. Louie, and R. A. Buhrman, Science **285**, 867 (1999).

[94] P. V. Leksin, N. N. Garif'yanov, J. Schumann, H. Vinzelberg, V. Kataev, R. Klingeler, O. G. Schimdt, and B. Büchner, Appl. Phys. Lett. **97**, 102505 (2010).

[95] S. Takahashi and S. Maekawa, Phys. Rev. B **67** 052409 (2003).

[96] K. Halterman and O. T. Valls Phys. Rev. B **69**, 014517 (2004).

[97] K. Halterman, O.T. Valls, and C-T Wu, Phys. Rev. B **92**, 174516 (2015).

[98] A. I. Buzdin, L. N. Bulaevskii, and S. V. Panyukov, Pisma Zh. Eksp. Teor. Fiz. 35, 147 (1982) [JETP Lett.35, 178 (1982)].

[99] A. I. Buzdin and M. Y. Kuprianov, Pisma Zh. Eksp. Teor. Fiz. 53, 308 (1991) [JETP Lett.53, 321 (1991)].

[100] T. P. Orlando and K. A. Delin, *Foundations of Applied Superconductivity* pp. 489-556 (Addison-Wesley Publishing Company, Reading, MA, 1991).

[101] L. J. Barnes, Phys. Rev. 184, 434 (1969).

[102] J. B. Hansen, M. T. Levinsen, P. E. Lindelof, B. Dueholm, J. Mygind, N. F. Pedersen, and O. H. Soerensen, Appl. Phys. Lett. 35, 28 (1979).

[103] T. I. Baturina, D. R. Islamov, and Z. D. Kvon, Jetp Lett. 75 326 (2002).

[104] F. Giubileo, M. Aprili, F. Bobba, S. Piano, A. Scarfato, A. M. Cucolo, Phys. Rev. B **72**, 174518 (2005).

[105] M. Octavio, M. Tinkham, G. E. Blonder, and T. M. Klapwijk, Phys. Rev. B **27**, 6739 (1983).

[106] R. Kmmel, U. Gunsenheimer, and R. Nicolsky, Phys. Rev. B **42**, 3992 (1990).

[107] C. Cuevas, J. Hammer, J. Kopu, J. K. Viljas, and M. Eschrig, Phys. Rev. B **73** 184505 (2006).

[108] P. W. Anderson, J. Phys. Chem. Solids 11, 26 (1959).

[109] A. A. Abrikosov, L. P. Gorkov and I. E. Dzyaloshinski, Methods of Quantum Field Theory in Statistical Physics (Dover, 1963).

[110] K. D. Usadel, Phys. Rev. Lett. **25**, 507 (1970).

[111] A. Furusaki, Superlattices and Microstructures, Vol. 25, 809 (1999).